University of Nottingham
UK | CHINA | MALAYSIA

Surface Formation and Modification in Electrical Discharge Machining

Shamraze Ahmed (BSc)

Faculty of Engineering, Department of Mechanical, Materials, and Manufacturing Engineering

University of Nottingham

November 2022

Abstract

Electrical discharge machining (EDM) is a non-conventional machining process predominately used to machine hard materials that are difficult to machine using conventional processes. Material removal is through a non-contact thermally driven process utilising electrical discharges. One drawback of EDM is the formation of a recast surface which can affect part properties. Oxide layers are sites of potential cracks, are brittle, are prone to spalling, potentially contributing to premature part failure, have lower melting temperatures, are porous and loose, and are difficult to control. These recast layer defects must be controlled via lengthy parameter optimisation or removed post-process, where surface integrity is critical.. The recast layer has been studied extensively; however, oxides have not been studied in depth, only through observations or brief discussions as part of other works.

The thesis first aims to understand EDM recast oxide formation and propose a route to reduce oxides. By altering parameters, the aim is to alter discharge energy and discharge/crater formation characteristics, as well as cooling and flushing of the spark gap. This showed that current, on-time and discharge energy lead to increased oxides, while off-time and pressure decreased oxides, which was linked to differences in gas, molten crater, and gap characteristics, and explored via constant energy experiments. This showed the importance of parameter discharge impulse force, which alters ejection and oxidation behaviour. Therefore, to achieve a feature with low amounts of oxides, a shorter on-time and lower discharge energy is needed, as well as increased flushing and off-time. This results in a parameter with high discharge impulse and high gap flushing and cooling.

Electrochemical methods have been used to remove recast post-process, however limited work has been done in combining EDM and ECM in a single process. A method to produce a zero-recast surface in a single controllable process, in a single step, combining the accuracy of EDM with the surface finish of ECM, has been proposed in this thesis. Electrochemical dissolution was used to remove the recast layer while electrical discharges were used to advance hole depth. The expansion of the side wall enables EDM to occur only on the frontal area, while ECM is limited on the side, thus creating discrete electrolytic and dielectric zones. To control dissolution dielectric electrical conductivity was altered and to control dissolution mechanisms type of salt additive was changed. NaCl produced a pitted surface while $NaHCO_3$ produced a surface with passive oxides with limited recast removal. $NaNO_3$ and $NaNO_2$ produced zero-recast surfaces, however with regions of excessive electrochemical pitting and removal. Finally, Na_2SO_4 and Na_2SO_3 produced smooth surfaces with removed recast, with Na_2SO_3 removing the recast through controlled electro-polishing. The preferred surface and most controllable electrolytic-dielectric was found to be Na_2SO_3.

To understand the balance between the EDM and ECM parts of the process, pulse waveform analysis must be conducted. The process was split into four pulse types and their significance explained: electrical discharge, semi-arc discharge, delayed discharge, and electrochemical. Intervals of high-voltage, when using DI, would result in regions of ECM when conductivity was increased. The EDM:ECM balance was crucial to process understanding and was directly affected by the high voltage intervals which occur due to gap conditions. The electrochemical difference between electrolytic-dielectrics

was shown through the EDM:ECM pulse ratio and gas analysis, showing that NaCl, which is the most aggressive salt, has the most ECM pulses, while $NaHCO_3$ which is the least aggressive has the most EDM pulses. Differences in electrolytic-dielectrics were explained due to dissolution mechanisms and pulse charge, which increase the high voltage intervals and ECM pulses. Similarly, an increase in conductivity and depth increases ECM pulses and charge, hindering EDM pulses. A mathematical model was used to illustrate the overall process balance through fundamental electrochemical theory and process pulse data. Through this model, the point during machining at which complete recast layer removal occurs is predicted and validated through experimental analysis.

Publications

S. Ahmed. A. Speidel, J.W. Murray, N. Ahmed, M. Cuttell. A.T. Clare. Electrolytic-Dielectrics: A route to zero recast Electrical Discharge Machining. International Journal of Machine Tools and Manufacture, Volume 181, 2022.

M. Castro-Palacios, S. Ahmed, N. Ahmed, J.W. Murray, A. Speidel, J. Duffin, J. Kell, A.T. Clare. A dual material removal mechanism for clearing of obstructed holes via electrical discharge machining. Manufacturing Letters 31, 10-14. 2022.

T. Petersen, S. Ahmed, M. Kunieda, A. Klink. Observation of EDM plasma behaviour influenced by parasitic working gap capacitance. Procedia CIRP 95, 189-194. 2020.

Patents

S. Ahmed, A.T. Clare, J. Kell, D. Clark, A. Speidel, M. Castro-Palacios, P. Smith, D. Novovic. A compound and a method of using the compound. US20210107078A1 (& EU). 2021.

S. Ahmed, J. Mitchell-Smith, A. Jackson-Crisp. An apparatus and a method of using the apparatus. GB2580474B. 2021.

S. Ahmed, J. Mitchell-Smith, A. Jackson-Crisp, A.T. Clare. An electro-discharge machining tool and a method of using the same. GB2578306B (& EU, US, CA, SG, CN). 2020.

J. Kell, G. E. Rigg, S. Ahmed, M. Castro-Palacios, A.T. Clare. Debris removal. GB2107236.8. 2021 (Pending)

Acknowledgements

I would like to thank my supervisor Professor Adam Clare for his support, guidance, advice, and patience throughout my PhD. It was due to his support and encouragement that I have developed significantly, both academically and personally. I have had the opportunity to work with a wide variety of people from the university to industrial partners, and to international universities, on exciting and current problems faced in industry. Through working on these unique projects, I have gained invaluable experience that has guided me throughout this PhD and has paved the way for future success.

I would also like to thank my industrial supervisor Martyn Cuttell and Rolls Royce, who has funded and allowed me the opportunity to undertake this PhD with direct links to industry. The work in this thesis would also not be possible without the facilities and guidance from The Nanoscale and Microscale Research Centre, Manufacturing Metrology Team, and The Wolfson Building. I am very grateful to my colleagues Dr James Murray and Dr Alistair Speidel for their support and advice throughout this PhD. I would also like to thank The Japanese Society of the Promotion of Science and Professor Masanori Kunieda, as well as my supervisor, who allowed me the opportunity to conduct research in Japan, which has greatly developed me personally, has widened my horizons, and created cherished memories.

Lastly, but not least, I would like to thank my parents for their support, and to my wife Asma who has given me unending support throughout this long and arduous, but enjoyable, PhD.

Table of Contents

List of Figures

List of Tables

List of Abbreviations

EDM: Electrical discharge machining

ECM: Electrochemical machining

MRR: Material removal rate (for EDM)

SEM: Scanning electron microscope

BSE: Back-scattered electrons

SE: Secondary electrons

EDS: Energy dispersive X-ray spectroscopy

XRD: X-Ray diffraction

Nomenclature

On-time: EDM discharge duration

Off-time: EDM discharge gap between discharges

Current: Peak EDM current

Dielectric pressure: Electrode internal flushing pressure

1 Introduction

Electrical discharge machining (EDM) is a non-conventional machining process predominately used to machine hard materials that are difficult to machine using conventional processes. EDM is a non-contact process which uses thermal energy to remove material via electrical discharges, enabling machining regardless of the material's mechanical properties.

One common application of EDM is in the drilling of turbine blade cooling holes. Due to the extreme heat experienced in engine, the temperature of the blades would normally exceed the melting point of the super-alloy. Additional cooling is therefore critical in the process. Film cooling is therefore utilised, which intakes cool air from the compressor stage and channels it through the blade, exiting through the cooling holes and diffusers and forming the film-cooling layer.

One drawback of EDM is the formation of a rough recast surface layer containing porosity, cracks, contamination, and oxides, which can affect the functional properties of the machined part. Oxide layers are sites of potential cracks, are brittle, have poor mechanical properties, and are prone to spalling, and so may potentially contribute to premature part failure or secondary contamination elsewhere in an engineering system. They are also known to inhibit coating adhesion in certain manufacturing processes.. The recast layer has been studied extensively; however, oxides have not been studied in depth, only through observations or brief discussions as part of other works.

These recast layer defects must be controlled via the lengthy process of parameter and process optimisation. Alternatively, the recast layer is often

removed post-process for applications where surface integrity is critical. This process can add substantial cost and time to the overall machining process.

This thesis firstly aims to understand EDM recast layer oxide formation, which has not been explored extensively in the literature, and aim to propose an approach to reduce oxides. Although the first step aims to reduce oxides in the recast layer and help formation understanding, a recast layer remains. Therefore, the thesis will then propose a single stage process to produce a zero-recast zero-defect EDM surface through a simultaneous electrochemical electric discharge process, with process understanding enhanced through fundamental analysis.

1.1 Aims of Thesis

The aims of this thesis are to investigate formation mechanisms of oxides in the EDM recast layer, which have not been explored extensively in the literature, and then propose an approach to reduce oxides. These EDM recast layer features are an unwanted by-product of the machining process, thus ideally reduced or entirely removed from resulting surfaces. The thesis will then aim to propose a novel process which aims to produce a zero-recast EDM surface with zero defects in a single-stage simultaneous EDM ECM process. To achieve these aims, the thesis will be based on the following aims:

Aim 1: Understanding of oxide formation mechanisms in the EDM process. Although the formation of the recast layer is well understood, a gap in the literature shows that oxide formation in EDM has not been explored extensively in depth, only through observations or brief discussions as part of

other works. This chapter aims to understand the influence of EDM parameters on surface and recast layer oxides. By altering parameters, the aim is to alter discharge energy and discharge/crater formation characteristics, as well as cooling and flushing of the spark gap. This will then enable understanding of the relation to oxide formation. Further fundamental understanding will be formed by linking the gas produced in EDM and parameter discharge energy, as well as high-speed images of single discharge crater behaviour, to formation mechanisms of oxides. This will then enable formation of an approach to reduce oxides in the recast layer by relation to EDM parameters and gap conditions.

Aim 2: Create a zero-recast and zero-defect EDM surface. Although methods to remove the recast layer post-EDM have been produced, a method to produce a zero-recast surface in a single controllable process with understanding of process mechanisms has not. The aim of this chapter is to enable a method to simultaneously remove the EDM recast layer while machining a surface. Electrochemical dissolution was chosen as the means to enable this. The electrochemical and electro discharge removal mechanisms must be controlled in this process to ensure a desired surface. To do this, dielectric conductivity must be altered to control dissolution. To further control dissolution mechanisms, type of salt additive must be changed to induce discrete chemical removal mechanisms.

Aim 3: To provide further fundamental process insight. To understand the balance between the EDM and ECM parts of the process, waveform

analysis must be done to view the balance of electrochemical and electro discharge pulses. Altered process mechanisms can then be understood through differences in waveforms and pulse characteristics. Gas analysis can be used to link to the balance of EDM and ECM by relation to the time varying nature of pulses and relation to the time varying gas production. To illustrate the overall process balance and resulting zero-recast point, a mathematical model must be used by using fundamental electrochemical theory and process pulse data, thereby allowing more generic and transferable data to be utilised in both academic and industrial settings.

1.2 Outline of Thesis

In Chapter 4, the influence of EDM parameters on surface and recast layer oxides was conducted. Current and on-time were altered to control discharge energy and discharge characteristics, and off-time and electrode flushing pressure were altered to control cooling and flushing of the spark gap. Oxides produced by EDM were confirmed via BS-SEM and XRD analysis. Detailed exploration of parameters was then conducted to better understand the relation to oxide formation. The gas produced from EDM as well as the parameter discharge energy were both related to the resulting surface oxide area and formation mechanisms. High-speed video images of single discharges were used to relate fundamental discharge mechanisms to resulting oxide formations. A constant energy experiment was then used to further explore influences of current and on-time on formation mechanisms by excluding discharge energy as a variable.

In Chapter 5, electrolytic-dielectrics that improve machined surface integrity, while maintaining machining rate, are introduced. By adding selected electrolytes to a conventional deionised water dielectric, material removal mechanisms can be altered and controlled in a simultaneous electrical discharge and electrochemical process which both removes material via EDM and removes the recast layer via ECM, producing a zero-recast surface with the accuracy of EDM and the surface finish of ECM. Firstly, NaCl was added at varying conductivities to explore the effect on the machined surface, both with hole depth and conductivity. After this electrochemical dissolution mechanisms were altered by addition of various salts, which result in discrete electrochemical dissolution mechanisms such as passive oxidation, aggressive pitting (non-passivating), and electro-polishing, resulting in varied resultant surfaces. These bespoke dielectrics alter fundamental machining behaviour to alternate between conventional EDM discharging and electrochemical dissolution. Analysis of the recast layer, removal rate, and surface analysis is conducted to relate fundamental understanding to quantifiable machining process output factors used in industry. For the first time, it is shown that machining rate is minimally affected while reducing, and eliminating, the defective EDM recast layer, which would otherwise need removal.

In Chapter 6, the mechanisms behind this unique machining process are described through fundamental waveform, discharge, and gas analysis. Waveform analysis is used to understand process mechanisms and differences between electrolytic-dielectrics, and is used to reveal discrete

pulse types, and their significance to the process. The balance between EDM and ECM, and its time varying nature, is explored through pulse ratio analysis which revealed the importance of the pulse ratio, and the significance of the high voltage intervals to ECM removal. The differences between electrolytic-dielectrics and conductivities are linked to resultant gas rates and changes with hole depth. The role of instability and the importance of gap conditions in process balance is explored and shown to be crucial to the process. Key process parameters are determined, such as EDM: ECM pulse ratio balance, electrolytic-dielectric conductivity, salt type, machining/exposure time, and electrode advance, which are crucial to producing tailored surfaces. A mathematical and validated model will be used to illustrate the overall process balance through fundamental electrochemical theory and process pulse data. Through this model, the point during machining at which complete recast layer removal occurs is predicted and validated through experimental analysis. This adapted EDM process has significant potential to be used for producing recast-free features by using an easily modified dielectric.

2 Literature Review

2.1 Introduction to EDM

Electrical discharge machining (EDM) is a non-conventional manufacturing process used in a wide variety of applications for example high-value moulds, cooling holes in turbine blades, and niche applications such as wear coatings on knives [1-3]. Compared to traditional manufacturing processes, which rely on mechanical forces such as the shearing mechanism, EDM is a non-contact and near zero force process which relies on thermal energy from an electrical discharge to melt and vaporise material for removal, regardless of the material's mechanical properties. Thermal energy is produced by application of a potential difference between the workpiece and tool electrode. After a certain voltage is reached, electrical discharge occurs which causes melting and vaporisation of both the workpiece and tool. A dielectric surrounds the discharge site allowing rapid cooling and material flushing. Some examples of components manufactured by EDM are shown in Figure 1.

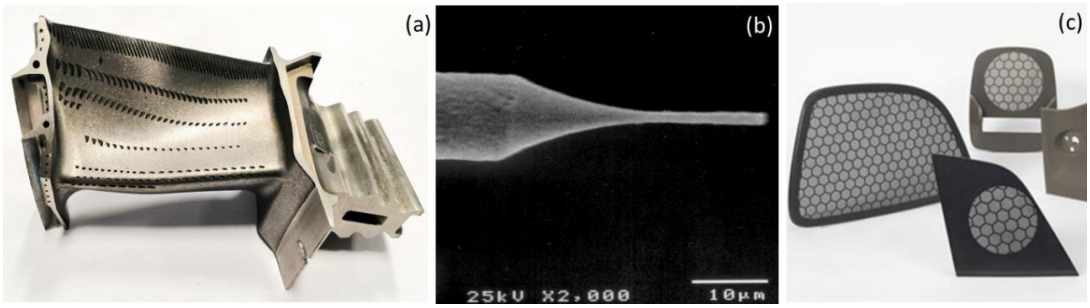

Figure 1. Examples of parts manufactured by EDM: (a) Cooling holes on a turbine blade (hole drilling EDM), (b) micro-rod (micro-EDM) [4], (c) Car speaker grills (Die-sinking EDM) [5].

Electrical discharge drilling is similar to conventional die-sinking EDM with the main distinction being the electrode and flushing mechanisms. In die-sinking EDM electrodes of any shape are lowered towards a workpiece

causing electrical discharges and removal, with the resulting shape being the inverse of the electrode used. Flushing is conventionally provided externally towards the machined surface [6], although internal channels can be machined for complex electrodes. In conventional EDM hole drilling, rotating tubular electrodes with internal flushing channels are used. The combination of high-pressure flushing and rotation of electrodes enables holes to be drilled both faster and deeper with increased debris evaluation, even wear, and faster removal rates, which are crucial for long and deep features machined economically [7, 8].

2.2 Generation of the Spark and Plasma Channel

EDM removes material via electrical discharges by applying a voltage between two conductive materials, in a fluid medium which acts as a dielectric. The dielectric is used to increase the voltage at which breakdown occurs in order to increase the dielectric discharge strength, compared to air. This increase in discharge strength ensures only very high electric fields cause breakdown increasing the discharge energy. The ideal dielectric strength of air is 3×10^6 V/m, kerosene 20×10^6 V/m, and deionised water 65×10^6 V/m, which is when there are no defects on the surface of electrodes, the dielectric is pure, and the electric field is uniform. The breakdown limit is the voltage at which the insulative capacity of the gap has been reached, and is the true measure of discharge likelihood, due to the generated electric field, and electrical breakdown of the dielectric occurs. The breakdown strength of the gap depends on the dielectric strength of the liquid medium (kV/mm), as well as gap conditions such as gap distance, debris, gases, temperature,

ionisation, local electric field strength, electrode/workpiece geometry, and electrode surface characteristics [9-11], and is crucial to control the resulting surface and part dimensions.

At the initiation stage of breakdown, an electron avalanche begins to form. Electron avalanches are formed when a large enough electric field causes acceleration of initial electrons towards the workpiece with sufficient energies to allow the impact ionisation of atoms, which results in free electrons and ions. Initial electrons are generated from radiation such as cosmic X-rays and ultraviolet and are required for ionisation. The initial electron thus causes a cascaded event of impact ionisation (of the dielectric) towards the cathode, which is referred to as the Townsend Avalanche. Electrons contribute more significantly than positive ions due to their higher kinetic energy due to being accelerated to higher velocities in the electric field, which when is higher than the ionisation energy of the colliding particle, causes impact ionisation. A higher initial voltage, and thus electric field, will result in an increased number of electrons due to the electron avalanche resulting in a shorter discharge delay time. Similarly a shorter discharge gap, increased surface roughness, or decreased breakdown voltage will decrease the discharge delay time [12]. The initial electron avalanche always takes place in a region of lower density such as a vapour bubble or fluid vortex. This is because in liquids the higher density increases scattering rates and lowers the mean-free paths, which reduces the probability for electrons and ions to reach ionisation energies. The lowered density increases the possibility of ionisation and thus electron avalanches. The possible mechanisms for low density regions are internal vaporisation due to Joule heating (due to electron emission by the electric field), molecular

decomposition due to Zener breakdown (a type of low voltage electrical breakdown), and micro and nano-bubbles in the dielectric or electrode surface [13-16].

As the electron avalanche propagates towards the workpiece its associated space charge field, which is due to its polarity, increases until it is comparable to the externally applied electric field due to the applied voltage between the electrodes. Once this limit has been reached the avalanche forms a weakly ionised region and is now referred as a streamer. The region of lower density, or bubble, then increases in size as further electron avalanches occur and the streamer propagates due to further impact ionisation. The high voltage gradient between the ionised streamer and dielectric aids further propagation.

In fluids this transition occurs near the cathode, and the streamer extends towards the anode. This is called a negative streamer. The negative streamer has a negatively charged head due to polarity of the initial electron avalanche. Secondary avalanches are caused by electrons that are released due to photoionisation. The photons responsible for photoionisation are generated from atom excitation in the electric field as well as background sources such as cosmic rays. The electrons from the negatively charged head of the streamer neutralise the positive ions of the secondary avalanches. The electrons from the secondary avalanches then extend the head of the streamer causing streamer propagation [17].

When the streamer reaches the anode, the electrons built up at the head enter the anode, and so a weak ionised channel is formed between the anode and cathode. The supplied current then flows freely through this conductive channel causing rapid heating, decomposition of the dielectric, formation of

gas, and an increase in diameter. This highly ionised channel is referred to as the plasma channel.

The plasma channel heats up the surrounding dielectric as well as the electrode and workpiece, decomposing the dielectric into a gas which surrounds the plasma as a high temperature pressurised bubble [18]. During the on-time the plasma also grows in diameter until it reaches a maximum depending on electrical and gap conditions, due to further ionisation and decomposition of the dielectric [19, 20]. The bubble keeps expanding during the plasma duration, restricted by the fluid pressure surrounding the plasma and gas bubble, and due to the energy balance (discharge energy through the plasma and into the workpiece instead of the dielectric medium), until the voltage is switched off stopping current flow. The growth in bubble diameter has a linear relationship with input energy [18]. The plasma channel then begins to collapse followed by the gas bubble which continues to expand until it causes an implosion which removes molten material and splits the initial gas bubble due to the sudden change in pressure [21]. The dielectric then deionises causing free electrons to recombine and returns to being an insulator.

2.3 Work piece and Electrode Material Removal Mechanisms

The heat from the plasma channel causes melting and vaporisation of the workpiece and decomposition of the dielectric. Material removal is through melting, vaporisation, and spalling (in the case of ceramic type materials) [22]. Due to the high heat flux of the plasma, the heat cannot conduct into the workpiece fast enough, resulting in some vaporisation, which occurs at the

start of a discharge, with accompanying molten metal ejection [23, 24]. The molten pool is superheated due to the high pressure in the bubble, caused by the heat input from the plasma channel which causes a build-up of gases and pressure, which is further restricted due to the external liquid pressure [25]. This then prevents further and continuous vaporisation of the molten pool [24], due to the extremely high pressures in the gap which can reach hundreds of MPa [26, 27]. For example, a temperature of 4250 K is needed for the vaporisation of the molten pool of Ti-6Al-4V in order to overcome the plasma pressure, calculated via a multi-physics simulation of the melt-pool hydrodynamics [28]. This is why vaporisation is not considered a major material removal mechanism in EDM. Internal vaporisation can also result in explosions which help material removal [29], in addition to shockwaves caused by external vaporisation. Vapour pressure gradients, from both the electrode and workpiece, also cause shearing forces on the molten pool causing material removal due to high movement which causes ejection once the movement overcomes the bonding strength [30], which also causes the plasma to randomly move on the crater [31]. The vapour pressure is highest in the centre of a crater, thus pushing molten material out, and even after discharge the molten metal continues to move due to inertia [23, 28]. When the pressure on the molten pool overcomes the atomic bonding strength this can also cause molten metal to be removed from the pool and be ejected, so material ejection can also be throughout a discharge [32, 33]. The collision of the vapour jets aids this process [34, 35]. Vapour pressure depends on melting point of the metal, with a lower melting point causing higher vapour jet forces. Once the voltage has stopped and the current stops flowing, the force on the

molten pool decreases. This can also cause sudden vaporisation and molten metal ejection [36].

The collapse of the bubble and plasma also causes removal of molten material due to the sudden pressure change on the pool surface, however this force contributes less when the gap is filled with gas for longer on-times, insufficient flushing, and longer machining times [37]. The bubble expansion and collapse also provide a pulsating impulse force on the molten pool and surroundings which contributes to the removal mechanism as discussed above [38]. The splitting of the bubble and resulting change in flow fields also increase debris flushing and molten metal ejection [21, 39].

2.4 The Dielectric Medium

Petroleum derived hydrocarbon oils such as kerosene are commonly used in die-sinking EDM as a dielectric. Alternatives are synthetically produced hydrocarbon oils such as isoparafin, which is a compound synthesised from petroleum distillates using a catalyst. Hydrocarbon oils are used due to their insulative properties, low viscosity for improved spark performance and flushing, and due to being non-polar so due not dissolve material readily. Deionised water (DI) is used in W-EDM and hole-drilling EDM and is a non-corrosive and environmentally friendly alternative [40] which also has a lower viscosity than oil based dielectrics. H_2O is a polar molecule made up of hydrogen and oxygen, with hydrogen sharing electrons in a covalent bond with oxygen. Material can dissolve by separating into anions and cations due to its polar nature. The polarity is due to an electronegativity difference of 1.24 between the hydrogen and oxygen, which causes more electrons on the

oxygen side of the molecule causing an asymmetric electron distribution. As material can be dissolved in water, in EDM the water must be filtered and deionised to reduce its conductivity and increase its breakdown strength by filtering through a resin bed. Cations and anions are removed from the water by a sorption process known as ion-exchange [41] in which the resin consisting of hydron and hydroxide exchange for the ions in the water, which then recombine as water. A ceramic filter is also used to filter debris and bacteria, while a paper filter is for larger debris.

Higher viscosity liquids, such as oil based dielectrics, also result in increased material removal efficiency due to increased bubble pressure and ejection [42], restricted plasma channel, and energy density [43], but also exhibit a reduced flushing ability as compared to DI. Increased cooling of water compared to oil also results in reduced surface cracks, but due to the larger heat capacity bubble pressure is decreased leading to decreased molten metal removal due to bubble pressure [43]. The impulse force is also higher with an increase in liquid viscosity due to the increased pressure on the plasma, bubble, and molten pool [44] and was shown to be related to bubble expansion and shrinkage [45].

An increase in electrical conductivity was also shown to increase electrolysis and oxidation due to a leaking current [46].The higher conductivity of water compared to oil also results in a larger gap, overcut, lower breakdown strength, increased recast layer thickness, and is seen to increase with conductivity [47]. A higher thermal conductivity, which increases with conductivity, also increases the plasma channel propagation and decreases energy density [48].

Additives are also often added to dielectrics to alter machining performance. Powder Mixed EDM (PM-EDM) consists of a mixture of dielectric and fine powder and is used to reduce dielectric breakdown strength, due to smaller paths for electron movement and increased local electric fields, and increase the gap for improved stability and production of mirror-like finishes [40, 49] due to secondary discharges which distribute energy [50]. Surfactants, such as non-ionic Span 20 and Span 80 can be added to dielectrics to decrease surface tension and act as a dispersant to decrease particle agglomeration by adsorbing at the liquid air interface, so more attraction to air than water to water. This increases uniformity of debris dispersion and overall flushing and gap conditions, aided by the slight increase in conductivity which increases the gap width, resulting in an increased MRR and decreased recast layer thickness. It also improves machining in PM-EDM [51, 52]. This can be similarly done with oleic acid [53-55]. Dielectrics composed of organic compounds with larger molecular structures (particles) as compared to H_2O, such as ethylene glycol, glycerine, polyethylene glycol 200, polyethylene glycol 400, polyethylene glycol 600, dextrose, and sucrose can be used to improve MRR (and flushing) by increased viscosity, plasma pressure, energy density, and higher gas pressure due to decomposition of heavier compounds [56-58]. Other additives such as aromatic hydrocarbons can be used to decrease gap voltage and delay time, resulting in increased MRR by 50 % [59], explained by effects on the Helmholtz double layer [48]. Breakdown limit can also be increased by additives such as amino acids (Zwitterion, β-Alanine, Glycine) and water soluble polymers (Polyacrylamide, polyvinyl alcohol, polysaccharide) by affecting the electric double layer and discharge

characteristics (localised electric fields leading to ionisation in particle vicinities) and by increasing the molecular size of dielectric particles (longer hydrocarbon chains) or additives [54, 60].

2.5 Gap Conditions

The constant material removal and gas evolution in EDM can cause problems in machining stability and control, therefore the dielectric is used to provide constant flushing of gas and material to restore the dielectric to optimum conditions. With depth, the size of gas bubbles increase [61] and debris evacuation decreases resulting in debris accumulation [62], worsening gap conditions. It can lead to concentrations of debris and molten material at bubble interfaces, which causes consecutive discharges at these locations due to the decreased breakdown limit [63, 64] and can lead to worsening of machining. Longer on-times especially cause the gap to be saturated with gases and large debris. If gap flushing is not good and debris begin to concentrate in one region, it can cause a cascade event which results in excessive sparking in the area of reduced flushing and debris or gas accumulation. Dielectric flushing pressure (and exit velocity) can be used to decrease the measured particle concentration significantly and was shown to increase the MRR, reduce the breakthrough stage, and improve surface finish [7, 65]. The effect of flushing pressure on cooling in hole drilling EDM however has not been explored significantly (outside of the effect on MRR and surface characteristics).

2.6 The EDM Surface

Figure 2 shows a schematic of the EDM recast layer, which contains porosity, cracks, contamination, and oxides [66], which can affect the functional properties of the machined part [67], while Figure *3* shows a BS-SEM image of the surface.

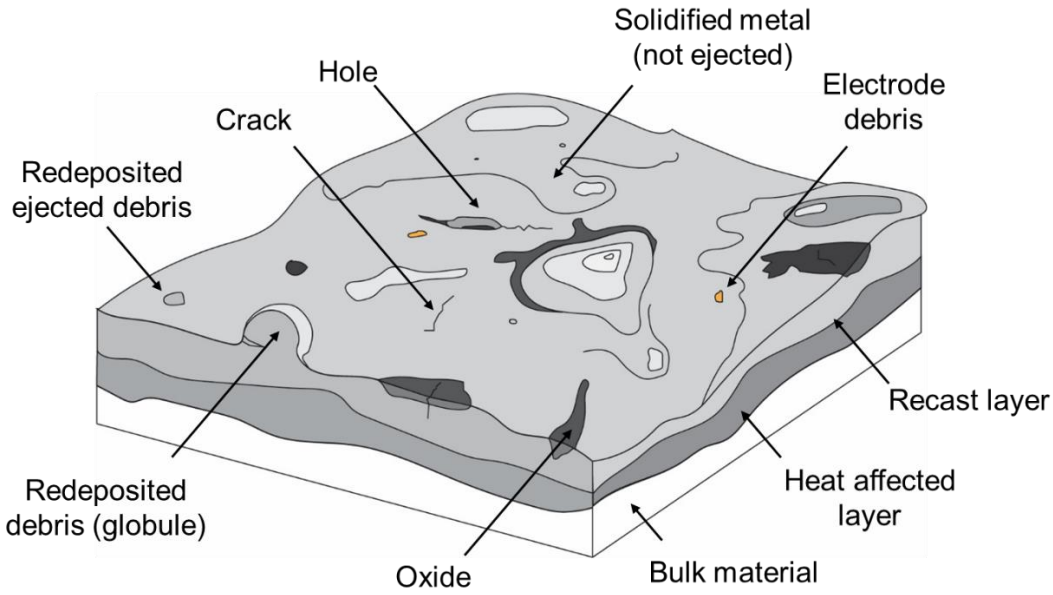

Figure 2. The recast layer with highlighted components. Four layers are shown: The surface layer, recast layer, heat affected layer, and bulk material.

We can see that the recast layer consists of resolidified material, workpiece and electrode debris, cracks, holes, and oxides. Below this is the heat affected layer which has altered properties due to thermal effects. Compared to the base material, the EDM recast layer has increased failure modes and reduced mechanical properties. Redistribution of elements form difference phases and crystal structures, resulting in altered physical properties. Due to the hard and brittle nature of the material due to rapid melting and quenching, crack propagation and growth is increased. Cracks are attributed to thermal and tensile stresses due to the thermal gradients. Rapid cooling causes cracks,

plastic deformation, and residual stress build-up [68-75]. Stress concentration zones are also increased when brittle oxides spall from the base material and due to the increased surface roughness. Below the surface the heat affected zone has been heated but not melted slightly altering the structure, but not the composition, for example the size or orientation of grains. Most of these recast layer components are strictly controlled in industry in surface standards; however, oxides are not well explored in industry or the literature.

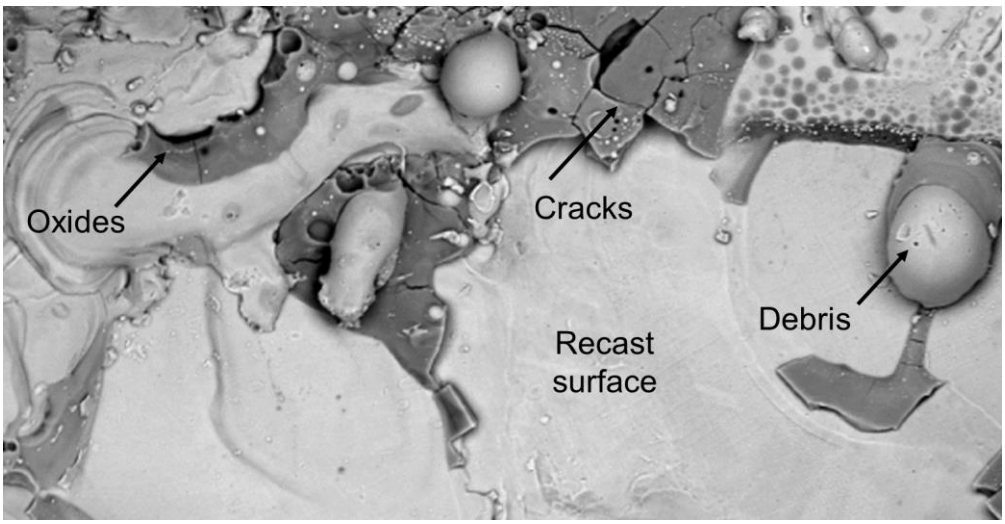

Figure 3. A BS-SEM image of the surface of the recast layer showing surface features: cracks, oxides, debris, and the recast surface.

2.7 Oxidation

Oxides are commonly caused by chemical reactions with oxidising species and metals. An oxidation reaction involves the transfer of electrons between two species, causing the metal to be positively charged while the oxidiser negative, resulting in an ionic bond due to electrostatic attraction. An atom is oxidised if its oxidation number increases, losing electrons. In this case, oxygen is the oxidising agent while the metal is the reducing agent, oxygen thus gains electrons. The general formula for oxidation is Metal + Oxygen →

Metal Oxide ($2M + O_2 = 2MO$). In this case the oxides formed are either single metal oxides (such as TiO_2) or mixed oxides, which are oxides with cations of more than one chemical element (such as $AlTaO_4$).

The likelihood of oxidation can be partly explained by element oxygen affinity, which can be obtained from Ellingham diagrams. These diagrams plot the Gibbs standard free energy in kJ mol^{-1} with temperature and partial pressure, with a lower value denoting higher affinity for oxidation [76-79], an example of which is shown in Figure 4. The slop of each line is the change in entropy, which is positive for oxide generation due to an increase in order, and the intercept of the line is the enthalpy, which is negative as oxidation gives of heat. Lower reactions on the figure are more likely to occur relative to other reactions on the figure and are more stable, as compared to gold oxides which rapidly reduce. The partial pressure below which oxidation is not likely to occur as it is lower than the equilibrium partial pressure can also be found using the diagram.

The use of Ellingham diagrams can be considered a guide to understanding oxide formation and comparisons between element oxidation, and not a tool, due to the formation of oxides in EDM not occurring at equilibrium and also far above the temperature range of oxidation data obtainable.

The Gibbs Standard free energy is the change in Gibbs free energy between the products and reactants of a reaction, which depends on the Gibbs free energy, product/reactant activity, and temperature of the reactant gas. The Gibbs free energy can be described as available energy to do work in the system, and is defined as $G = H – TS$, where G is the Gibbs free energy, H is the enthalpy, T is the temperature, and S is the entropy. If we assume the

change in free energy occurs at constant temperature and pressure, then the change in free energy is zero. This results in $G = G° + RT\ln(p / p°)$ (for gases), where G° is the standard free energy, R is the gas constant, p is the partial pressure, and p° is the standard pressure. (p / p°) is a measure of the reactant activity, which is a measure of the ability of a component to take part in a reaction (the quantity of a component compared to its standard state which in this case is standard atmosphere). The change in Gibbs free energy between products and reactants can then be expressed as $\Delta G = G_C – (G_A + G_B)$, where A is the metal, B is oxygen, and c is the oxide, which results in $\Delta G = \Delta G° + RT\ln(Q)$. Q is the reaction quotient (measure of reaction activity) and is equal to $(a_{mO2} / a_m\, p_{O2})$, where a_{mO2} and a_m are the measure of activity for the metal oxide and metal, and p_{o2} is the activity for oxygen (the partial pressure). Activity of the metals is defined as γX, where X is the metal concentration (mole fraction) and γ is the activity coefficient determined experimentally. If we don't have γ we can assume ideal behaviour at standard state (solid) and take as unity. At the equilibrium point of the reaction the change in free energy is zero, therefore $\Delta G° = -RT\ln K_p$, where K_p is defined as the equilibrium constant which can be simplified as $(1 / p_{O2})$. From the value of ΔG°, the equilibrium partial pressure of O_2 can be found, which is the partial pressure of oxygen where no reaction occurs.

If the partial pressure is higher than the equilibrium partial pressure then the Gibbs standard free energy is negative resulting in a driving force for oxidation, which continues until the partial pressure of oxygen settles back at equilibrium. Therefore, if the Gibbs free energy of the product is smaller than the reactants, the change is negative. While the change remains negative the reaction

continues, changing the proportion of reactants and products, thus the negative change is the driving force of the reaction and only stops once the change is zero. This essentially means that driving force for a particular reaction is higher when the Gibbs Standard free energy is smaller (more negative) showing that it has the highest likelihood of reacting to form oxides. For alloys, the oxidation of a specific element depends on its activity in the alloy (γX), which depends on the concentration in the alloy and likelihood of reaction or element interactions. This changes the free energies and partial pressures of the reactions, changing the reaction likelihood.

Therefore, we can see that oxidation depends on temperature, oxygen partial pressure, and reactant concentration. Also, in this case the reaction is a heterogeneous reaction, which is a reaction involving two or more phases (gas and liquid), therefore the rate also depends on the surface/interface area available for reaction (which alters the activity). Compared to solids, molten metals are said to have 3 to 20 orders of magnitude higher diffusivity which explains the rapid oxidation of the molten metal [78]. Oxygen solubility is high in liquid metals and increases with the above stated variables increasing oxidation.

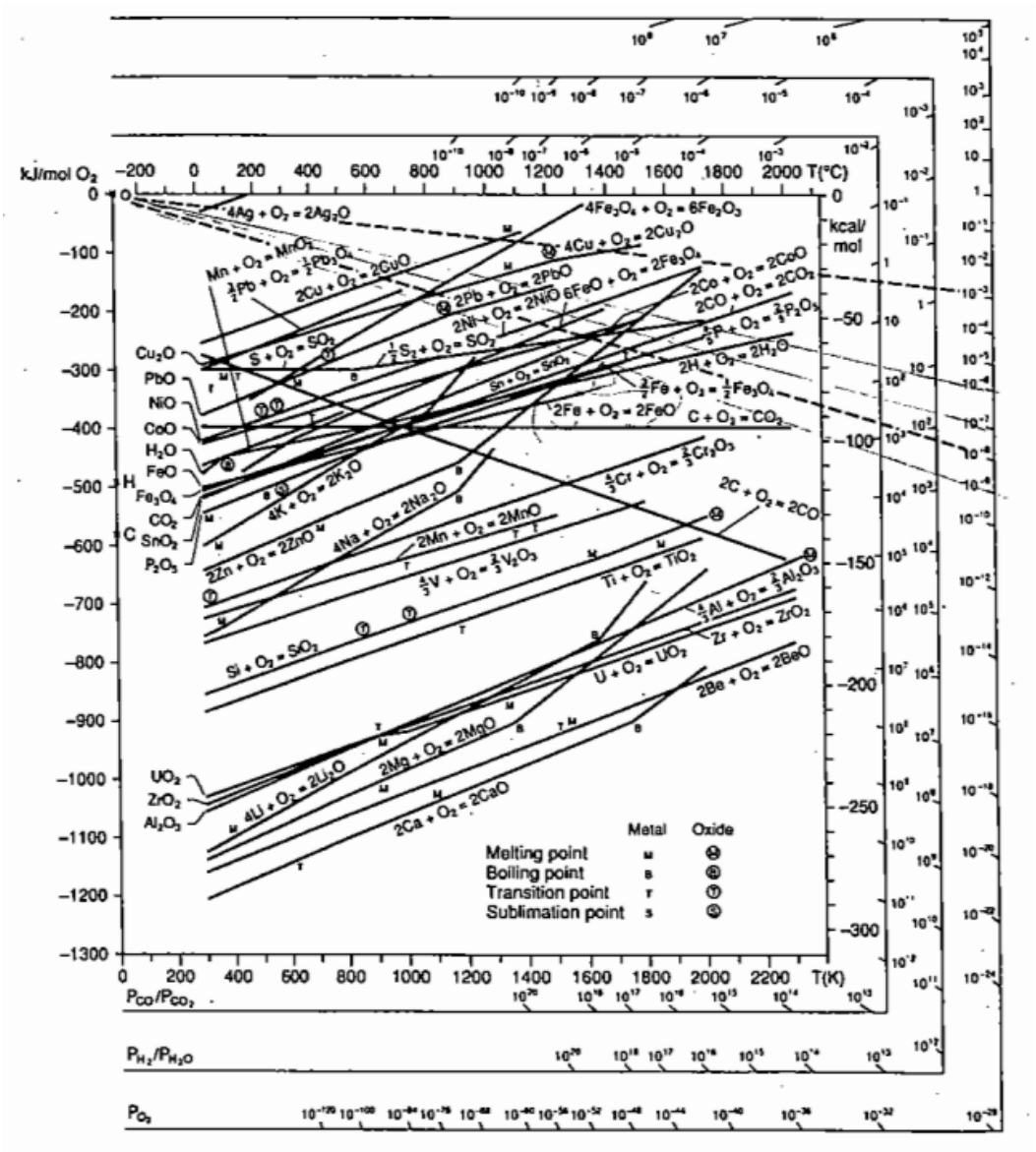

Figure 4. Ellingham Diagram for various oxides showing Gibbs standard free energies for oxidation reactions and partial pressures of oxygen [78].

Oxygen is required for the oxidation reaction. The oxygen is provided by the dielectric used in EDM, either by decomposition of H_2O due to the thermal energy of electrical breakdown in the water splitting process, shown in Equation (1), or by electrolysis of H_2O in Equation (2).

$$2\,H_2O \rightarrow 2\,H_2 + O_2 \quad (1.1)$$

$$H_2 \rightarrow 2\,H \quad (1.2)$$

$$O_2 \rightarrow 2O \quad (1.3)$$

$$OH \rightarrow O + H \quad (1.4)$$

Oxygen and hydrogen can only be directly produced via water splitting at extremely high temperatures of higher than 3000 K [80]. At 1800K and ambient pressure water vapour begins to split into a mixture of H_2, O_2, O, H, and OH, and above 3500K the constituents also split completely into O and H [81]. Even at 3000K only about half of H_2O is decomposed fully. The EDM plasma however reaches temperatures ranging from 4000 K to 8000 K [82] resulting in complete water splitting in the vicinity of the plasma channel.

Oxygen can also be supplied to the discharge gap through the electrolysis process, due to charge being carried by charge carries causing oxygen evolution. Gas bubbles form at the electrodes due to decomposition of DI when the voltage is applied due to electrolysis. This produces hydrogen H^+ (Equation (2.1)) and hydroxide OH^- (Equation (2.3)). H^+ then forms hydrogen at the cathode (Equation (2.2)), while OH^- forms oxygen at the anode (Equation (2.4)) [83].

$$2H_2O \rightarrow O_2 + 4H^+ + 4e^- \text{ (anode)} \quad (2.1)$$

$$4H^+ + 4e^- \rightarrow 2H_2 \text{ (cathode)} \quad (2.2)$$

$$4H_2O + 4e^- \rightarrow 2H_2 + 4OH^- \text{ (cathode)} \quad (2.3)$$

$$4OH^- \rightarrow O_2 + 2H_2O + 4e^- \text{ (anode)} \quad (2.4)$$

2.8 Oxides in EDM

Oxide layers are sites of potential cracks, are brittle, are prone to spalling, potentially contributing to premature part failure or contamination, have lower melting temperatures, are porous and loose, and are difficult to control. The border between oxides and the resolidified surface also has thermal and tensile gradients due to different thermal expansion and conductivity. They are also known to inhibit coating adhesion in certain manufacturing processes. Although most components of the recast layer have been studied in depth, there is limited research concerning oxides.

Oxides are generated in the EDM process when molten metal from discharges chemically reacts with oxygen in the discharge gap, either from oxygen or air in the discharge gap during dry-EDM [84], or from decomposition or electrolysis of DI into oxygen and hydrogen [43]. As DI is commonly used for hole drilling, decomposition during the EDM process can be considered the main source of oxygen necessary for oxidation of the work piece.

Following electrical breakdown of the dielectric, the discharge sites are surrounded by a gas bubble (in liquid dielectrics) and a plume (in gases) [18] as well as the entire length of the plasma channel [85], confirmed by high speed imaging of single discharges. The discharge plasma, discharge site, and molten metal, is therefore surrounded by a large amount of oxygen, which can cause oxidation of the workpiece material.

Liao et al. showed that in EDM an increase in conductivity causes a current leakage when the open voltage is applied, as shown through discharge waveform analysis. This was then attributed to electrolysis, which is known to produce gases [46]. Munz et al. also observed current leakage in EDM due to

electrolysis and observed gas generation, which ultimately led to oxide formation on the electrodes [86].

Zhang et al. studied the EDM surface and recast layer of a carbon steel workpiece in water, oil, and water-in-oil (W/O) emulsion and noted that iron oxides were only present on the surface of the water and W/O emulsions and not oil [43]. However, no iron oxides were present in the recast layer of the W/O emulsion, which was attributed to the decreased amount of water and subsequent decomposition into oxygen in the discharge gap. It was also noted that more oxides were present when machining with higher energy parameters due to the increased decomposition of the dielectric into oxygen and due to the increased local temperatures.

Through high-speed imaging of the discharge gap Wiessner et al. [18] also showed that an increase in discharge energy increased the maximum single discharge bubble diameter, which shows an increased amount of gaseous products, while Kanemaru et al. showed that it also increased the bubble lifetime till collapse [85]. The increased amount of decomposed dielectric and bubble lifetime would then lead to an increase in generation of oxides due to increased supply of oxygen, local temperatures, and total reaction time. This was confirmed by Yadav et al. who noted that lower discharge energies tended to produce less oxides while increased discharge on-times tended to increase oxides due to more time for the oxidation reaction [84]. They also showed that increasing the percentage of oxygen in the gap, through control of the gas dielectric composition, subsequently increased the percentage of oxygen in the workpiece. The material removal rate was also improved, which was explained due to the heat generated in the exothermic oxidation reaction in

the molten pool, which increased melting and temperature during both the discharge on and off-time. This was also noted by Kunieda et al. who machined using air and oxygen rich dielectrics [87], and also Zhang et al. who showed an increased recast diameter and depth of craters in single discharges in oxygen compared to air [42]. Both explained the observation by the increased released heat into the discharge gap. Similarly, Lauwers et al. who investigated the material removal mechanisms of composite ceramic materials attributed the energy released during oxidation to the increase in MRR. A Si_3N_4-TiN workpiece was compared to ZrO_2-TiN and Al_2O_3-SiCw-TiC workpieces, and the material removal rate was larger in the Si_3N_4-TiN workpiece. This was attributed to the fact that the Si_3N_4 and TiN was oxidised to SiO_2 and TiO_2, while for ZrO_2-TiN and Al_2O_3-SiCw-TiC no oxides were formed [22].

Kibria et al. who compared machining Ti-6Al-4V in deionised water and kerosene [50] found that when using oil, TiC was formed, while in water TiO_2 was formed. The higher melting temperature of TiC (3150 °C) resulted in needing a higher discharge energy to improve the material removal rate as compared to machining in water where the melting temperature of TiO_2 is 1750 °C. The increased release of oxygen was also explained to cause increased removal (overcut). This was also noted by Chen et al. who also machined a Ti-6Al-4V workpiece in deionised water and kerosene and suggested that an increase in MRR may be due to oxidation as the TiO_2 has a lower melting point and therefore requires less discharge energy in machining [44]. As well as different melting temperatures Yadav et al. explained that oxides in the EDM recast layer are more easily removed than the re-solidified material as they

are less likely to redeposit on the surface and are easier to flush away and flake off, explained due to the loose structure and lower density [84]. The recast layer also showed considerably more cracks when machining in oxygen as compared to air, due to the present oxides. Spalling is accelerated by formation of cracks on the oxide surface and also makes subsequent spalling easier. The border between the oxide and resolidified surface promotes thermal gradients and tensile stresses due to different thermal expansion and conductivity and also promotes crack formation and spalling [22, 88].

All of the above literature only briefly mentions oxides through discussion from observations, there is little in-depth literature on oxides on EDM surfaces, however more work has been done on oxides on laser drilled holes on nickel super-alloys. Oxides are common on laser drilled holes, both on the surface and as inclusions [89]. Sezer et.al. showed oxides on the surface of Nimonic 263 as well as inclusions, that were increased with slower heat transfer rates which also resulted in slower solidification rates [90]. Leigh et.al. explored the recast layer and oxides in CMSX-4 and explained that a reduction in the energy density supplied reduces the molten pool surface temperature, decreasing vapour pressure and thus molten pool ejection resulting in molten metal with longer exposure times for oxidation. It was shown that reducing the amount of oxygen particles supplied to the molten pool reduces the oxidation rate too. Gas pressure was shown to have a parabolic relationship with oxides, with low pressures having low oxides due to reduced oxygen, and high gas pressures having low oxides due to increased cooling, ejection (reduces molten metal for oxidation and increased flushing) and fracturing of the brittle oxides. Therefore it was shown that increased molten pool ejection with less

oxygen supplied produces least oxides [91]. De Luca et.al explained that Ni at 1700 °C can absorb >10 at.% oxygen and that Al, Ti, and Cri are potent oxide-forming elements, resulting in the surface oxides. Al was shown to have the highest affinity with O and so was more prevalent [92].

De Luca et.al also suggested mechanisms for oxidation of the molten pool, which was not well explored in the literature for laser melting. The oxygen was said to react with the molten pool and separates from the molten alloy, dispersing particles of molten oxides throughout the melt pool based on the strong Marangoni convention driven by the surface tension gradients. Oxides then accumulate towards the surface of the melt pool at the edges due to Marangoni forces due to the lower density of oxides, and reintroduction into the pool is prevented by bad wettability. It was explained that the solidification front may also push the dispersed oxides into the remaining molten pool, pushing it towards the surface and edges. Higher energy densities can also cause ejection of oxides.

The recast layer has been studied extensively; however, oxides have not been studied in depth, only through observations or brief discussions as part of other works. To date, no detailed analysis concerning oxide formation mechanisms in EDM has been made. The relationship between discharge energy and discharge/crater formation characteristics, as well as cooling and flushing of the spark gap, and oxides, has not been explored, only cursory observations have been made.

2.9 Improvement of the EDM surface and Introduction to Electro-chemical removal of the recast layer

Although the recast layer can be minimised through careful parameter optimisation at the penalty of reduced machining rate [47, 93-96], the recast layer cannot be eliminated from EDM surfaces without post-machining removal. Such removal methods include grit blasting [97, 98] and magnetic abrasive machining [99, 100]. These methods increase production cost considerably and the resulting surfaces may have increased roughness and embedded particles [101], which also impacts part performance.

Electrochemical machining (ECM) is an alternative non-conventional machining process which can produce high integrity surfaces without recast layers. However, in some applications such as high aspect ratio holes, EDM is preferred due to machining accuracy and higher removal rate.

Electrochemical machining occurs when a potential difference is applied across a workpiece and electrode causing current flow across a conductive electrolyte (due to the motion of ions and electrons). This current flow causes dissolution of the workpiece into the electrolyte ($Me \rightarrow Me^{n+} + ne^-$) following Faraday's Law ($m = Q/F \cdot M/z$) where m is the mass transfer, Q is the charge, F is Faraday's constant, M is molar mass, and z is electron valence. Hydrogen and hydroxide are also formed at the cathode as shown in Equation (2.3), while oxygen is produced at the anode. The metals in the workpiece give up electrons (oxidation) to the electrolyte ions (reduction), which are usually salts, and are lost into the gap. They can also form metal hydroxides when reacting with OH^- [102, 103]. Metal salts can also be formed, however these breakdown

rapidly releasing the metal into the gap. Oxide layers can also be thinned down to electrochemical removal.

Different electrolytes result in different electrochemical removal mechanisms. Passivating electrolytes contain oxidising components such as nitrates, chlorates, or sulfates, which when a current is passed transfer charge and promote the formation of oxygen/OH^- and oxide layers on the metal-liquid interface by reacting with oxygen. These salts are unable to dissolve material directly and rapidly and thus have a lower current efficiency, however are still able to breakdown the passive layer causing controlled and some pitting. In addition to oxide formation, oxygen and hydrogen evolution may also occur due to electrolysis, as the presence of oxides act as a catalyst for further gas generation as oxides are generated at lower potentials than gases. Non-passivating electrolytes, such as NaCl, do not form these oxide layers and often result in aggressive removal such as pitting by breakdown of oxide and passive layers through adsorption of Cl^- [104, 105] and are capable of directly dissolving metals. Removal is possible over the entire current density therefore current efficiency is high. There are different forms of electrochemical removal. Mass transport limited control is the movement of atoms and ions through a film layer towards the metal surface, metal-oxide interface, or oxide-liquid interface. If the layer is a viscous (too much products), salt (concentration of salts to the surface), or thin oxide film, then the limit is product removal. If there are a limited supply of salts or oxygen then the removal is reactant limited. In both of these cases the process is occurring as fast as possible and through stochastic means which can result in a polished and controlled surface. These layers form part of the Double layer, which is

when oppositely charged ions form on the electrode via adsorption and above this opposite charges attract decreasing in concentration till the bulk, forming the diffusion layer. Charge is stored and discharged in this layer, decreasing with distance, and affects electrical characteristics. In pulsed applications this layer is time varying in terms of charge and geometry and is affected by differences in gap resistances. Pitting is aggressive removal of workpiece material through accelerated removal, either when there is no formed oxide layer or through breakdown of the oxide layer and increased passage of anions to the exposed metal [106]. Electrochemical levelling is the macro scale process when a surface is levelled due to the differences in potential between peaks and valleys, which results in more removal on peaks resulting in a levelled surface. Electrochemical polishing is the micro scale process when atoms are removed through controlled means stochastically where removal is delocalised from geometry due to transport limited control, resulting in removal of defects at the scale of visible light. Polishing is thus at the micro scale compared to levelling and is controlled through surface layers.

Post-process electrolytic removal can also be used to remove EDM recast layers via electrochemical dissolution [107-109]. Once again however this approach adds significant time and cost to the overall process chain. 2-step combination processes of EDM and ECM within the same machine tool have been demonstrated to eliminate the recast layer. An example of this is a two-step W-EDM removal method where first a surface is machined with EDM to allow high bulk material removal rates, after which the gap is changed and electrolyte is used to remove the recast layer [110]. However, this setup involves a change of electrolyte and effectively combines two distinct

processes in a process chain. The adaptation to machine architecture to distribute both electrolyte and dielectric should not be underestimated.

A similar process using disks to cut material was used in a sequential EDM-ECM process on the same machine tool [111], in which the recast layer was shown to be removed via cracking at micro-cracks due to tensile stress, bubbles, and fluid flow. Once again, this process involved removal of the EDM oil and replacement with an ECM electrolyte, and therefore is a complex arrangement difficult to implement in a regular production system. It is clear that electrochemical methods are particularly effective in recast layer removal given the absence of a deformed layer from mechanical methods, or a heat-affected layer from thermal methods. It is therefore of interest to utilise the anodic dissolution electrochemical removal mechanism to produce a metallurgically ideal surface. EDM dielectrics have the potential to be exploited as a delivery mechanism for electrolyte type fluids to enable ECM and EDM in a combined process.

Processes that combine electrochemical and electrical discharges (ECDM) have been explored previously, mainly to machine non-conductive and metal-matrix composite materials [112] using NaOH, KOH, or $NaNO_3$ at high conductivities (10 mS/cm to 100 mS/cm) [113-116]. In ECDM, a gas layer is produced over the cathode due to cathodic hydrogen generation via the electrolysis of water. This gas layer then acts as a dielectric, which when in the vicinity of a non-conductive material, can cause an electrical discharge between the electrode and the gas interface which causes melting and vaporisation of the material. At the same time, electrochemical dissolution can

aid material removal. This process has also been used for the machining of conductive material in high conductivity liquids [117], however as discharges are the main mechanism of material removal, recast layers are still present on the machined surface.

In ECDM, other adaptations have been made in an attempt to reduce the size of or remove the recast layers in this combined process. The recast layer can be somewhat reduced using lower conductivity fluids (1 mS/cm to 5 mS/cm [118-122]), while Zhang et al. [123] showed some evidence that some recast layer could be removed after sufficient time. However, the evidence for this is poor and the work does not attempt to explain the mechanisms nor attempt to balance the contribution of ECM and EDM in their hybrid process to propose methods to control resulting surfaces and process characteristics. The use of EDM combined with ECM has so far only been observed in a superficial manner, with material removal rate (MRR), tool wear and macro-scale surface features being explored. However to the best of our knowledge, no attempt has been made to interrogate the impact of a conductive dielectric on the spark-dissolution balance and removal mechanisms, surface morphology, or attempt to explain process behaviour.

By combining EDM and ECM removal mechanisms in a single controllable process by use of electrolytic-dielectrics the machining steps are reduced from at minimum two to a maximum of one step, and on a single standard EDM machine with only an EDM generator. This reduces capitol cost, increases throughput, reduces optimisation steps, and can easily be retro-fitted to existing machines by replacing DI with electrolytic-dielectrics. The proposed

method also has the advantageous ability to produce high aspect ratio holes quickly with no surface damage.

Exerting control over the spark and anodic dissolution balance will hypothetically lead to the capability of producing a controlled and tailored surface with no recast layer.

3 Experimental Methodology

3.1 Machining & Equipment

Machining experiments were performed on an AgieCharmilles DRILL 20. Constant electrode rotation (36 RPM) was used to ensure even wear, machining depth, and hole profile [8]. Internal electrode flushing was used for all trials using the in-built high-pressure pump, set manually through the machine pump pressure gauge.

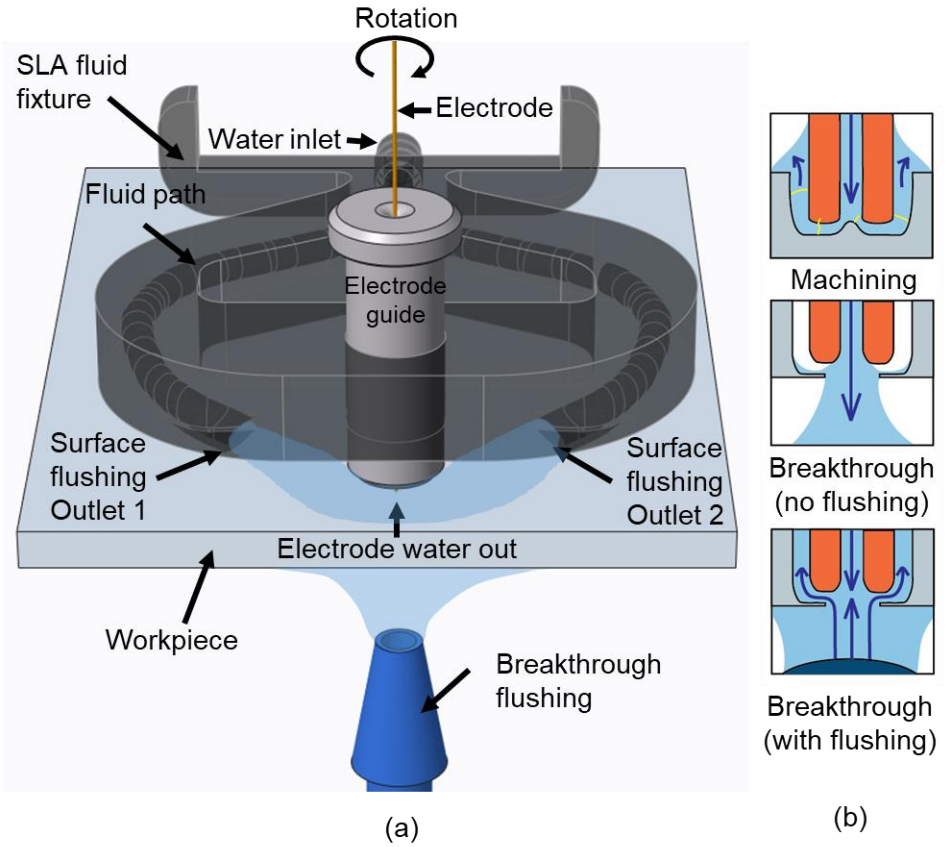

Figure 5. 0.3 mm initial oxide formation experimental set-up using a hollow brass electrode using surface and breakthrough flushing. a) Shows normal machining, b) shows breakthrough without and with breakthrough flushing.

For machining in Chapter 4 for the initial oxide formation experiment, a schematic of the machining set-up is shown in Figure 5, which shows the workpiece, electrode, and close-up of the discharge site. Surface flushing was

used to ensure that the electrode and machining surface were submerged in deionised water, by using a 3D printed SLA part with two dielectric outlets on either side of the machining site. The default machine surface flushing outlet pressure was used. This was done to ensure good entry surface quality and aid in the flushing process. A third flushing stage was used to submerge the electrode and machining site with deionised water during electrode breakthrough stage to improve flushing and machining. The dielectric outlet is placed directly below the electrode exit point beneath the CMSX-4 workpiece. This is done to reduce breakthrough time. Breakthrough is defined as the instant where the workpiece bottom surface has been opened up due to discharges, as shown in Figure 5b [124]. At this point, dielectric from the electrode exits through this hole instead of returning along the electrode back to the surface. This significantly reduces the amount of dielectric surrounding the sparking sites, thus leading to unstable sparks due to unstable gap conditions. Breakthrough flushing is thus used to introduce needed dielectric to the spark gap to improve material removal.

For all other experiments the set-up in Figure 6 is used, in which the workpiece is held in a fixture that also allows for simultaneous gas collection. In this case side flushing is used from one side and the electrode does not penetrate through the workpiece surface (blind holes). The gas collection method will be discussed later.

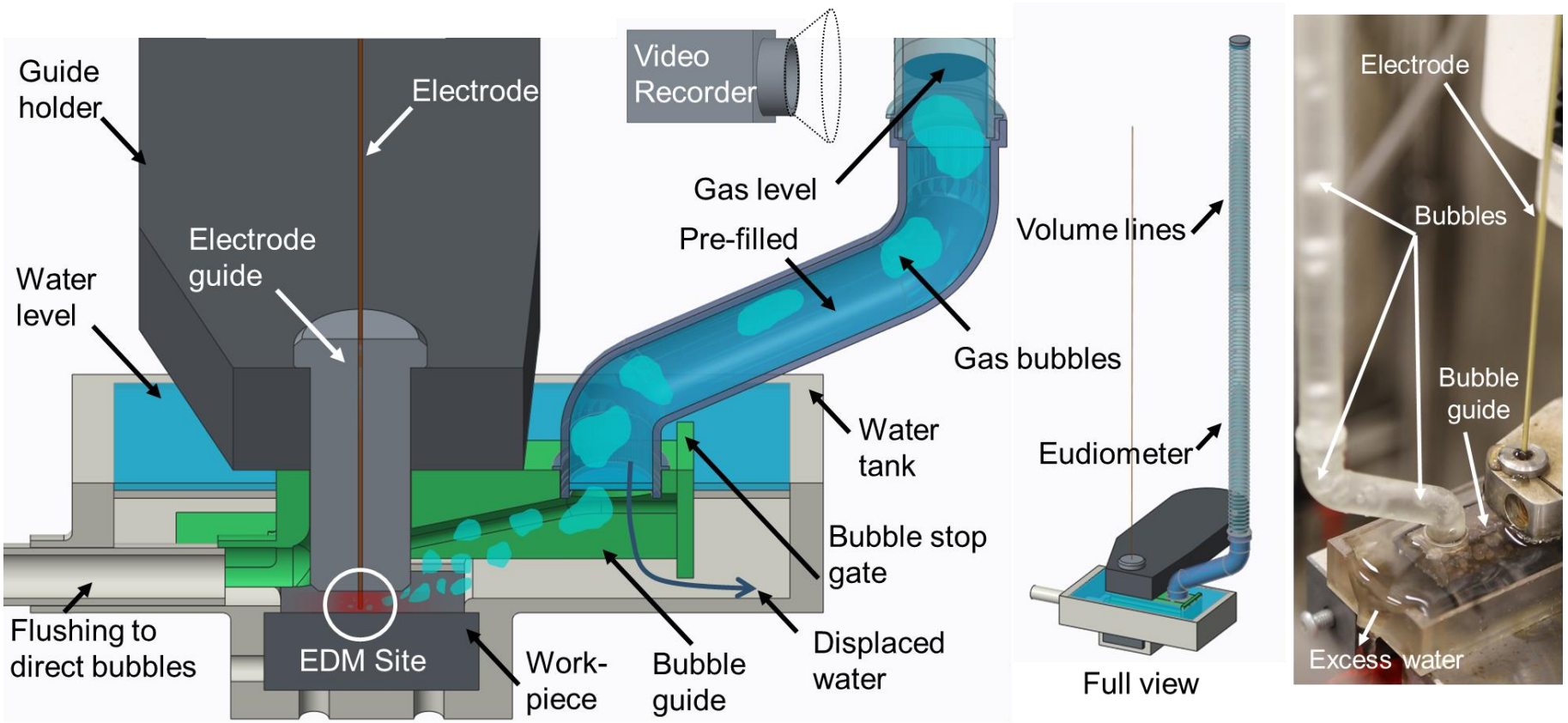

Figure 6 - Experimental set-up for gas collection. Bubble guide and eudiometer used to collect gaseous products generated from the process. Video recorder to view changes in gas level.

Deionised water (DI) of conductivity 1 µS/cm was produced using the external dielectric filtration unit on the machine, consisting of a cartridge filter (large debris), resin deionisation unit (removal of ions), and ceramic filter (removal of bacteria through pores). Electrolytic conductivity was measured using a Mettler-Toledo S3 conductivity meter before machining, which measures the response by applying a current between two electrodes.

To ensure repeatability, before each experimental run an EDM redressing step using a graphite electrode as the redressing surface was utilised to ensure that the electrode tip had no remnants from previous machining by removal of the electrode tip curvature due to previous wear. This is also done to minimise impact on breakthrough machining, as it will reduce the volume of material machined during the reduced flushing breakthrough stage, effectively shortening the breakthrough stage. If the electrode front is flat, at breakthrough the electrode will break straight through, as only a very thin layer of material is needed to be removed. If the curvature of the electrode is high, the bottom of the hole will be curved, therefore at breakthrough this curved region will need to be removed, leading to a large amount of material to be removed at this stage.

3.2 Machining Data Acquisition

Machining time was obtained from the electrode movement depth-time graphs generated by the EDM machine, an example of which is shown in Figure 7. Machining time is defined as the time from initial discharge to end of machining. For Chapter 4 this is at breakthrough, while for Chapter 5 and 6 this is when the set machining time has completed.

For Chapter 4 machining is separated into three stages, which can be distinguished by the change in gradient of the electrode advancement, as shown in Figure 7. The first is the bulk material machining stage. The second stage is when the electrode breaks through the workpiece and flushing capability is reduced causing reduced machining speed. The third stage is when the electrode has finished machining the hole and advances freely, shown through the increased electrode advancement speed. This stage can be detected through the change in electrode advance speed, frequency of normal discharges, or flushing back pressure [124], however electrode speed was chosen as it can easily be obtained and interpreted. This stage is necessary to determine machining time via depth-time graphs. Although the breakthrough stage is clear in Figure 7a, some parameter combinations, such as in Figure 7b, resulted in either unclear or near-zero length breakthrough stages. Therefore, for all machining runs the bottom of the workpiece was continuously observed until sparks were visible. The depth-time graph at this point was captured to pinpoint the exact breakthrough start time for all runs.

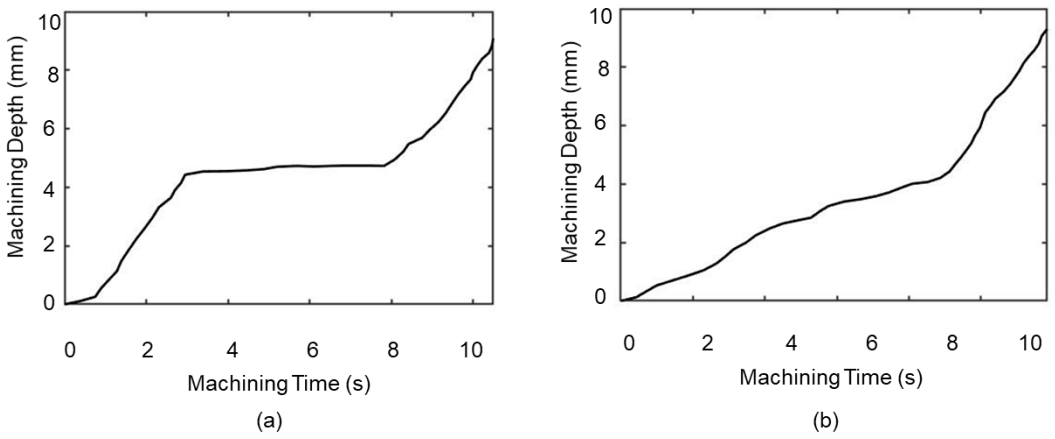

Figure 7. Example depth graphs obtained from the EDM machine. a) Depth-time graph of an example hole, showing three distinct regions: 0-3 seconds normal machining, 3-8 seconds breakthrough machining, 8 seconds finish machining. b) Shows a hole with an unclear breakthrough stage start point.

To produce accompanying hole depth with time data, which was used in Chapter 6 to correlate to gas generation, the machine Z-axis depth graphs, as shown in Figure 7, were used to produce approximate wear with time plots as shown in Figure 8. Equation (3) shows how the real depth curve was generated. z is the machine Z-axis depth, w is the electrode wear.

$$dz \propto dw \tag{3.1}$$

$$\frac{\Delta z}{Z_{end}} = \frac{\Delta w}{W_{end}} \tag{3.2}$$

$$\Delta w = \Delta z \frac{W_{end}}{Z_{end}} \tag{3.3}$$

The machine Z-axis depth change can be related to the MRR of the process, with no consideration for electrode wear. Therefore, the hole depth is recorded as larger than it is due to the additional loss of depth due to electrode wear. The actual hole depth cannot be obtained purely from the MRR data without obtaining the electrode wear. As the change in wear should be proportional to the change in MRR (as only electrical discharges remove the majority of the frontal electrode material), we can assume any change in rate of MRR is reflected as a change of rate of electrode wear. This is shown as the change in gradient in Figure 8, where a change in the gradient of the machine Z-axis is reflected in a change in the wear and the hole depth. Electrode wear was only obtained at the end of machining (method in Figure 9); therefore, intermediate values must be obtained by using the change in machine Z-axis at each step. A higher change in Z-axis shows an increase in MRR, and thus increase in wear. Equation (3.2) shows that we can equal the change in machine Z-axis at each step, as a proportion of the final Z-axis

depth, with the change in wear at each step, as a proportion of the final wear value. Equation (3.3) is then used to get the change in wear at each step. This essentially produces a wear curve that is directly proportional to the Z-axis machine depth curve.

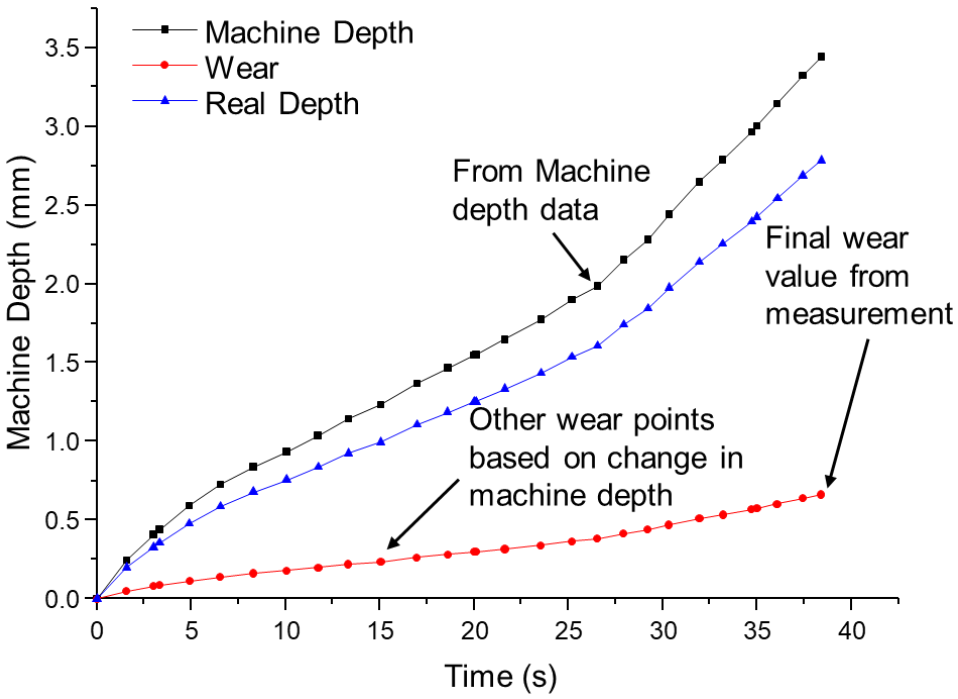

Figure 8.Showing method to calculate actual hole depth from machine depth and final wear value by considering wear to be proportional to change in MRR.

Electrode wear was measured by calculating the z-axis difference using a reference surface, before and after machining, as shown in Figure 9.

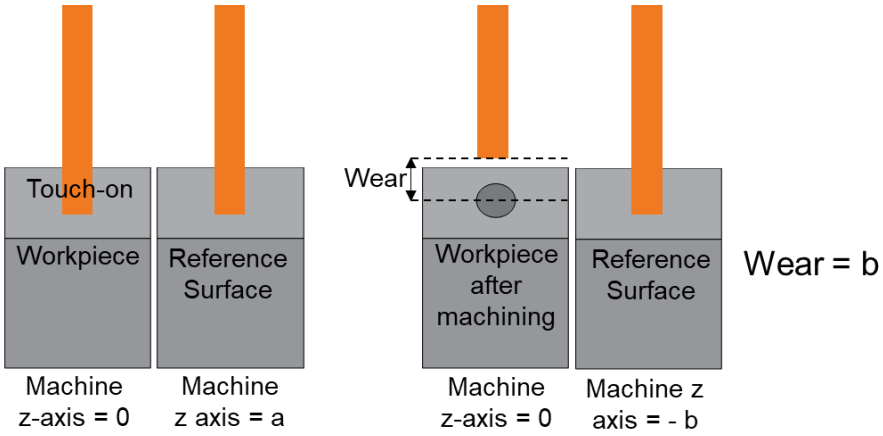

Figure 9. Method for calculating electrode end wear using a reference surface, done before and after machining.

3.3 Gas Collection and Analysis

To measure the volume of gas generated for each type of salt mixture a fixture was made to collect gases from the process, as shown in Figure 6. To control gas collection a tank was made to submerge the workpiece in dielectric. This was done to ensure no gas escape. To guide the bubbles for gas collection, a tent-like guide was made to surround the discharge site and electrode. This both ensures no gas leakage and complete submersion of the machining site to ensure no outside gases are present and enter the eudiometer. The funnelled gas then gets collected in a eudiometer tube, filled with dielectric prior to machining, which is displaced as gas fills the tube. The eudiometer tube was selected to be of a high length to diameter aspect ratio to ensure improved gas level reading, therefore the length is large in comparison to its diameter. Gas volume measurements were taken from the eudiometer tube volume graduations and for Chapter 5 volume level was recorded with a camera for more data points with time.

To measure the change in gas level with time Matlab was used. Using Matlab Video Labeller, ground truth data was produced, as shown in Figure 10. Ground truth data is data containing positive instances, for example images of correct gas levels, defined by bounding box and time locations. Approximately 200 positive labels were manually obtained. This positive data was used to train an aggregate channel features detector with 10 training stages. An aggregate channel features detector is a classic object detection detector (compared to deep learning) which compares channel pixel values (R, G, B, greyscale, transformed) of positive training data with the video it is being trained on. Positive results are matches which are close to the positive training data images selected previously, ranked according to matching scores. Negative instances are obtained during training. The trained ACF detector was then used on new gas level videos by using a sliding window to scan every frame of a video and comparing it to positive instances, distinguishing it from the background. Each detected gas level is given a confidence score. Confidence scores lower than a set threshold, which is selected manually to be high enough to not select false positives, are removed, resulting in accurate gas level measurement.

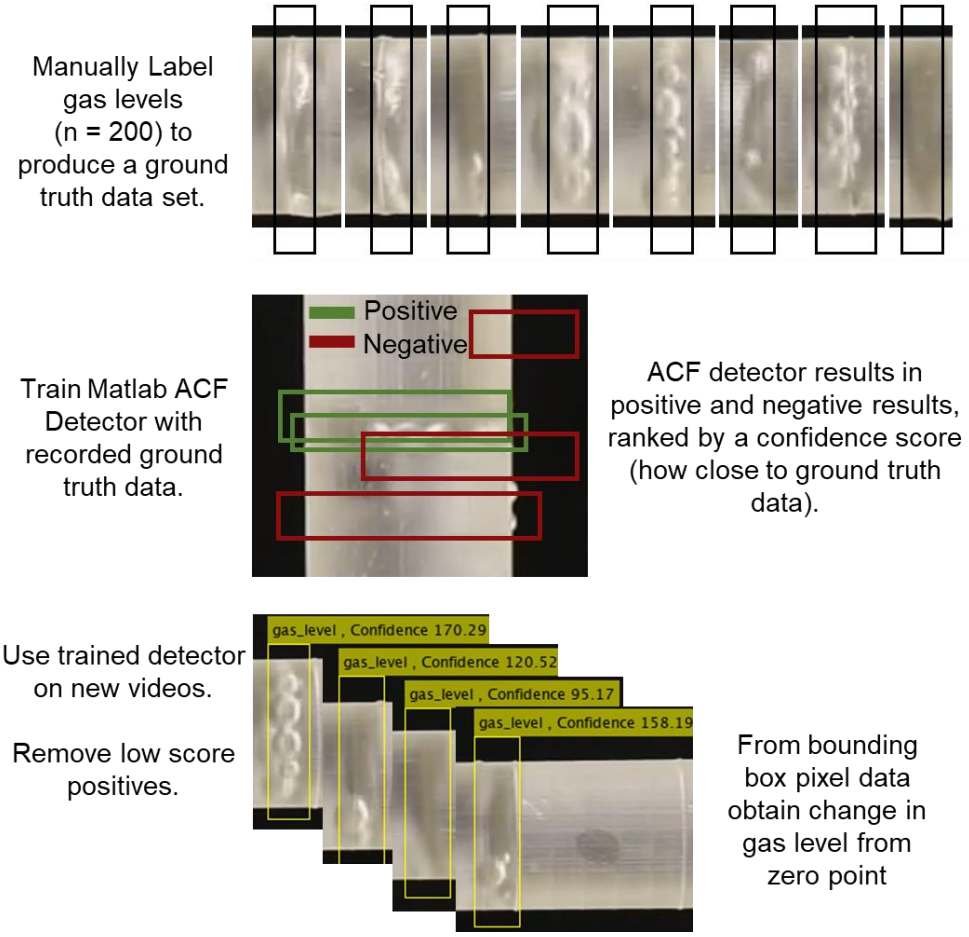

Figure 10 – Method for measuring gas level using Matlab by producing ground truth data of positive level instances and training an ACF type detector.

Gas chromatography (GC) was used to do an initial test on gas composition from EDM generated gases. Gases were produced and sealed for analysis in the GC. Gases are passed through a winding tube column carried by an inert carrier gas, through a detector. The components of the gas pass through at different rates depending on the chemical and physical properties. The Thermal conductivity detector (TCD) and the Flame ionization detector (FCD) were used. The TCD measures changes in thermal conductivity of gases and compares to the carrier gas, which is done by detecting a change in voltage due to the gas decreasing the thermal conductivity as it passes through a wire passing a current, thus increases the filament temperature and resistivity. This

is then compared to the carrier gas. The FID detects ions formed during combustion of gases, but can only detect combustible gases.. The components of the analysed gas can be detected by order in which the components reach the detector (time) while the area response shows the proportion, which must be calibrated with a sample of known concentration

3.4 Waveform Capture and Analysis

The set-up shown in Figure 11 was used to capture current and voltage waveforms. A Pearson current monitor model 150, with 0.5 V/A sensitivity was used to measure the current waveforms by producing a current proportional to the measured current due to the generated magnetic fields. A Rohde & Schwarz RT-ZD01 high-voltage differential probe with 100 MHz bandwidth at 1000:1 attenuation rating was used to measure the voltage waveforms, which measures the voltage drop across resistors. A Rhode and Schwarz RTB2000 oscilloscope with sample rate of 2.5 G sample/s and bandwidth of 70 MHz was used to process the current and voltage data.

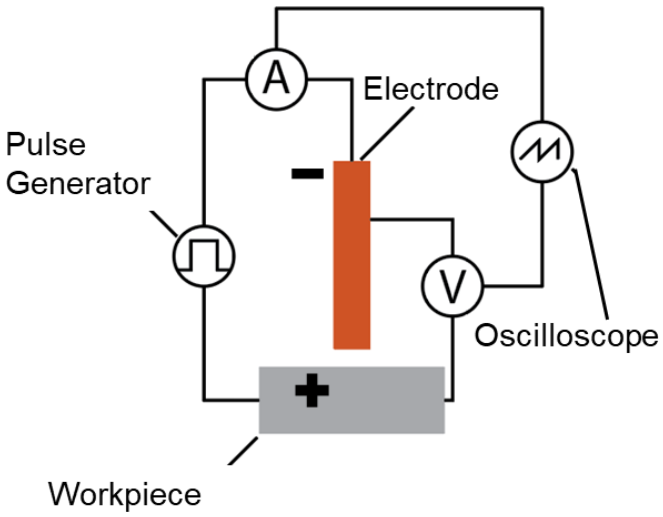

Figure 11. Showing waveform capturing set-up consisting of a current and voltage sensor and oscilloscope to view and record waveforms.

3.5 High-speed video imaging

To view discharge molten metal pool phenomena, high-speed imaging was used to prove and visually explain oxidation mechanisms. In this case machining has been conducted in air due to inability to observe the molten pool in water (due to gases).

A Shimadzu HPV-X2 high-speed camera lent by Shimadzu and used at the Kunieda lab, University of Tokyo, was used in conjunction with a microscope lens, lens filter (laser bandpass) and Cavi-Lux Smart laser control unit (HIS), laser illumination source, and focuser to view the discharge site. A NF Wave Factory WF1944B 15MHz and NF Bipolar DC BP4620 power supply and pulse generator were used to supply the single discharge pulse. A 200 MHz 2.5 GS/s Tektronix MDO3024 mixed domain oscilloscope was used to record the discharge in conjunction with a current and voltage sensor (Pearson 101 current sensor). A trigger was connected between the camera, oscilloscope,

laser, and pulse generator. Once the power supply was initiated and current starts to flow, the oscilloscope trigger switches on the laser and camera. The current, voltage, and gap-width were kept constant between all tests. A micrometer stage was used to set the gap width to 10µm. A framerate of either 1 million or 10 million FPS was used for all recordings. The electrodes were rounded to ensure sparking would occur within the camera frame.

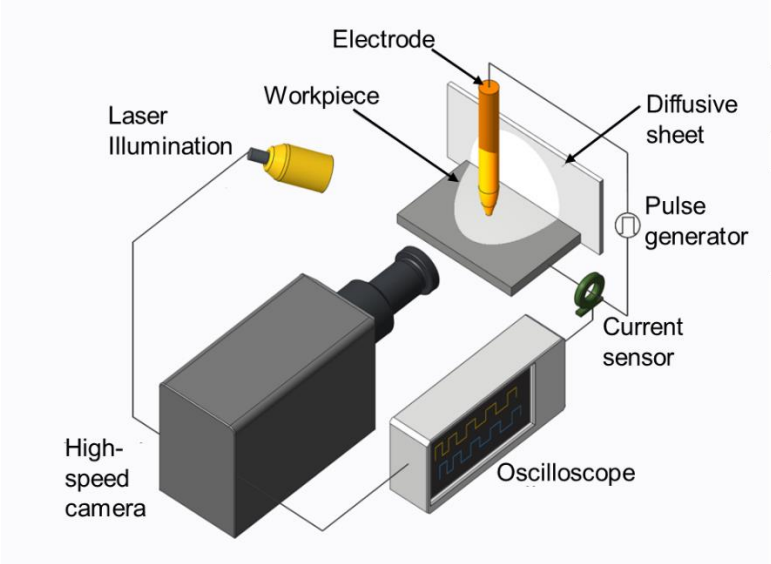

Figure 12. Shows the set-up used to view single discharges utilising a high-speed camera and laser illumination.

3.6 Sample Preparation

To view the machined surface, holes were sectioned using an abrasive cutting disk (Brilliant 220 Precision cutting) and then manually ground to reach the centre of each hole, using the fixtures in Figure 13, and resulting in holes as shown in Figure 14. The fixtures were used due to the small sizes of the samples, which could not be mounted due to affecting the EDM surface.

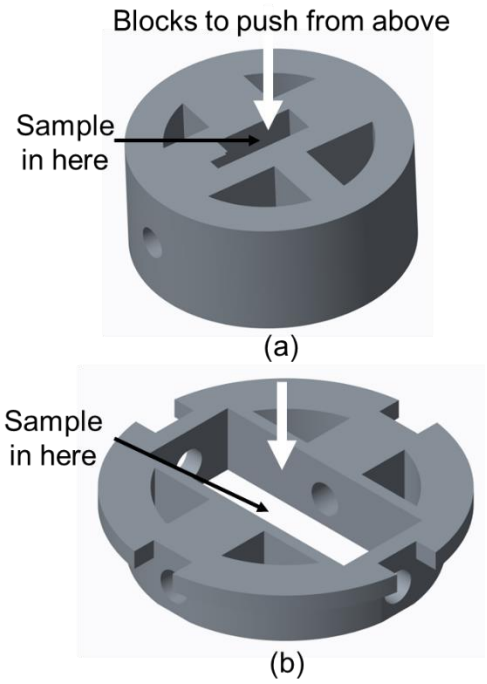

Figure 13. Fixtures to grind for recast layer analysis, ensuring flat and even polishing for small samples. (a) Used for 0.3 mm holes in 1.4 mm thick CMSX-4, (b) used for 1.9 mm holes in 20 mm thick Inconel 718.

Samples were mounted and polished to a mirror finish and then etched using V2A etchant (100 ml water, 100 ml hydrochloric acid, 10 ml nitric acid) to reveal the recast layer. Recast layer average depth measurements were obtained by calculating the recast layer area from the SEM images and dividing by the length of each SEM imaging area to obtain an average recast layer depth measurement.

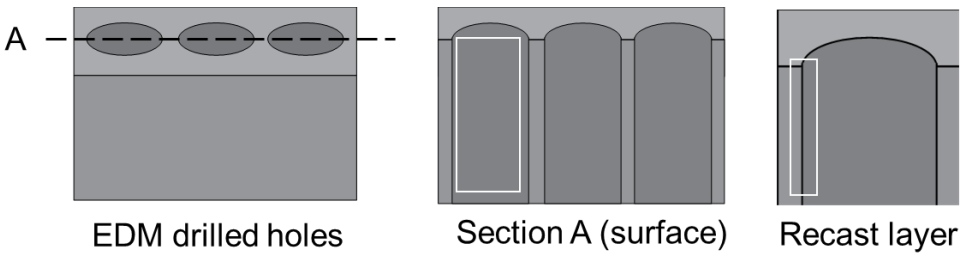

Figure 14. Showing hole geometry. Section A shows the section taken for surface analysis. Recast layer is taken on both sides of the Section A.

3.7 Sample Characterisation

3.7.1 Surface profilometry

An Alicona G4 focus variation instrument was used to image and quantify the surface roughness of the machined surface. The surface datasets were separated into roughness and waviness profiles using a Gaussian filter with cut-off 250 µm to effectively remove the hole curvature from the scanned surfaces for improved roughness comparison using the Sa, Ra, Sz, and Rz roughness parameters, which will be discussed in more detail in later sections.

3.7.2 Scanning Electron Microscopy and Energy Dispersive X-ray Spectroscopy

Backscattered (BSE) and secondary electron (SE) microscopy using the FEI Quanta600 SEM were taken of the hole surfaces to assess the surface and recast layer. Energy dispersive X-ray detectors were used for composition analysis for the identification of areas of oxides.

For the EDS spot analysis six 0.232 mm by 0.232 mm EDS spot map images were taken along each hole for the 0.3 mm holes, while 1.15 mm by 1.15 mm were taken for the 1.9 mm holes, with a 45 second scan time, accelerating voltage of 20kV, and spot size of 5. The area of oxides on the surface was obtained by calculating the area of the oxygen rich zones via EDS images by firstly binarising the images and using Matlab to calculate the total area of the oxygen rich zones, as shown in Figure 16. This method was preferred to EDS point analysis or XRD analysis as a quantitative technique, as XRD analysis isn't suitable for the amount of samples needed to analyse

(due to resources used), and EDS point analysis does not give any information concerning position of possible oxides on the surface topography, compared to EDS spot map results. X-ray Tomography could be used to calculate oxide volumes, however due to the number of hole and sample required this was not a feasible process, therefore the surface approach is a good estimate for oxides in the recast layer. Because this is a comparative study the absolute oxide area is not as important, more so which parameter has the most influence. To confirm that the EDS analysis was accurate in terms of identifying oxide rich zones, XRD analysis was performed to confirm and identify which oxide phases were present.

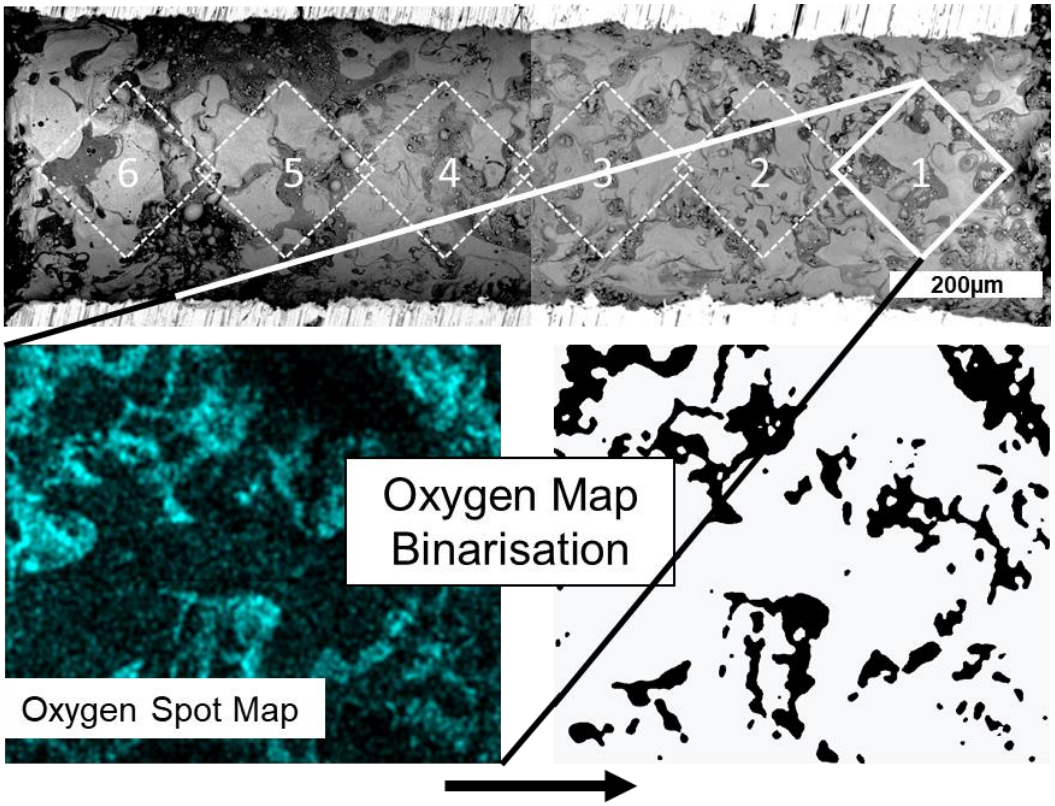

Figure 15. Showing EDS sampling regions, and spot maps produced. The Oxygen spot map was used for binarisation and estimation of oxide area. Numbers denote surface captures, 1 is the top and 6 is the bottom of the hole.

In addition to the EDS oxide analysis for oxide area measurement, the back-scattered electron SEM images were used to also calculate a surface oxide area by measuring the area of oxide regions on the surface as shown in Figure 16, which shows the same hole as Figure 15.

The oxide regions are clearly visually distinct from the bulk recast surface and confirmed to be oxide rich regions via EDS and XRD analysis. In all cases the SEM back-scattered oxide regions correlated to the oxide EDS spot maps, as shown in Section 4.2.3, therefore confirming that this method for locating and measuring oxide area is suitable. Compared to the EDS spot method for detecting oxide areas, BS-SEM images show the oxide regions more clearly and are easier to identify. The EDS spot images show oxide regions, however due to the small sample time of 60 seconds and because oxygen is a light element, the total area after binarisation and measurement of area is lower than that found with EDS imaging, as seen by comparing the binrased images in Figure 15 and Figure 16.

Following the EDS spot images of the surface, larger images of the holes were taken with BS-SEM. The oxide area (% of surface) was then calculated by first altering the BS-SEM images tonal histogram to accentuate oxide regions. The images were then binarised via Matlab’s binarisation function. This method was used for the 1.9 mm holes too.

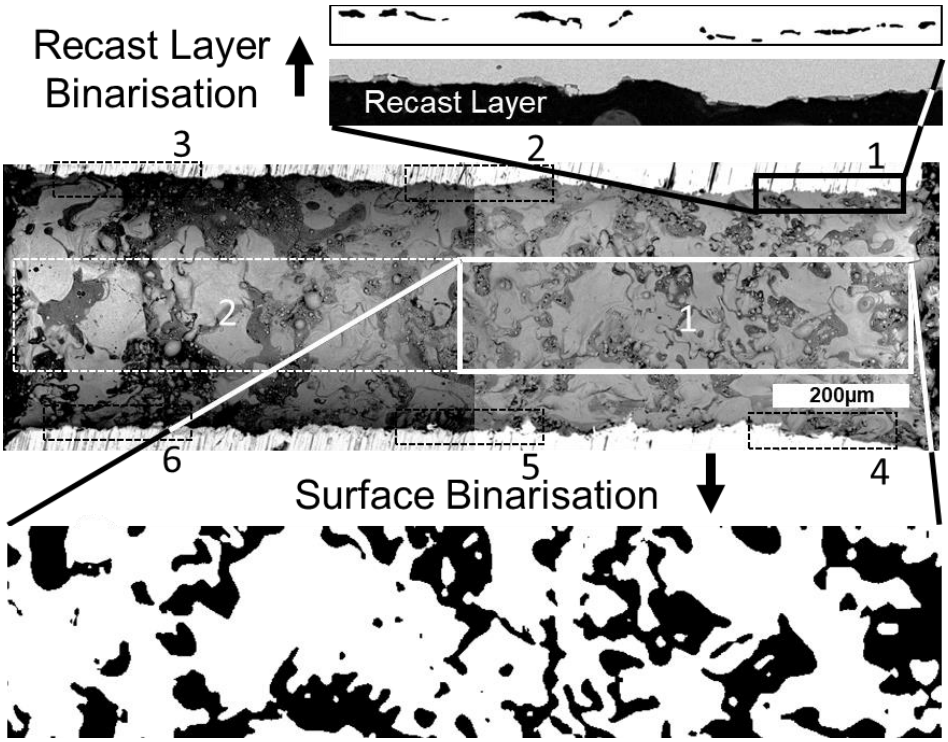

Figure 16. Showing BS-SEM sampling regions for each hole and resulting binarised image via Matlab showing oxide regions, done for the highlights areas. White numbers denote surface captures, while black numbers denote recast layer captures.

Following this, the samples were individually mounted and polished till approximately the centre of each hole, based on the entry and exit diameters. Polishing was done from 400 to 1200 grit paper, then 6 and 1 micron diamond polish, and finally with colloidal silica. These were viewed under the SEM to view the recast layer, obtain data on oxide area via EDS images, and obtain the hole diameters.

3.7.3 X-ray Diffractometry

The measurements were made using a Bruker D8 Discover Series 2 fitted with a spot-focus Cu-anode X-ray tube, a focussing poly-capillary, a Ni filter for Kβ radiation, a near-sample pinhole, a motorised stage mounted on an Eulerian cradle and a scintillation counter, scanning 2θ from 10° to 70° at a

step size of 0.05°. Samples were mounted on a plastic holder so as to not confuse aluminium peaks from the background. Measurements were made with a 0.5 mm diameter near-sample pinhole to minimise background contributions, 1 mm anti-scatter and detector slits, and a step time of 16 s. Background (a few mm away from the sample over the plate) and reference (CMSX-4 surface next to the hole) measurements were made with 2 mm diameter near-sample pinhole to maximise signal, 2 mm anti-scatter and detector slits, and a step time of 8 s. The peak positions for the reference Ni pattern have been adjusted to account for the lattice parameter difference between pure Ni and the alloy. The distraction pattern shown is after background subtraction.

4 Oxide Layers and Formation Mechanisms in EDM

4.1 Introduction

The literature showed that there is little understanding of oxide formation in EDM and no in-depth studies have been undertaken to date. Cursory observations in EDM have been made, however influence of parameters and mechanisms of formations have not been discussed. The purpose of this chapter is to understand oxide formation mechanisms in EDM, both the influence of parameters and also the fundamental discharge phenomena leading to oxides.

In order to understand oxide formation in EDM, first parameters will be altered to understand the effect on oxides on the recast surface, as well as assess the oxide measurement methods. Using this as base, fundamental oxide formation mechanisms will be explored using experimental data and linking to single discharge phenomena.

4.2 Methodology and Experimental Process

4.2.1 Initial Main Effects Experiment

The electrodes used were 0.3 mm diameter brass with a deionised water channel through the longitudinal axis, in the set-up shown in Figure 17. Brass was used due to its improved wear and MRR compared to Cu [125], as it has a higher melting point, which is factored in its erosion index (a measure of a materials suitability as an electrode) [126]. The workpiece was a 1.4 mm thickness single crystal cast CMSX-4 rectangular piece, the composition is included in Table 1 [127]. This material was used as it is commonly used in

high-temperature applications in jet engines, such as turbine blades, in the production of cooling holes. Therefore, any resulting data can be used in industry.

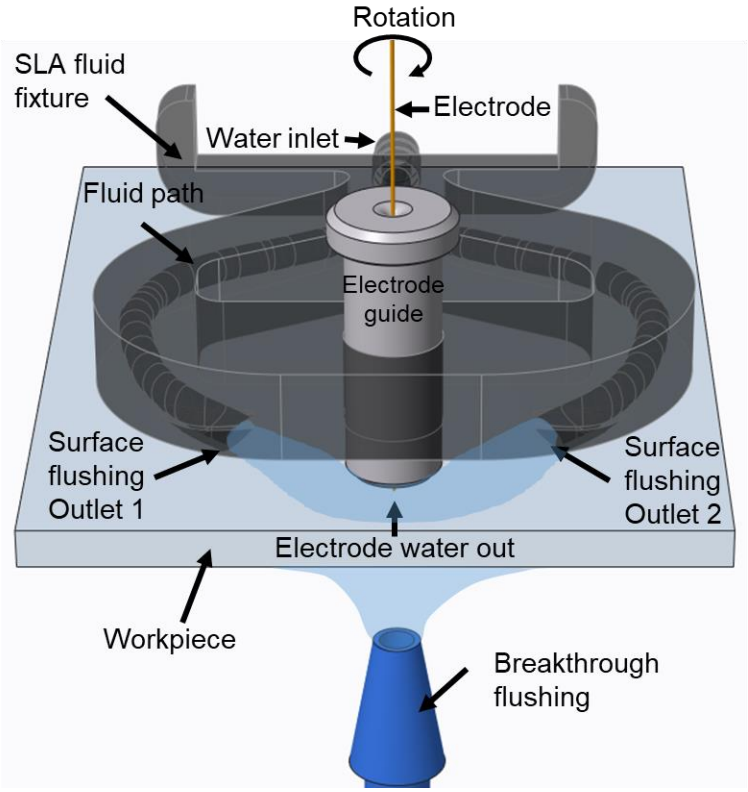

Figure 17. 0.3 mm initial oxide formation experimental set-up using a hollow brass electrode using surface and breakthrough flushing.

Table 1**.** Nominal composition of the CMSX-4 nickel super-alloy used in this study

Cr	Co	W	Mo	Ta	Re	Al	Ti	Hf	Ni
6.5	9.6	6.4	0.6	6.5	3.0	5.6	1.0	0.1	Bal

For the initial full factorial test, the factors and levels that were used are listed in Table 2 with the experiment runs listed in Table 3. These factors were chosen to alter the discharge energy and cooling during machining in order to understand the influence on oxides in the recast layer. The levels of the factors were based on standard parameters used for EDM drilling of nickel super-

alloys, which consist of short discharge on and off-times. They were also selected for minimum machining time and wear, from previous experimental work, in order to ensure machining relevancy to industrial manufacture. The on-time, off-time, and current were doubled to ensure a large change in oxides on the surface to ease analysis as ensuring a maximum duty factor of 50 % for stable machining, and the pressure was changed from 6 MPa to 9 MPa, which is the maximum pressure in the current set-up. The factors that were fixed were the conductivity of the deionised water, electrode diameter, electrode rotation speed, electrode advance speed, surface flushing pressure, and breakthrough flushing pressure. Experimental output factors are machining time (s), wear (mm), surface oxide area (%), recast layer oxide area (μm^2), surface roughness Sa (µm), and breakthrough proportion (%). To reduce experimental runs and the resulting surface and recast layer analysis a full factorial design with two repeats was used, totalling 32 experimental runs.

Table 2. Experimental factor levels used in the initial mains effect experiment

On-time (µs)	**Off-time (µs)**	**Current (A)**	**Internal Pressure (MPa)**
5	5	9	6
10	10	19	9

Table 3. Full list of experimental runs in full factorial experiment with two levels per factor with two repeats.

Run	Current (A)	On-time (µs)	Off-time (µs)	Pressure (MPa)
1	19	5	10	9
2	9	10	5	9
3	9	10	5	6
4	19	5	10	6
5	19	5	5	6
6	9	10	10	6
7	19	5	5	9
8	9	10	10	9
9	9	10	10	6
10	9	10	10	9
11	19	5	5	9
12	19	5	5	6
13	9	5	5	9
14	9	5	5	6
15	19	10	10	6
16	19	10	10	9
17	9	10	5	9
18	19	5	10	9
19	9	10	5	6
20	19	5	10	6
21	9	5	10	9
22	9	5	10	6
23	19	10	5	9
24	19	10	5	6
25	9	5	5	9
26	19	10	10	6
27	19	10	10	9
28	9	5	5	6
29	9	5	10	9
30	19	10	5	6
31	9	5	10	6
32	19	10	5	9

Due to the small size of the holes a custom fixture was used to prepare the sample for analysis. A cutting disc was used to cut near the hole, after which

the custom fixture was used to hold the sample for manual grinding until the inner surface was exposed.

An area of 1.2 mm by 0.1 - 0.2 mm was used to assess the surface roughness, depending on resulting hole size, using the Alicona G4 focus variation instrument. The Sa surface roughness parameter was used to obtain a general roughness value, which is based on the difference in height of each point with the mean surface height.

Energy was calculated by Equation 4, where the average machining voltage for each current parameter was used and power was calculated by correcting for time (J/s, or the differential of energy wrt time).

$$E = \int_0^t u(t) \cdot i(t) \cdot dt = U \cdot I \cdot t \quad (4)$$

4.2.2 Detailed Parameter experiment

The electrodes used were 1.9 mm diameter brass with a deionised water channel through the longitudinal axis. Larger electrodes were now used due to difficulty in sample preparation and analysis associated with the small 0.3 mm holes. The electrodes used were 1.9 mm diameter brass, due to its lower wear and improved MRR compared to Cu [125], with a multi-hole deionised water channel to ensure no central material remains after machining. The set-up shown in Figure 6 was used. The workpiece was an Inconel 718 rectangular piece (nominal dimensions 25 mm by 25 mm by 10mm), which is used in high-temperature aerospace applications due to its resistance to corrosion and

good high-temperature properties [128, 129]. The nominal composition of Inconel 718 is listed in Table 4.

Table 4 - Nominal composition of Inconel 718**.** Inconel 718 workpiece used in all experiments. Composition also used in ECE calculation.

Element	**Ni**	**Cr**	**Nb**	**Cu**	**Mo**	**Ti**	**Al**	**Co**	**Ta**	**Si**	**Mn**	**Fe**	**Total**
Min Wt %	50	17	4.75	0	2.8	0.65	0.2	0	0	0	0	24.6	100
Max Wt %	55	21	5.5	0.3	3.3	1.15	0.8	1	0.05	0.35	0.35	11.2	100

Table 5 shows the experimental factors used in the experiment. Six levels of each factor were used with 3 repeats per level totalling 72 runs. For on-time, the hold parameters were 19 A current, 10 µs off-time, and 5 MPa pressure. For off-time, the hold parameters were 19 A current, 5 µs on-time, and 5 MPa pressure. For current, the hold parameters were 5 µs on-time, 10 µs off-time, and 5 MPa pressure. For pressure, the hold parameters were 19 A current, 5 µs on-time, and 10 µs off-time.

Table 5. Experimental factor levels used in the detailed parameter experiment, with 3 repeats per parameter.

On-time (µs)	**Off-time (µs)**	**Current (A)**	**Internal Flushing Pressure (MPa)**
5	5	9	1
20	20	19	2.5
40	40	25	4
60	60	29	5.5
80	80	34	7
99	99	38	8.5

4.2.3 Constant energy Experiment

To understand the influence of impulse force on crater morphology and resulting oxides, an experiment to use parameters at the same energy was conducted. The impulse force is the force acting on the molten pool due to the changing pressure gradients, in this work the term impulse force is instead used as it is commonly referred to as this in the literature for EDM, The set-up shown in Figure 11 was used to capture waveforms of different parameters. In this case, the EDM hole drilling machine was not capable of fine-tuning of parameters to obtain same parameter energies, therefore a Mitsubishi Electric EA12 V die-sinking EDM machine with a custom tank to hold DI was used. By varying parameters and calculating the resulting energy using Equation (4) in Matlab a set of parameters with near similar energy can be found, as shown in Figure 18 showing an example of voltage and current waveforms for a single pulse and the resulting power, for two parameter sets. The energy was calculated by multiplying the instantaneous current and voltage to produce a new plot, then taking the integral of that curve to get the energy.

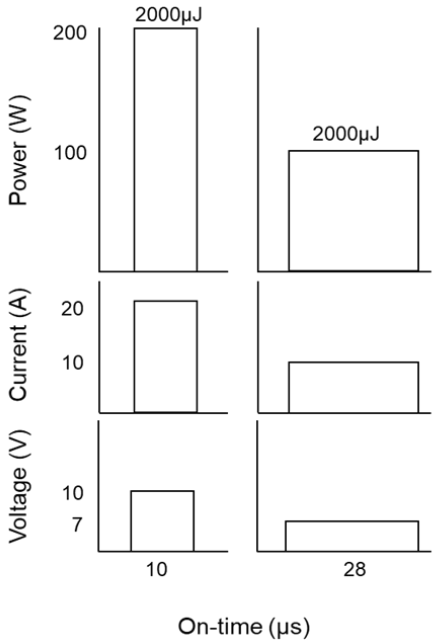

Figure 18. Example of different parameters with same energy, with parameters obtained from using the waveform recording set-up consisting of a current and voltage sensor and oscilloscope to view and record waveforms.

4.3 Results

4.3.1 Oxide area measurement

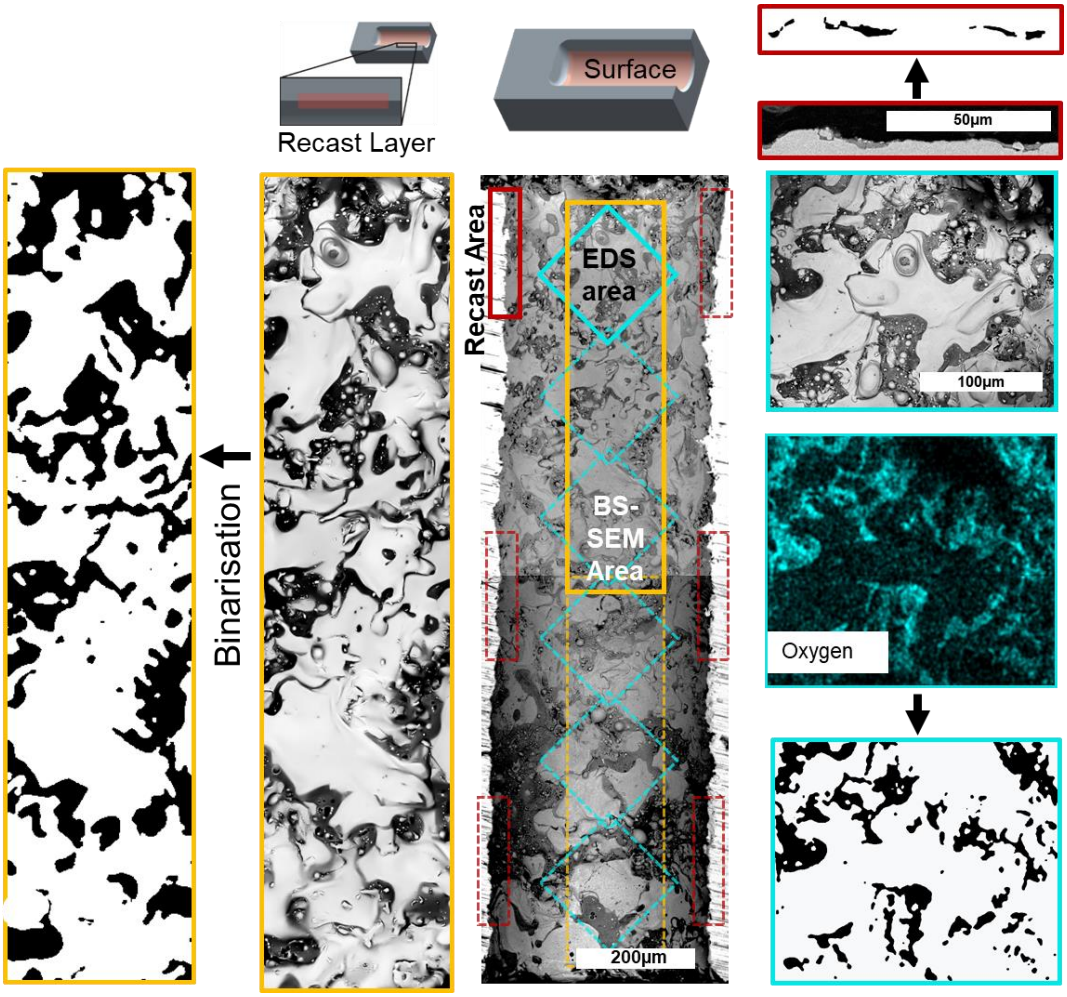

Figure 19. Example of a hole (19 A current, 5 µs on-time, 10 µs off-time, 9 MPa pressure) showing the BS-SEM surface. The area taken for the EDS (blue), BS-SEM (orange), and recast layer (red) binarisation is shown overlaid on the BS-SEM image of the hole surface.

Figure 19 shows an example of one of the holes machined in the experiment, to show the outputs of the oxide area data and analysis methods visually. The parameters used were 19 A current, 5 µs on-time, 10 µs off-time, and 9 MPa pressure. The figure shows the 3 types of output oxide area images produced for the hole surface and recast layer, with the sampling regions shown in blue (EDS images), orange (surface BS-SEM image), and red

(recast layer BS-SEM images). This was done for all experimental runs. Via EDS spot maps of oxygen, six oxide area images are produced. Two large area oxide images are produced via using the BS-SEM images. Similarly, six recast layer oxide area images were produced using BS-SEM images of the recast layer.

Figure 20 shows the SEM backscattered electron mode of the surface of the drilled hole after sample preparation. By using backscattered electrons, it is possible to visually distinguish between elemental compositions of the recast surface. The darker regions were seen to correspond to regions of increased oxygen content, while the lighter regions were similar in composition to the bulk material. This was the case for all analysed holes showing similar contrast differences. EDS maps were produced, which included detecting the elements shown in Table 1 and oxygen for oxide detection. Figure 20 confirms that the darker regions have increased oxygen content and decreased nickel content than the lower count regions. Similarly, the other elements that constitute CMSX-4 also had reduced count in these regions, except for cases of increased aluminium (Al), titanium (Ti), tantalum (Ta), and chromium (Cr). This indicates that the possible oxides could be a combination of Al, Ti, Ta, and Cr.

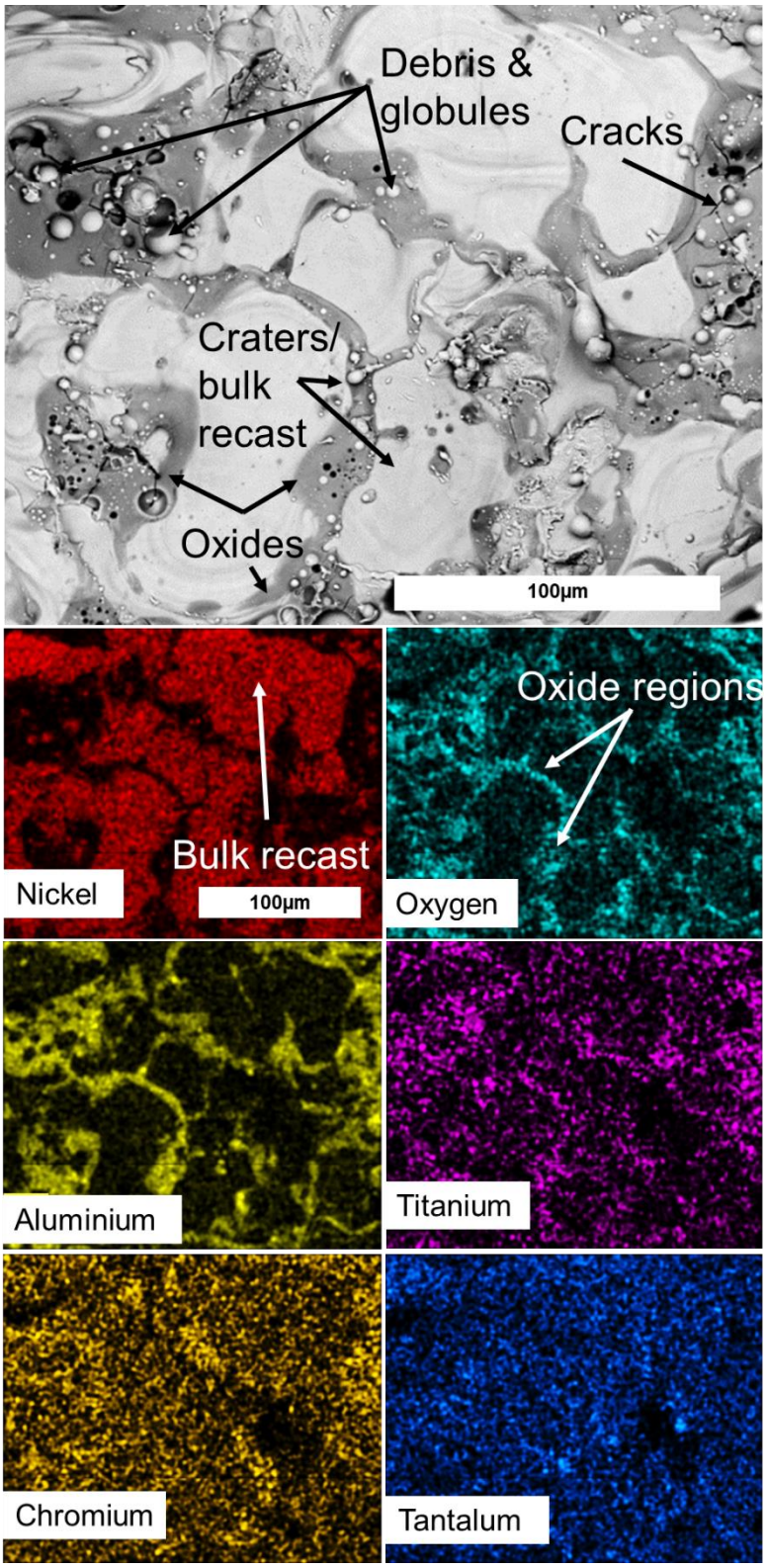

Figure 20. SEM images showing the EDM surface and recast layer. Top showing BS-EDM image of the surface showing clear oxide zones. Below are the EDS spot maps of significant elements showing the nickel, oxygen, aluminium, titanium, and chromium,

XRD analysis was used to confirm the presence and phases of these oxides. Due to the limitations of the XRD equipment, it was not possible to use the 0.3 mm holes drilled in this experiment to confirm the oxides; therefore separate 3 mm holes were drilled for the XRD analysis. The SEM surface of the 3 mm and 0.3 mm holes were similarly present with oxide regions and preliminary EDS analysis showed similar results to the 0.3 mm holes (regions of increased Al, Ti, Ta, Cr, O, and oxide geometry) as shown in Figure 21. For the XRD experiment a sample with a higher amount of surface oxides was used to make it easier to detect oxides, this is also shown in Figure 21.

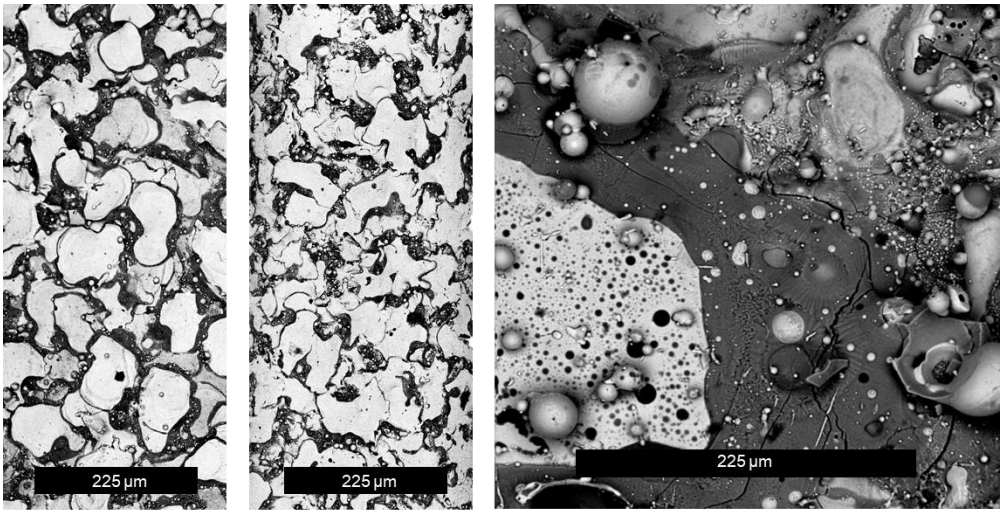

Figure 21. Showing similarity between 3 mm and 0.3 mm holes on surface oxide geometry. Right: an example of a high oxide hole used in XRD oxide analysis.

From XRD analysis, possible oxides were $TiTaO_4$, $CrTaO_4$, $AlTaO_4$, TiO_2, TaO_2, $NiTa_2O_6$, and Al_2O_3. They have similar crystal structures (space groups 102 or 136, Tetragonal) but vary in their metal components and therefore lattice parameters leading to the spread of peak positions. The variety in formulae suggest fairly free substitution of the metals in this phase, so it may contain a mixture such as $(Al, Ti, Ta, Cr)O_2$. By referring to the EDS spot maps,

which contain concentrated regions of aluminium, titanium, chromium, and tantalum, it can be confirmed that oxides of these metals are present in the samples by comparing to XRD data.

From Ellingham diagrams it can be seen that Al has the highest oxygen affinity due to the lowest Gibbs Standard free energy in kJ mol^{-1} until 2000 K [79, 130, 131]. Al was shown to have a higher likelihood more so than Ni or the other elements in CMSX-4. This is reflected in the EDS analysis which shows more EDS counts for aluminium in the oxide regions, and limited nickel oxides. Al is followed by Ti, then Ta and Cr in terms of oxygen affinity. In some other studies of high temperature oxidation of nickel super alloys Al, Ti, Ta, and Cr oxides were also found [47, 132, 133].

Figure 22 shows two holes as a comparative example of the effect of discharge energy and cooling parameters. Hole 1, as shown in Figure 22a,c, is described as low energy and high cooling, while Hole 2, as shown in Figure 22b,d, is described as high energy and low cooling. For Hole 1 the discharge current was set to 9 A, on-time to 5 µs, off-time to 10 µs, and internal pressure to 9 MPa. Hole 2 was set to 19 A, on-time 10 µs, off-time 5 µs, and internal pressure to 6 MPa. From the SEM back-scattered electron images, it can be seen that the darker oxide regions are larger in area in Hole 2, compared to Hole 1. One of the six EDS map images per hole is shown in Figure 22c & d. This shows the large difference in oxides due to the changes in parameters. Over the six EDS spot maps taken of the surface of the two holes, for Hole 1 the oxide area was calculated as 13% (using the oxygen EDS maps) while for Hole 2 the oxide area was calculated as 23%. By using the back-scattered electron SEM images the oxide area for Hole 1 was 36% while Hole 2 was

55%. Both methods show a similar increase, however with different magnitudes due to the method of data collection.

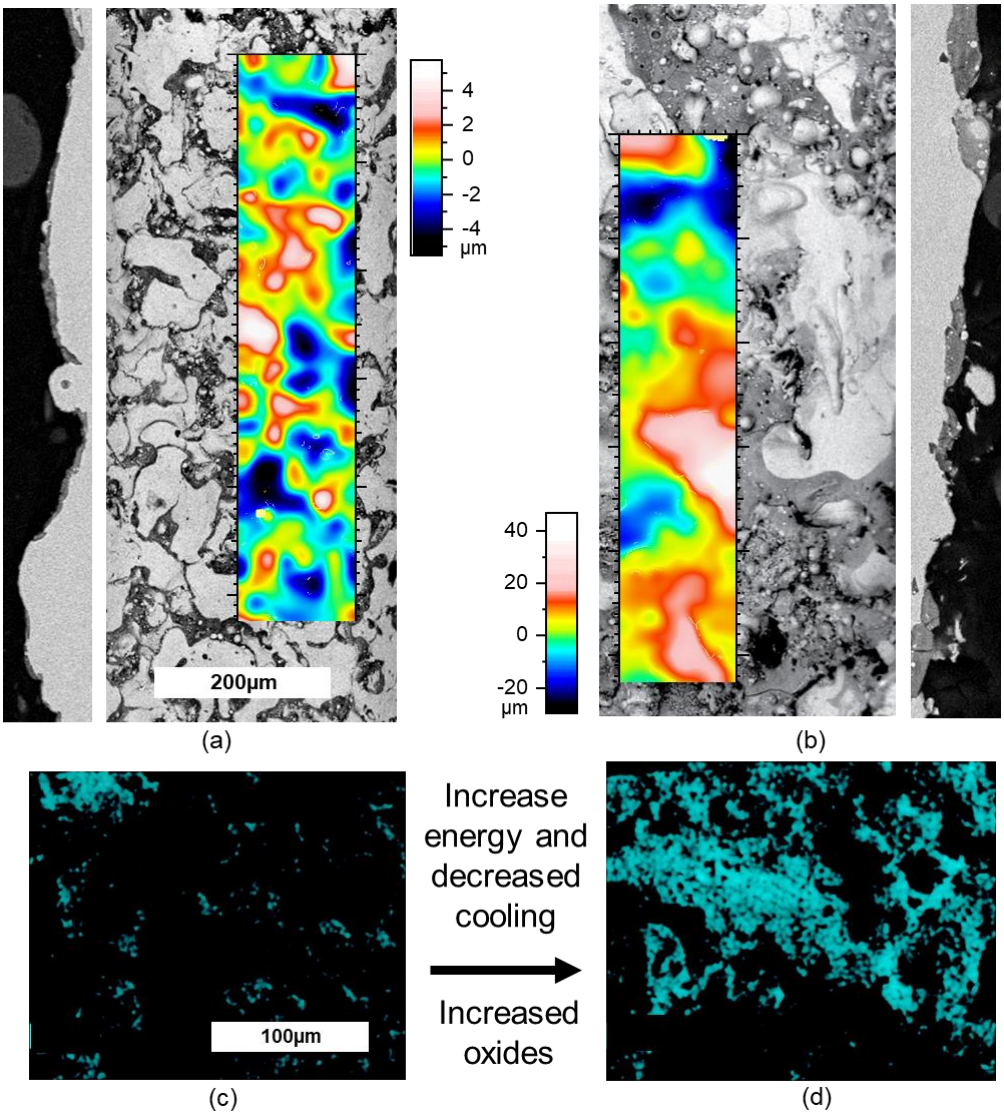

Figure 22. Shows a comparative example of effect of increasing discharge energy and decreasing cooling. a) Shows a low energy high cooling hole. b) Shows a high-power low cooling hole. c) Shows the Al EDS maps of the surface of a). d) Shows the Al EDS maps of the surface of b).

4.3.2 Initial Main Effects Experiment

Figure 23 shows the results of the full factorial experiment analysed in Minitab statistical software. Figure 23a shows the main effects plots for surface oxide area percentage via the oxygen spot EDS map method, Figure 23b

shows the main effects plots for surface oxide area percentage via the BS-SEM method, and Figure 23c shows the recast oxide area in μm^2 via the BS-SEM method. The spot EDS oxygen map method for assessing oxide area shows very similar trends and main effects to the BS-SEM method thus showing that either method is suitable for assessing oxide area and the influence of parameters. The BS-SEM method is more reflective of actual oxide area as the EDS spot map method has reduced spot counts due to small scanning times (45 seconds) and due to oxygen being a lighter element, which is harder to detect using EDS. As the regions of darker tone (change in contrast) on the BS-SEM images correlate to regions of oxides, it is possible to easily link the surface topography to oxides, hence it is more suitable for this analysis as it shows all regions of oxides in a short scan time. The relation of oxide area for both the surface and depth are also similar in terms of effects of EDM parameters. However it is not possible to take several cross sections of the same hole due to the small size, therefore a single cross-section is not precise and may not be accurate compared to surface SEM and roughness data which produce data over the entire surface and therefore surface SEM oxide measures a necessary compromise. X-ray Tomography could be used to calculate oxide volumes, however due to the number of holes and samples required this was not a feasible process, combined with the difficulty to measure micron thickness oxide layers. Therefore the surface approach is a good estimate for oxides in the recast layer. Therefore, the BS-SEM method was used from this point to assess oxide area on both the surface and recast layer. This method is also more suitable for this experiment as it is significantly

quicker to obtain data compared to the EDS spot map method, thus resources spent on the SEM machine are reduced.

In both Figure 23a,b, we can see that an increase in current and on-time increases the surface oxides, while the off-time and pressure decreases oxides. The mean change in oxide area in Figure 23b, for current, ranges from 39 % to 46 %, similarly for on-time. Off-time and pressure have a smaller magnitude of mean change ranging from 41 % to 45 %. Figure 23c shows that on-time is the most significant factor for recast oxide area, with a mean change from 118 μm^2 to 170 μm^2, followed by current, off-time and pressure. The current and on-time contribute to increased energy (increased gas, molten metal, vapour, and temperature) and alter molten pool characteristics (ejection of molten material or increased exposure), which lead to increased oxides, and will be explained in Chapter 4.4.1 and 4.4.2. The change in off-time results in reduced oxidation rate (reduced molten metal and temperature) and also increase removal of debris, gases, and a reduction in temperature.

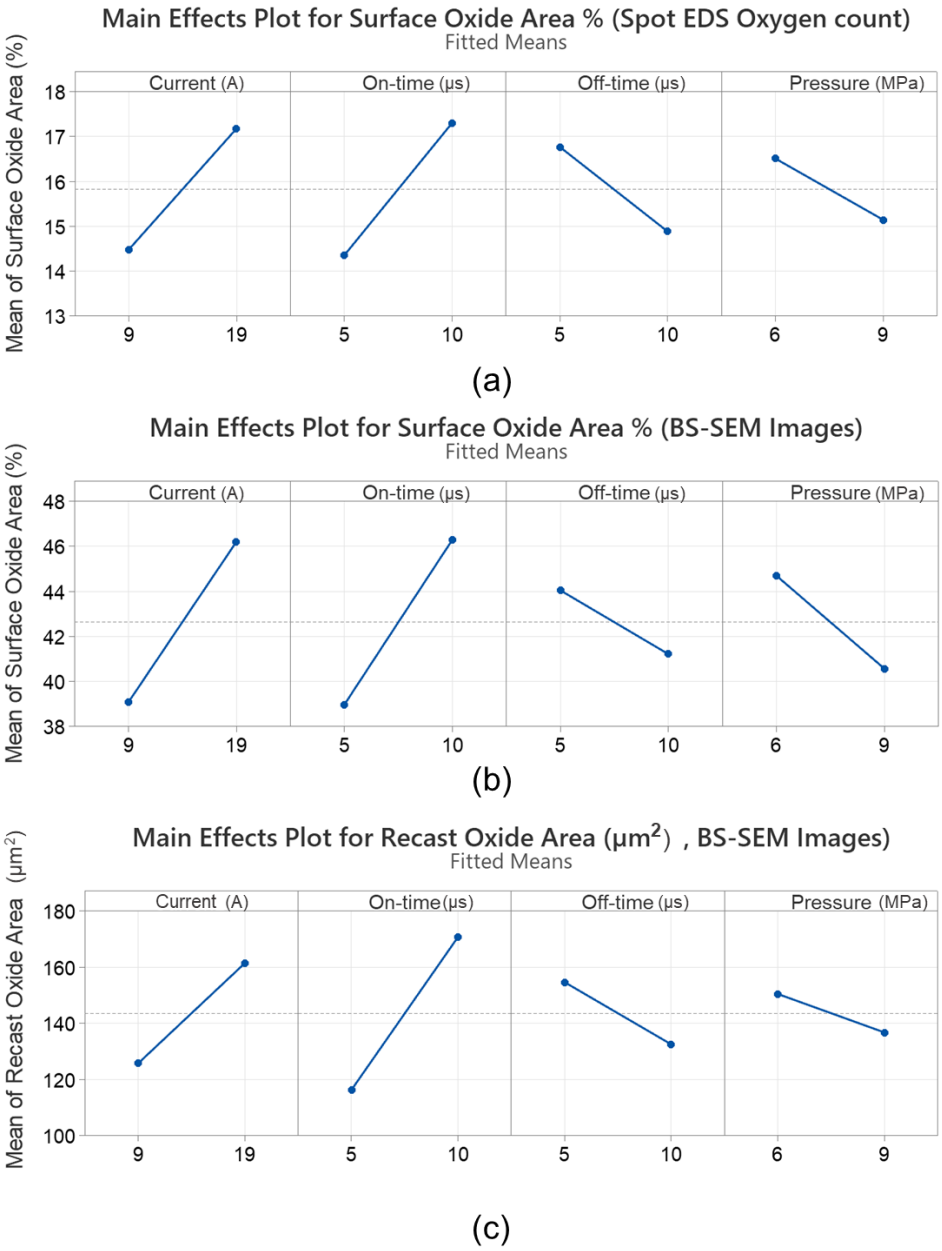

Figure 23. Plots showing main effects of parameters and influence on oxide area. (a) shows the effect on surface oxides using the EDS oxygen spot map, (b) shows the effect on surface oxides by using BS-SEM images, and (c) shows the main effects plot of the effect on recast oxide area using the BS-SEM images.

Figure 24 shows the main effects on machining time and wear. It was shown that current and flushing pressure significantly decreases machining time, while off-time increases machining time, and on-time has a slight increase. Current decreases machining time due more energy removing material. An

increase in on-time should also decrease machining time, however in this case there is a slight increase, which may be attributed due the increase in duty factor (amount of on-time compared to off-time) which causes decreased flushing of debris resulting in unstable machining. In theory an increase in on-time should decrease machining time, only if a suitable off-time is then used (to produce a duty factor of 50 % or higher). Wear was shown to increase significantly with current, due to increased energy melting and vaporising the electrode material, followed by off-time, while on-time had a slight decrease and pressure had no effect. On-time reduced wear slightly due to less individual discharges removing material from the electrode (lower energy density with time). An increase in off-time increased the wear, which is unexpected as it should not affect wear to that extent. This could also be due to the change in duty factor which was not assessed in this study.

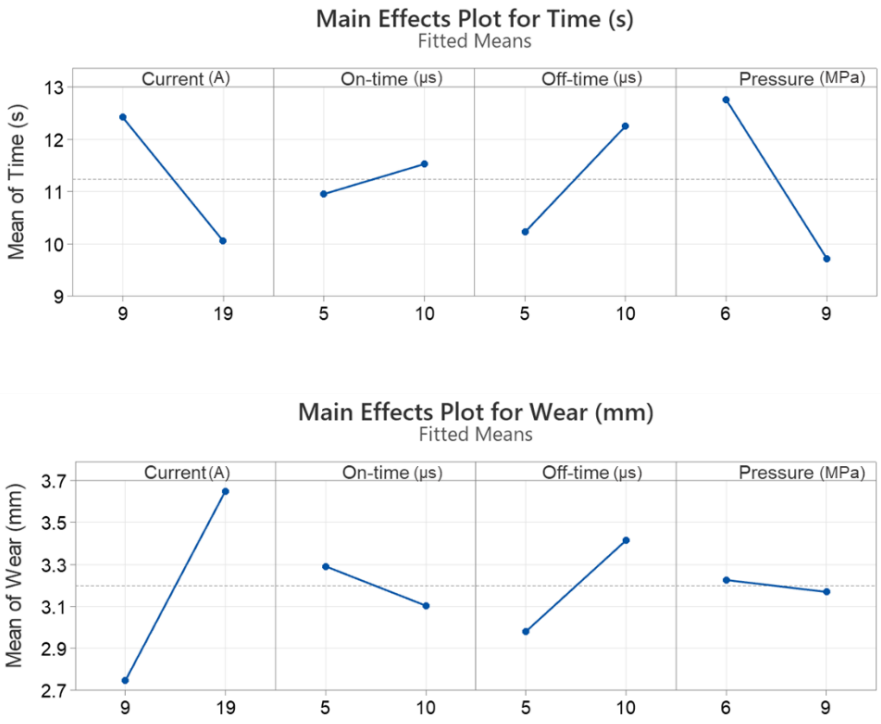

Figure 24. Main effects on machining time and wear of current, on-time, off-time, and pressure.

Figure 25 shows the main effects on breakthrough percentage and surface roughness. It was shown that only flushing pressure has an influence on breakthrough percentage, which can be attributed due to the increased pressure causing electrode vibrations and instability. The other parameters did not have an effect, although at higher values if current and on-time an effect on breakthrough percentage is expected. Surface roughness was increased by current and on-time due to increased material removal, while pressure decreased roughness and off-time showed a small decreasing trend due to increased material evacuation leading to stable machining and removal of molten debris.

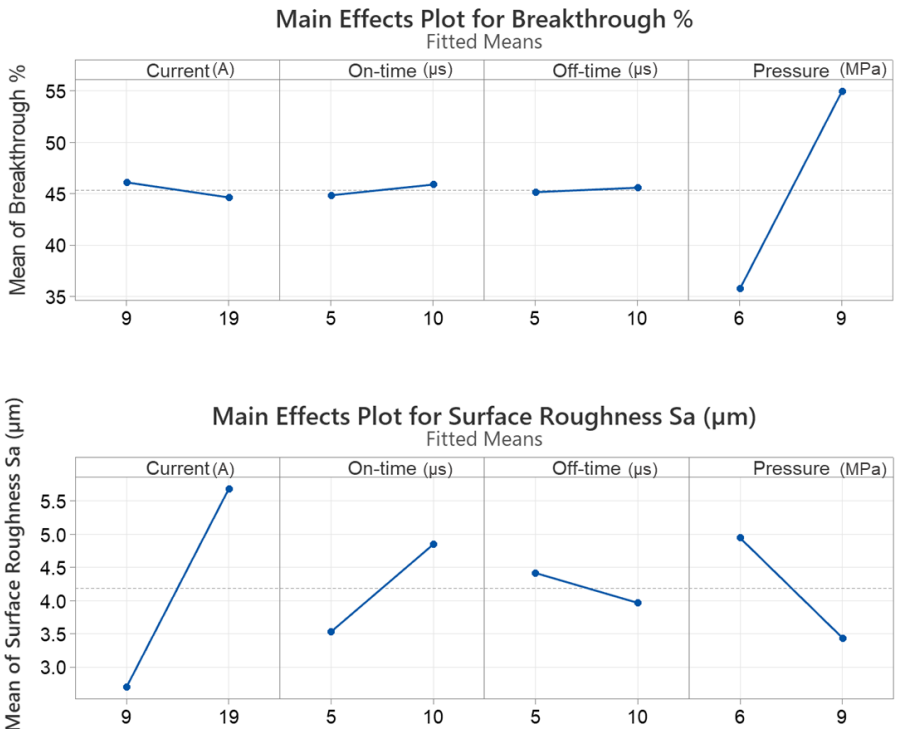

Figure 25. Main effects on breakthrough percentage and surface roughness of current, on-time, off-time, and pressure.

By calculating the power for each parameter, a relation with discharge power and oxide area can also be shown in Figure 26. Generally, an increase in discharge power results in increased oxides for both surface oxides and

recast oxides, due to increased gas, molten metal, vapour, and temperatures. A tapering off trend can be seen for the recast layer depth graph. This is expected as the energy balance would result in energy spreading to other parts of the discharge gap instead of causing oxide generation deeper into the recast layer. Recast layer values have larger errors due to the measurement method used (limited sample area) compared to the more comprehensive surface analysis. It is not possible to take several cross sections of the same hole due to the small size, therefore a single cross-section is not precise and may not be accurate compared to surface SEM and roughness data which produce data over the entire surface and are therefore a necessary compromise. The recast layer is also prone to influences by sample preparation in which oxides can spall off, causing larger data error.

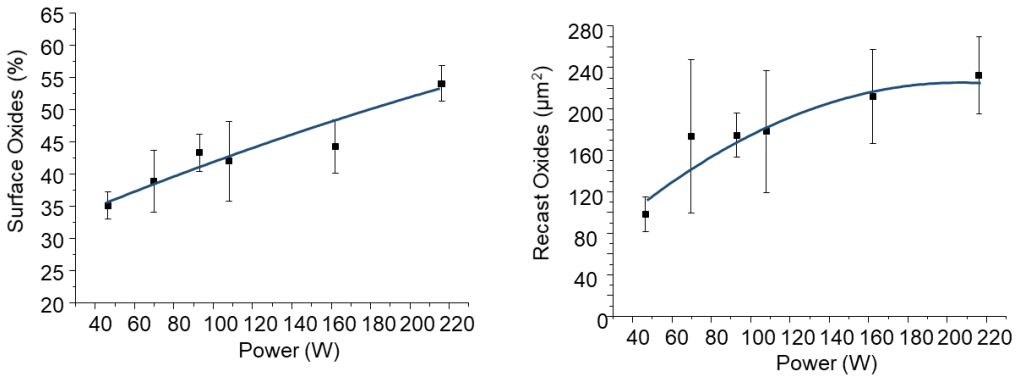

Figure 26. Effect of discharge power on surface and recast oxides. Hole parameters used shown in Table 3. Surface oxide measurements = 193, recast layer oxide measurements = 193. Error is for each power level.

4.3.3 Detailed Parameter experiment

Figure 27 shows the results of the detailed parameter experiment on surface oxides. It was shown that on-time, shown in Figure 27c, has the largest influence on surface oxides, from 27 % at 5 µs to 55 % at 99 µs. A larger increase is seen from on-times from 5 to 40 µs, which then tapers off towards 99 µs, which may be due to reduced oxygen generated for oxidation (gas bubble expansion and limited water for oxygen generation). Current is shown to have a linear increase in oxide area due to increase energy. Off-time shows a sharp decrease in oxides from 5 µs to 40 µs, which then tapers off towards 99 µs, similarly to on-time. This can be explained by a reduction of temperature, molten material for oxidation, and available gases. Pressure is seen to not have a significant effect on oxide area, although a very slight increase which may be due to increase water introducing more oxygen.

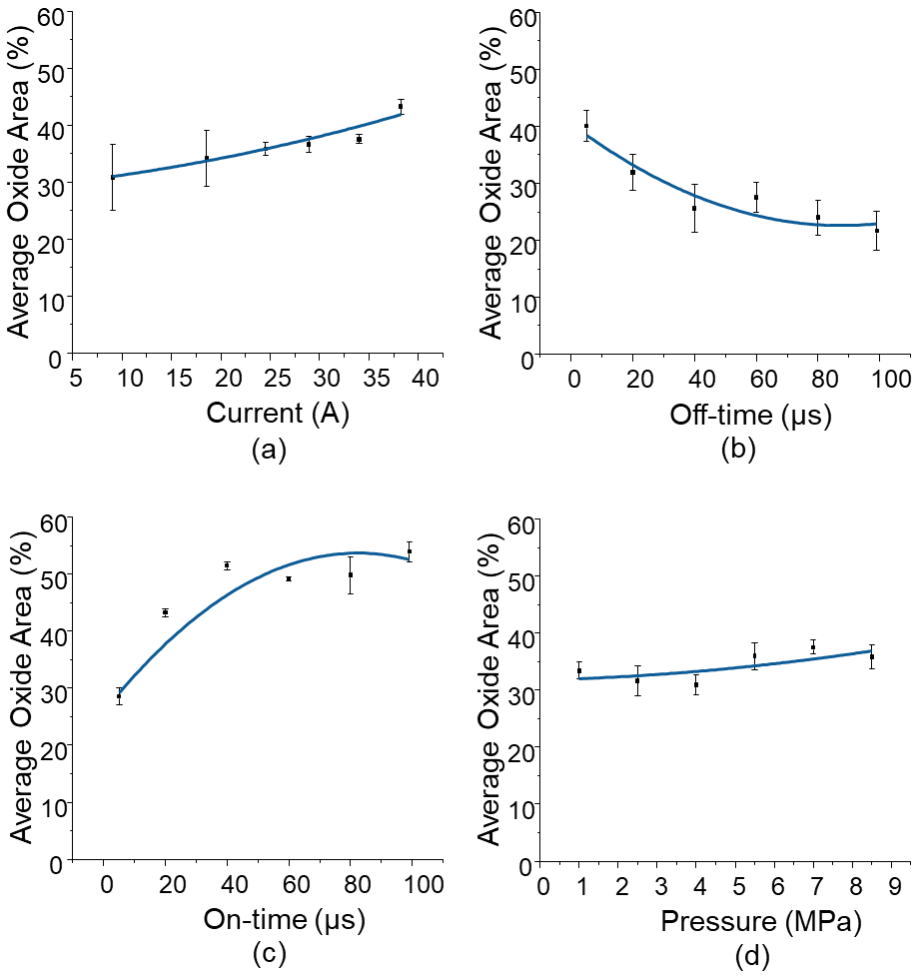

Figure 27. Showing the effect on hole surface oxide area. (a) Influence of current, (b) influence of off-time, (c) influence of on-time, and (d) influence of flushing pressure.

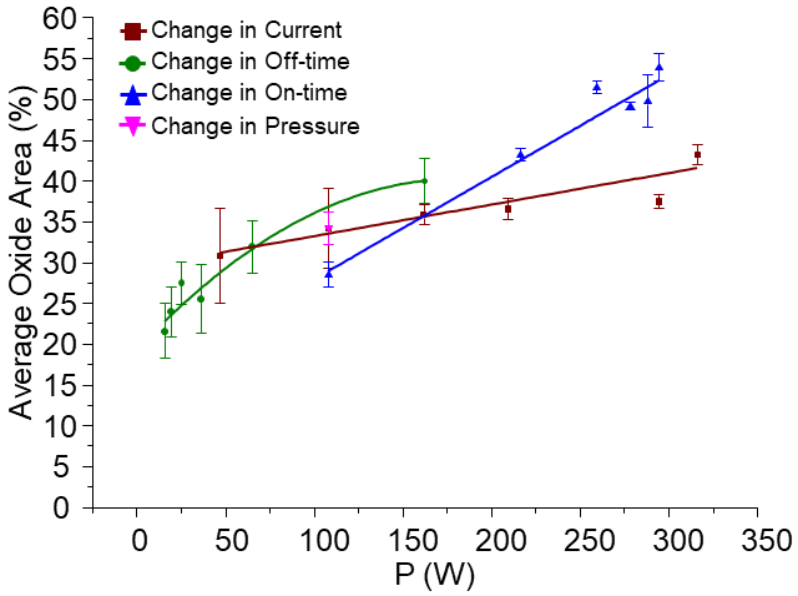

Figure 28. Influence of average power of all runs on average oxide area. n = 72 runs, oxide measurements = 165.

Figure 28 shows a plot correlating the average power for all experimental runs to surface oxide area. Power was used in this case to include the effects of the off-time in each parameter set, as the total energy in the system changes with off-times. The results are similar to the initial main effects results, in that an increase in discharge power generally increases the average surface oxides. The change in oxides is high for on-time, however current produces little change in oxides over a large power range, and produces less oxides at similar powers.

Figure 29 shows that current is the main factor that increases the MRR, followed by on-time, due to the increase in energy for material removal. Current shows a linear increase in MRR, while on-time tapers off due to decreasing energy density. Off-time shows an exponential decrease in MRR due to less power, while pressure shows a slight increase in MRR from 1 to 4

MPa with no change from 4 to 8.5 MPa, explained by improved flushing and gap conditions.

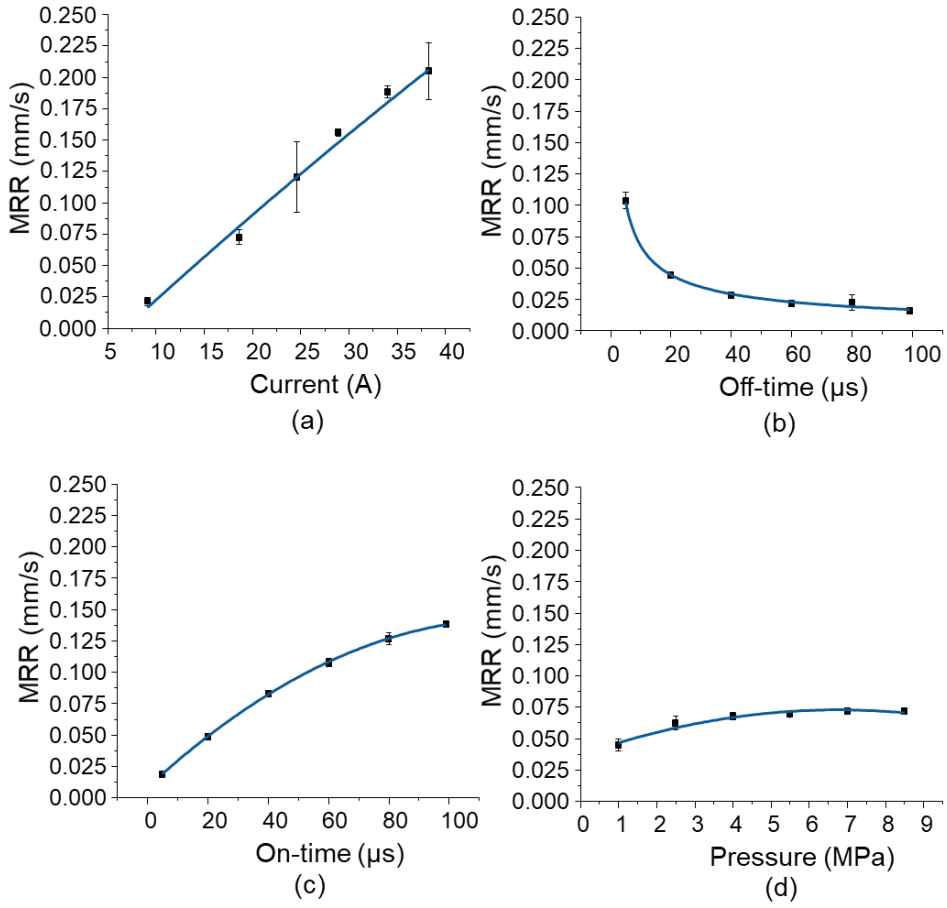

Figure 29. Showing the effect on MRR. (a) Influence of current, (b) influence of off-time, (c) influence of on-time, and (d) influence of flushing pressure. 3 repeats per parameter.

4.3.4 Oxidation Gas Analysis

Gas was collected for the holes machined in Chapter 4 for all experimental runs. It was shown that current increases gas rate linearly and with the highest magnitude compared to other parameters due to increased energy for water splitting. Gas evolution per mm however begins to decrease with increased current. Off-time has an exponential decrease in gas rate with increased off-time due to decreased power, while the change in gas evolution per mm shows

a linear decrease. An increase in on-time shows an increase in gas rate, with a decreasing trend with higher on-times due to saturation of the gap with gases and limited water supply. Gas evolution per mm increases but tapers off to a constant. Pressure shows a very slight increase in gas rate and a slight change in gas evolution per mm.

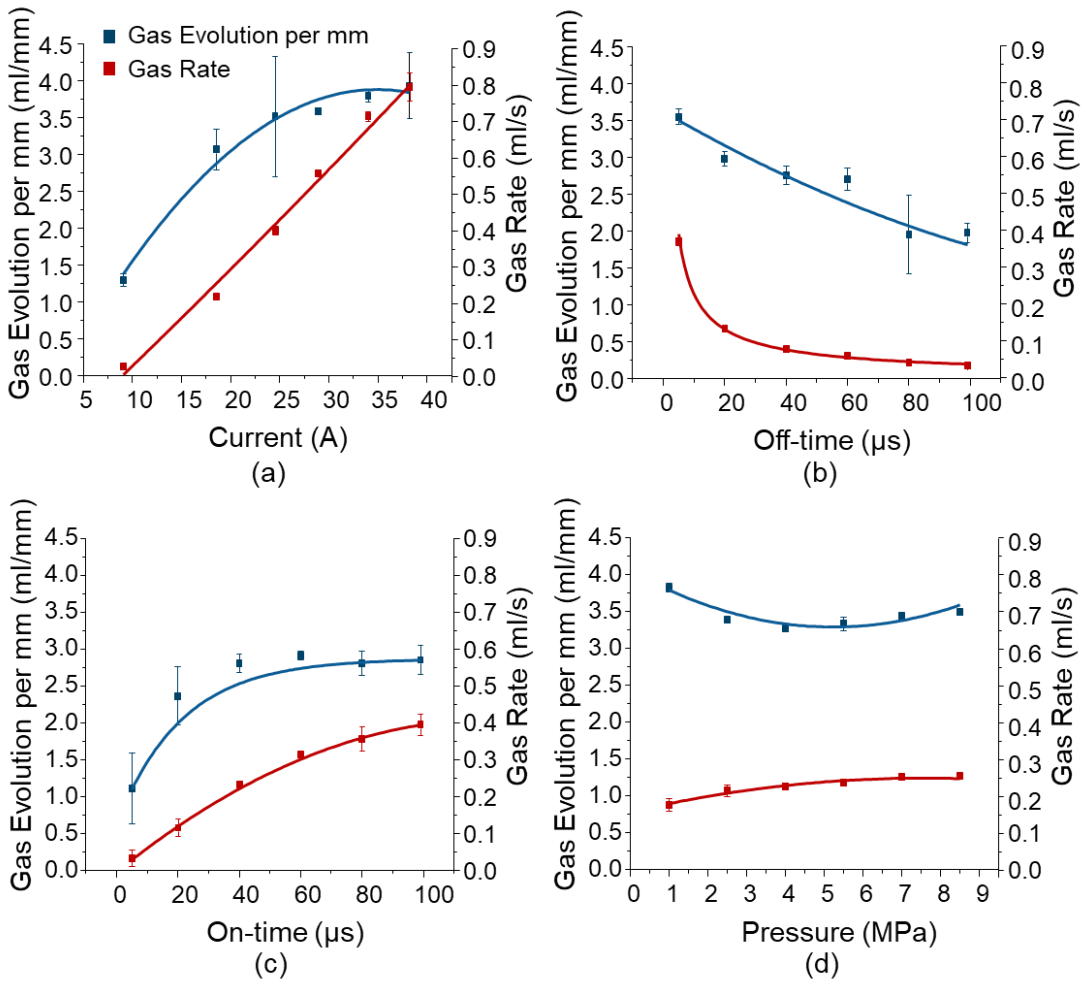

Figure 30. Change in gas evolution per mm hole depth, and change in gas rate, with changes in parameters. (a) Influence of current, (b) influence of off-time, (c) influence of on-time, (d) influence of pressure. 3 repeats per parameter.

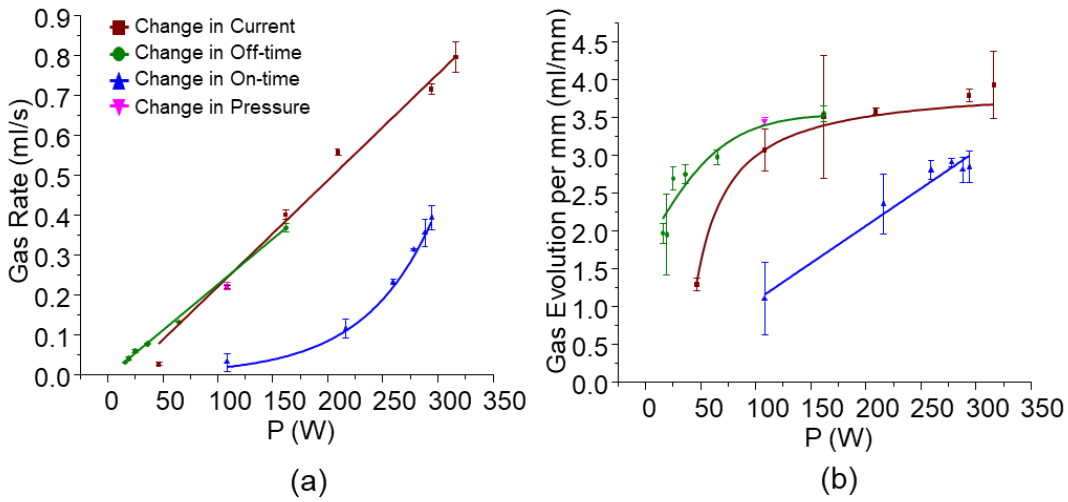

Figure 31. Showing the effect of power on gas rate and gas evolution per mm, for each parameter set. 3 repeats per parameter.

Figure 31 shows that, generally, an increase in power increases the gas rate and gas evolution per mm. Figure 31a shows that all parameters have large increases in gas rate with an increase in power. All show very similar trends, except for on-time which generates less gas at each power value compared to the other parameters, which will be explained further in Chapter 4.4.1 and 4.4.2. Figure 31b shows that off-time and current have a decreasing trend of gas evolution per mm with power. Compared to on-time they generate more gas per mm. On-time also shows a linear trend.

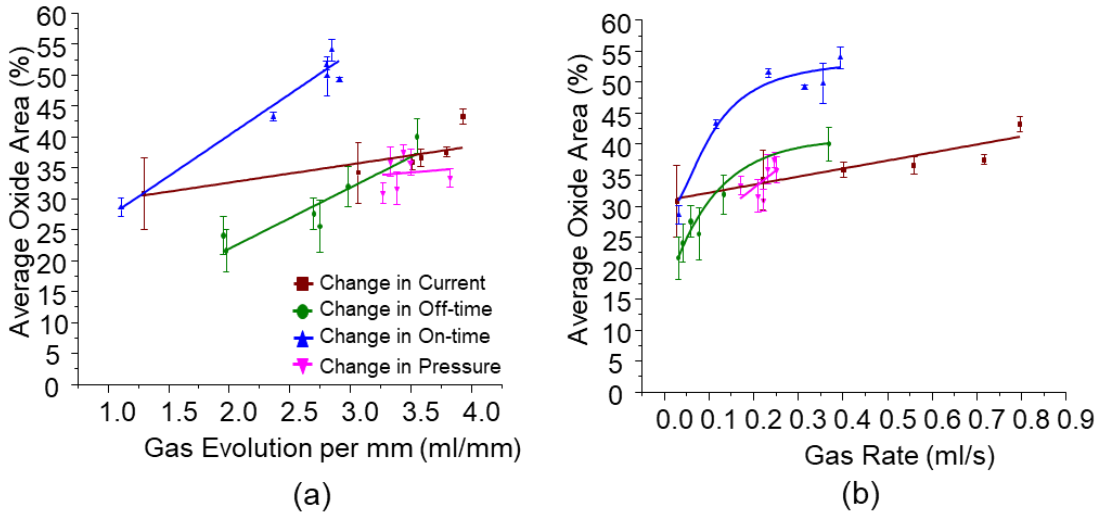

Figure 32. Relation of gas rate and evolution with average oxide area for changes in each parameter set. 3 repeats per parameter.

By relating the gas rate and gas evolution with oxide area the influence of gases on oxide generation can be understood better, as shown in Figure 32. This figure, which relates gases to oxide areas, was used to show the link between Figure 30 and Figure 27 in an easier to understand visual way. Generally, an increase in gas is shown to relate to an increase in oxide area. On-time is shown to result in more oxide area at lower gas rates and gas evolutions per mm compared to other parameters, which will be explained further in Chapter 4.4.1 and 4.4.2. Current is shown to have a smaller change in oxide levels with changes in gas rate and evolution.

4.3.5 Constant energy Experiment

To understand the difference with a high and low impulse parameter, two same power parameter sets were used to see the effect on oxides. With this method the effect of parameters on oxides without interference of pulse power can be obtained. Figure 33 shows that, at the near same power levels, the

parameter with the high on-time and low current had considerably more oxides on the surface.

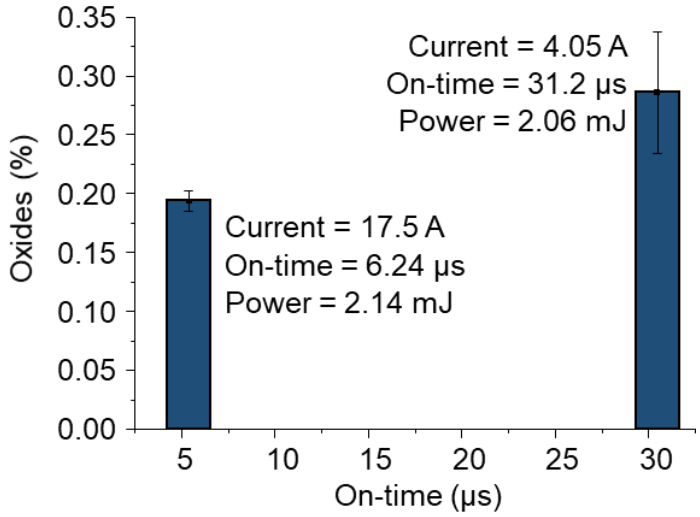

Figure 33. Showing the effect of parameters at constant energies on oxide levels.

4.4 Discussion

4.4.1 Oxidation Mechanisms

The mechanisms of oxide formation can be understood by analysing the BS-SEM images produced for all holes. For all holes, oxides have been concentrated in regions surrounding discharge craters, as shown in Figure 34. From this, we can infer that expansion of the crater, plasma, and bubble have caused this concentration by observation of the geometry, which shows radial concentrations around craters. It can be implied that oxide regions are produced in the molten state. In some instances, lines, which expand out radially from crater centres, can be observed, likely caused by molten metal flow (radially outwards) and are visible due to slightly different structure or composition. In Figure 34 concentration of oxides are mixed with debris. This

also solidifies the understanding that oxides are produced in a molten state, as all oxide regions have mixtures with non-oxide globular solidified debris. Therefore, movement of molten material which has rapidly oxidised and resolidified on the edge of the crater can be assumed the main cause of oxides in the recast layer. The influence on the magnitude of this piling of oxides on the edges is linked to the EDM parameters and will be explored in more detail.

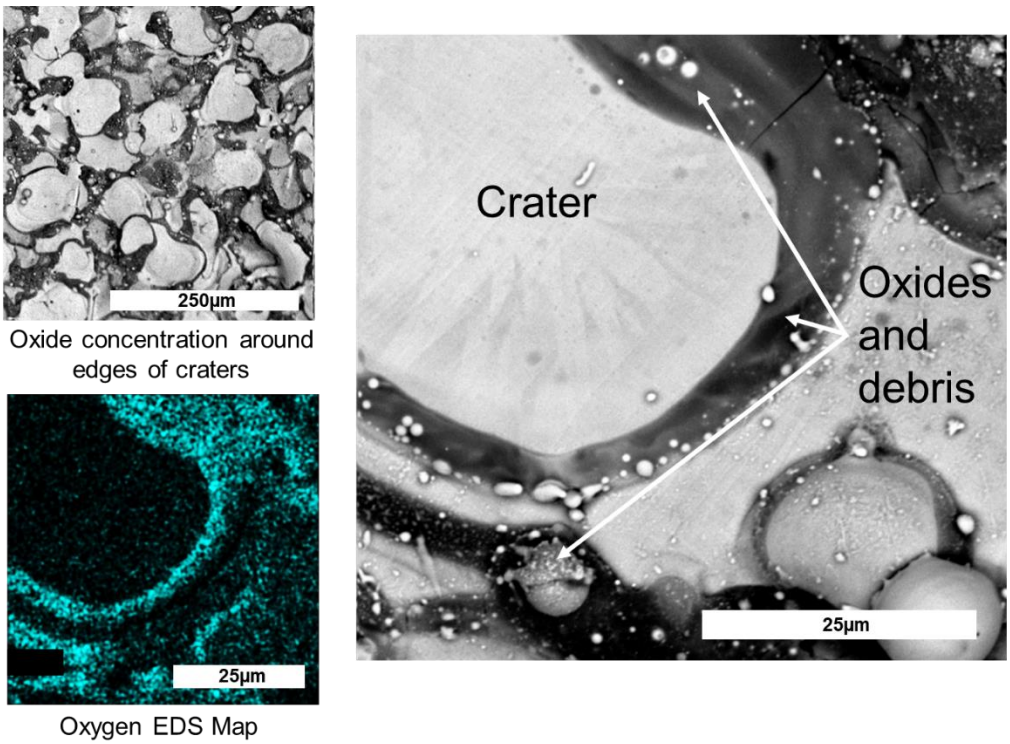

Figure 34. Showing oxide and debris surrounding craters. Darker regions signify oxides. Craters show flow lines. Oxide regions show debris accumulation.

Figure 35 shows a schematic of the proposed oxidation mechanism in EDM with DI. At t = 0 µs the surface of the component during EDM is covered with the usual recast surface features. When a discharge occurs between t = 0 µs and t = 5 µs the temperature rapidly rises due to the ionised plasma channel. A high temperature gas bubble surrounds the plasma consisting of hydrogen and oxygen from thermal decomposition as well as metal vapour. The figure

also shows remnant bubbles from previous discharges in the spark gap for illustration. The high temperature causes melting and vaporisation of the metal. Due to the bubble expansion, heat supplied from the plasma, metal vapour, and liquid outside, the bubble is under high pressure and there is a force applied on the molten pool causing molten pool movement and pushing outwards, and possibly ejection.

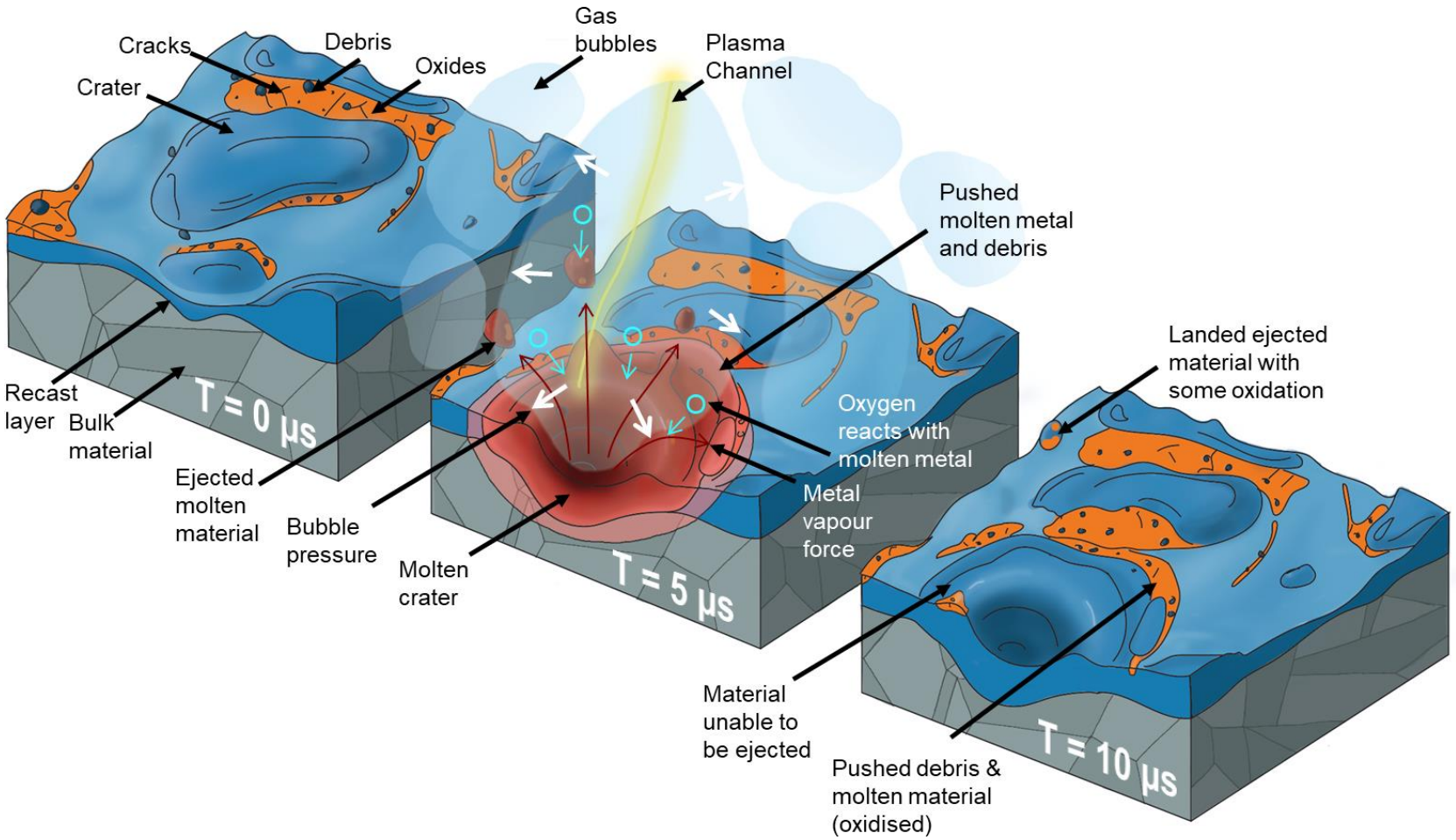

Figure 35. Proposed mechanisms of oxidation. At T = 0 µs, EDM surface during machining consisting of recast layer features. At T = 5 µs electrical discharge, at T = 10 µs resulting surface.

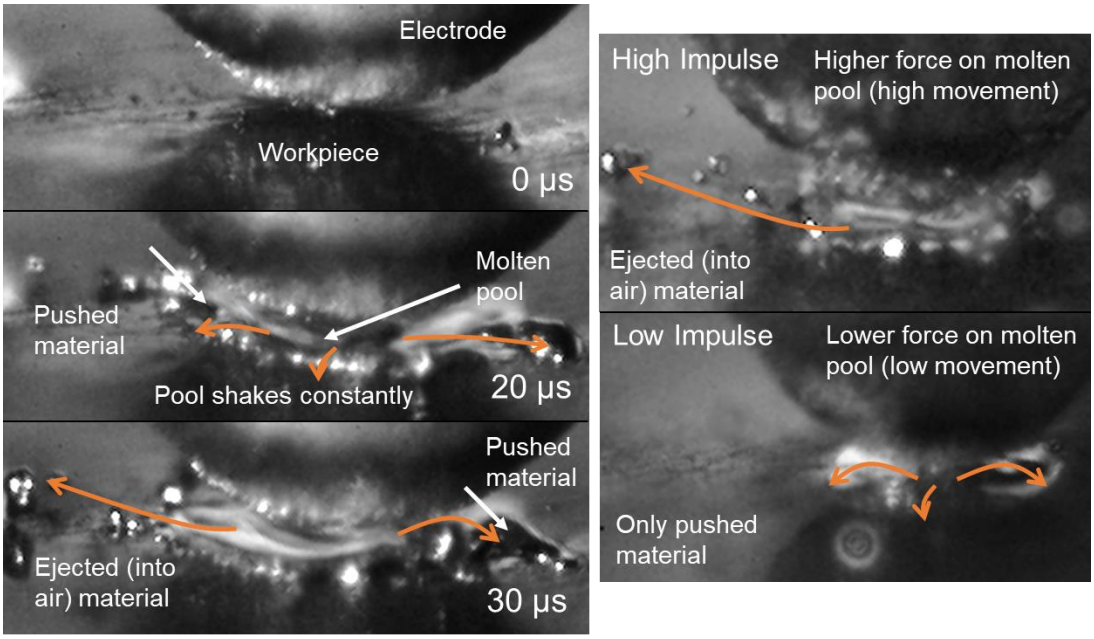

Figure 36. (a) Showing high-speed images at 1,000,000 FPS, showing the molten pool, material pushing, and material ejection. Two different types of molten metal ejection. High impulse: low on-time and high current. Low impulse: high on-time and low current.

To show this visually, high-speed images of single discharges were used. Figure 36a shows molten pool behaviour, and Figure 36b shows differences in pool ejection due to impulse forces. The impulse force is the force acting on the molten pool due to the changing pressure gradients, in this work the term impulse force is instead used as it is commonly referred to as this in the literature for EDM, Figure 38 shows removal via vapour explosions and Figure 37 shows the relation to the plasma channel.

In Figure 36a, between 0 and 20 µs electrical breakdown has occurred, after which at 20 µs molten metal is being pushed outwards from the centre of the molten pool crater. At 30 µs some of the molten metal has been pushed out from the molten pool, while some has only been pushed towards the edge

which will then solidify in its position. This movement is due to the vaporisation forces and due to the ionised plasma channel, which is shown in Figure 37a where light from the plasma is seen in the direction where material ejection is observed (video taken without a laser filter). In water this force would be further increased due to forces generated through decomposition and expansion of gases produced from H_2O. The pressure (as well heat flux) at the centre of the plasma is highest and reduces as distance from the plasma centre increases, with an increase in current increasing the spread of heat flux and increasing pressure [134]. Therefore, vaporisation and melting is concentrated at the region where the plasma is on the molten crater. The plasma is also known to move around the crater [135], with its range of movement (and diameter) increasing with time [136]. This can explain the effect the plasma has on molten metal movement and ejection. Figure 36b shows two types of molten metal ejection. A higher impulse force on the molten crater can cause increased molten metal ejection, while no molten metal ejection can be caused by low impulse force on the molten crater. The impulse force is affected by the amount of time the plasma channel is active and expanding, and how much energy is put into the plasma channel. This is essentially controlled by on-time and current. A low on-time and high current results in a high impulse force, while a high on-time and low current results in a low force. The relation of power will be discussion in Section 4.4.2.

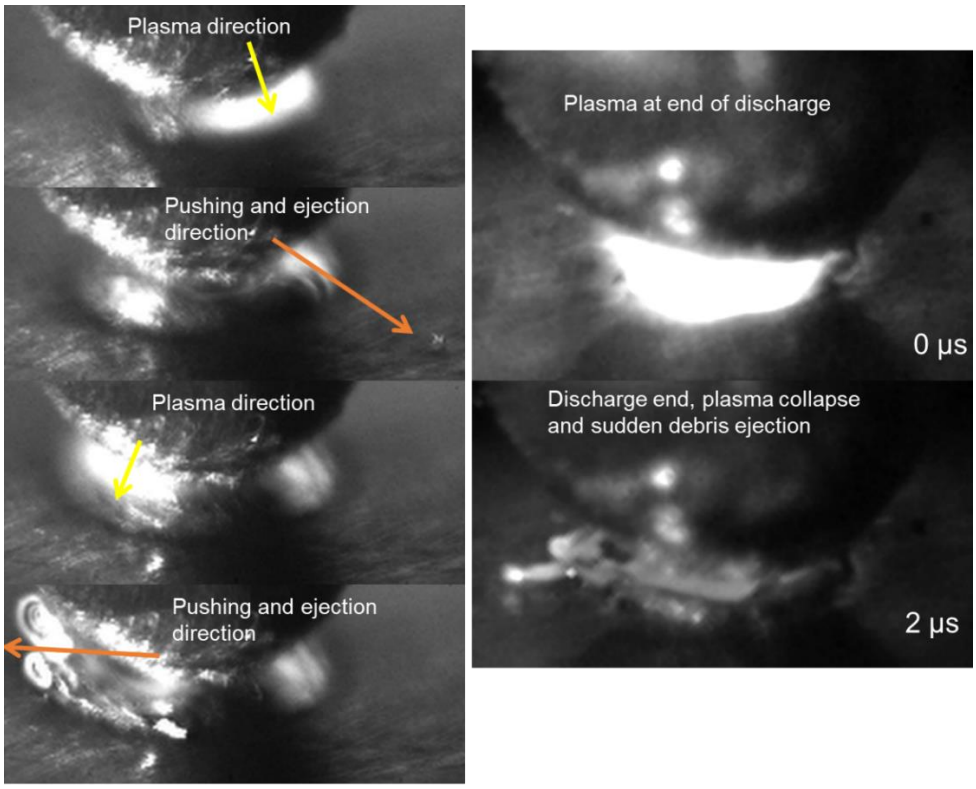

Figure 37. (a) Influence of plasma direction on molten debris ejection direction, (b) plasma collapse force on molten debris ejection.

This was confirmed by Zhang et al. [42] who suggested that a decrease in on-time increases bubble pressure (boundary between bubble and liquid) and plasma pressure, which also increases the impulse force on the molten pool due to the expansion and contraction of the bubble, thus ejecting more molten metal (the impulse force was higher in liquids compared to gases). This was also confirmed by M. Zhang et.al [45]. Lower pressures due to higher on-times thus cause flatter craters (molten metal getting pushed rather than ejecting), while higher on-times cause craters with rims and deeper depressions. Maradia et al. [137] also suggested than an increase in bubble pressure (higher pressure gradient on the gas bubble boundary) results in higher molten metal ejection, while lower pressure gradients are seen at the gas bubble

boundary for longer on-times resulting in reduced molten metal ejection. The plasma electron density is also highest at the beginning of the discharge (highest pressure) and is 5 times lower near the end, which is the case with longer on-times. This was also shown by Kanemaru et al. [85] who indicated the pressure also decreases with time (and increased bubble radius), along with the electron density of the discharge.

Thus, it can be inferred that parameters which cause molten pools to only push towards the edge will result in concentrations of oxides on edges of craters which solidify as either oxides, resolidified bulk material, or a mixture including any accumulated debris. With parameters with high material removal, the oxidised material will be removed from the spark gap and flushed away, resulting in either lower oxides, or redepositing of oxides further away from the current discharge crater.

Molten material removal from the molten crater can also be explained by vapour explosions within the melt pool, as shown in Figure 38. Figure 38a shows a vapour bubble forming at 0 µs, which expands at 2 µs, and shows debris removal at 8 µs. Due to the rapid process, only a few frames can be captured therefore the still images shown in Figure 38 are difficult to interpret without viewing a video of the process. Annotations are used to expedite understanding. This addition in molten metal removal is influenced by higher currents and is likely to only occur at the start of discharges, so will be more pronounced for shorter on-times. Molten metal explosions occur due to plasma heating of the molten metal causing some internal vaporistion, which then overcomes the atomic binding force leading to expansion and molten metal ejection [29]. Figure 38b shows molten metal which is close to the electrode

due to molten pool movement, which then near instantly explodes between 0 and 1 µs. It can be infered that due to the closing gap between the molten metal and electrode the plasma has moved to the smallest gap, resulting in sudden heating causing a vaporisation explosion resulting in molten debris removal. This is shown by observing direction of plasma and resulting direction of debris removal in Figure 37a. The force when the plasma collapses also results in sudden material ejection shown in Figure 37b, which also depends on current and on-time.

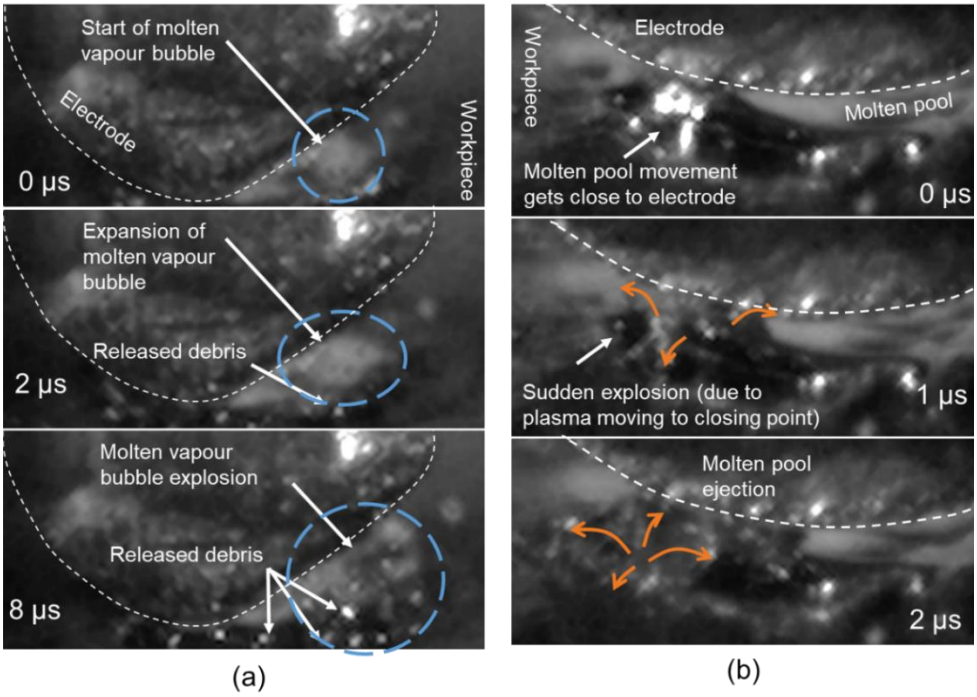

Figure 38. (a) Vapour explosions in molten metal. (b) Molten metal explosion due to plasma movement

Referring back to Figure 35 at T = 5 µs, after the plasma has produced a molten crater and molten crater movement and ejection has begun the high temperature gas mixture and a small portion of the molten metal rapidly react in the oxidation reaction around the crater, where the molten metal has been

pushed out. Some oxidation on the crater itself will also occur if molten material cannot be sufficiently ejected, while some oxidation of ejected molten metal may occur too. During the on-time for the discharges shown in Figure 36 the molten pool is seen to vigorously shake due to the forces applied to it. This agitation of the molten pool may also increase oxidation as it increases the exposure to the high temperature gas and encourages molten metal and gas mixing. The rapid movement of the plasma to the point of lowest resistance also causes molten pool movement. As shown in Figure 39, in some areas of the machined holes we can also observe spheres at the edges of craters near the oxide regions which supports the gas mixing theory. Oxygen is also likely to diffuse into the metal and precipitate oxides.

This can also be explained by a mechanisms first suggested by De Luca for laser powder melting [92], which explains that molten oxides separate from the molten pool and disperse throughout based on the strong Marangoni convention driven by the surface tension gradients. Oxides then accumulate towards the surface of the melt pool at the edges due to Marangoni forces due to the lower density of oxides and reintroduction into the pool is prevented by bad wettability. The time scale of this will be larger than that of the discharge on-time, as the movement of the pool continues after the discharge has moved location. The solidification front is also likely to push oxides into the remaining molten pool, pushing towards the surface and edges.

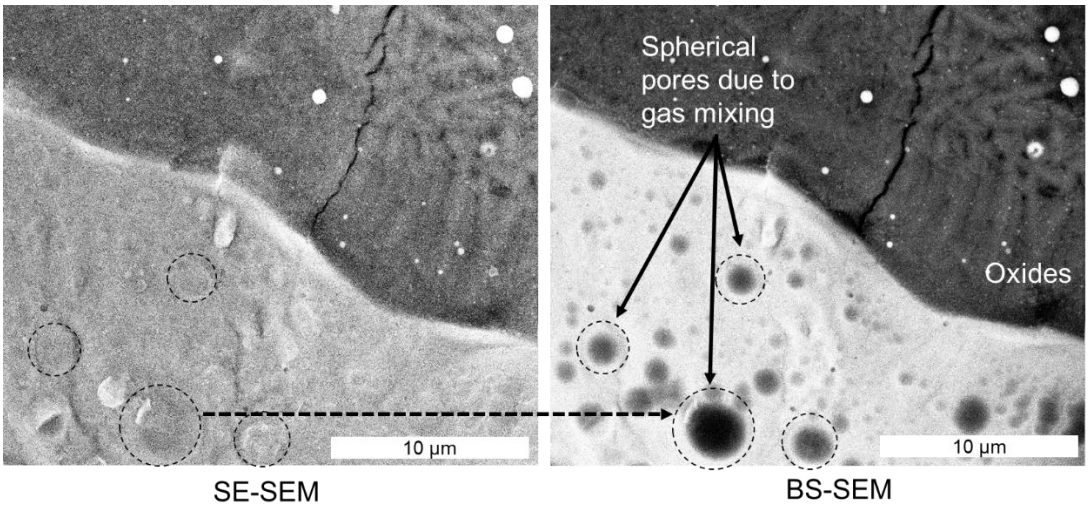

Figure 39. Showing secondary electron and back scattered electron SEM images of the edge of an example crater near an oxide region. Spherical pores are shown which indicate gas mixing with molten material.

The bubbles produced will also likely concentrate molten debris and solidified debris at the bubble interfaces, causing the deposits to concentrate in circular geometries around craters (where the expanding bubble originates). This then causes a concentration of the oxidised material around the molten crater.

Between T = 0 µs and 5 µs, oxidation rate in the melt pool is controlled by the reaction of the molten metal gas interface, therefore it should follow the linear rate law and be proportional to time, allowing rapid oxidation [76-78]. This happens because the oxygen can easily pass through molten metals (compared to solidified metals) and can rapidly arrive at the metal oxide interface. Due to the rapid movement of the molten metal, more bare molten metal is exposed for oxidation, while the reacted sections are either mixed into the molten metal or pushed to the side. Once this oxide thickens or begins to solidify, oxidation is controlled via diffusion through the oxide layer through the parabolic law (decreases with time). This is the case when the oxide is well

adhered to the surface and is compact. Due to sparking and flushing any oxide layers that have begun to spall off or detach from the surface will not exhibit diffusion controlled oxidation. For areas surrounding the molten crater, diffusion controlled oxidation is likely to occur due to the high gap temperature and abundance of oxygen in the gap. These oxide regions will however be thin and compact and are likely to not contribute to the total oxide area due to the significantly slower rate of oxidation compared to molten metal.

Referring back to Figure 35, at T = 10 µs the heat due to the plasma has melted part of the crater shown at T = 0 µs and pushed surface debris and oxides causing further accumulation. Between T = 5 µs and 10 µs, the molten metal and oxide has solidified.

4.4.2 Influence of parameters

It was shown that high current and on-time (Figure 23, Figure 27), and discharge power (Figure 26, Figure 28) increases oxides, while high off-time decreases oxides (Figure 23, Figure 27).

Discharge energy and discharge/crater formation characteristics, as well as cooling and flushing of the spark gap were considered the main possible influencers of oxide formation in the recast layer. Figure 40 shows gap conditions relative to parameters used, and is used to convey the general effect of energy on the discharge gap and oxidation. In Figure 40a, a spark occurs which removes material and produces a gas bubble which grows during the spark on-time. When the current flow stops the gas bubble begins to implode, releasing the gas into the spark gap along with the molten debris, as shown in Figure 40b.

From previous results it was shown that discharge power increased oxides. With an increased energy more gas is produced by decomposition of the dielectric, as well as more molten metal and vapour being produced. This gas then fills most of the spark gap, increasing available oxygen for oxidation. The increased energy also results in increased gap, metal surface, and molten metal temperatures resulting in an increase in the rate of the oxidation reaction. Conversely, a low energy parameter results in decreased gases, debris, and temperature as shown in Figure 40, while a high off-time and flushing parameter results in decreased gases and debris due to removal from the discharge gap.

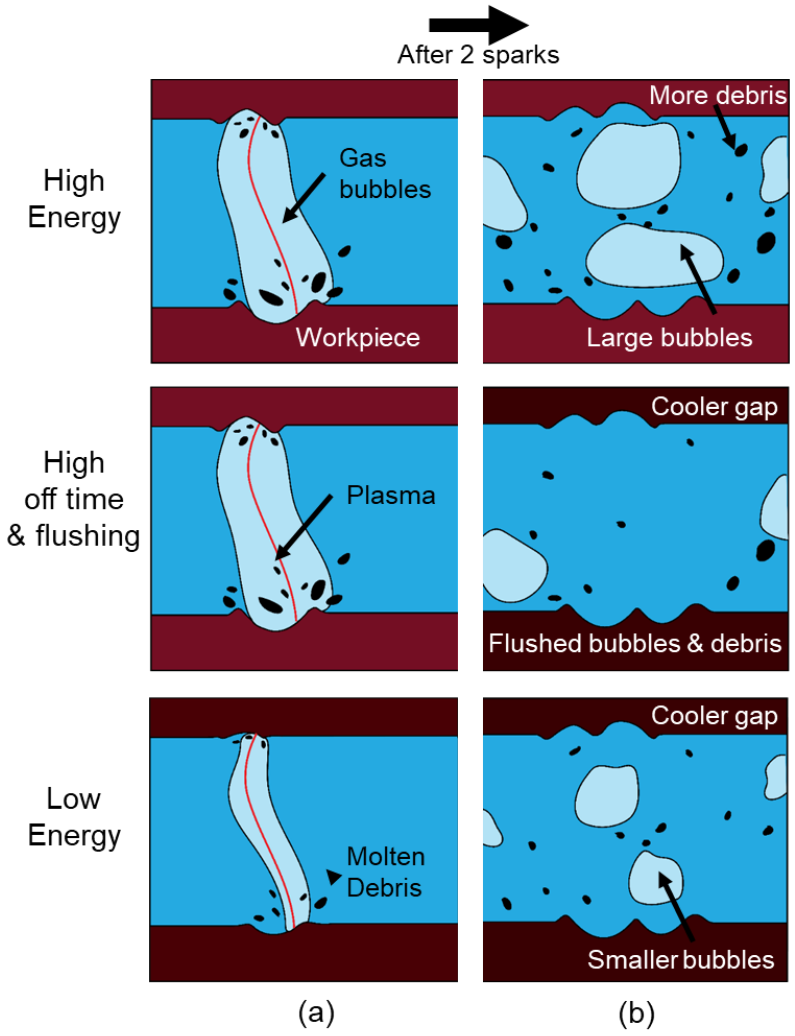

Figure 40. Influence of parameters on gap conditions. High energy, high off-time and dielectric flushing, and low energy. (a) shows discharge, while (b) shows resultant gap conditions after 2 consecutive sparks.

The increased energy supplied, while it does increase oxides, also likely results in higher molten metal ejection from the discharge site. As discussed previously, this higher energy parameter could lead to discharges with increased impulse forces. However, this depends heavily on parameter combinations as discussed below.

Higher currents result in increased gases (Figure 30) and gas bubble pressure (from increased decomposed H_2O and metal vapours), which results

in the gas bubble collapsing with more force thus ejected more material. It also increases the plasma movement velocity [136]. This can in turn result in molten material ejection from the discharge site (reduced build up around crater edges) and thus reduced oxides. This may explain why even though current increases discharge energy the most compared to other parameters, the slope in Figure 28 is the smallest, showing than an increase in current, while it increases energy significantly, only marginally increases oxide area. This is explained due to an increase in the discharge impulse force and removal mechanisms as discussed previously, which is also shown by observing the change in oxide topography with depth from the holes machined in Chapter 4.2.2, shown in Figure 41. For current generally oxides are seen to increase with depth, as compared to the other parameters. This can be attributed to the strength of discharges removing surface oxides, both oxides which were already on the surface from previous discharges, and newly formed oxides. Secondary discharges also play a role in slowly removing oxides from the surface, which would be further enhanced by higher currents and forces.

On-time, similarly to current, has high average discharge energy as shown in Figure 28, however oxides are considerably more at longer on-times at the same energy, while the low on-times show low oxides. On-time was also shown to have the largest difference in oxide levels between the lowest and highest on-time. This can be partly explained by lower on-time discharges producing high impulse forces and bubble pressures, resulting in molten debris ejection, while the longer on-times produce lower impulse forces. On-time also increases exposure time of the molten pool to gases, as well increasing the amount of gases surrounding the discharge site (which levels

off due to decreased supply of H_2O in the gap as shown in Figure 30), and increased time for movement and mixing of the molten pool. The heat generated has more time to be lost into the gap, increasing the gap temperature. Due to the increased plasma size with time [138], the heat flux is lower due to lower current density at the discharge spot, resulting in larger craters with more heat dissipated into the gap [83]. Vapour pressure is also reduced for longer on-times due to reduced plasma and liquid interface temperature [28]. Short on-times also result in more material removal due to this increased energy efficiency due to the higher energy density. In addition to this, when on-time is increased (at a constant off-time) the spark gap has less time to remove gases, debris, and reduce the gap temperature, therefore compounding the influence of the increased on-time. In this sense, a longer on-time with short off-times reduces gap flushing and cooling. Therefore, we can see large build-up of oxides around craters as shown in Figure 41. With depth there is also little change due to the low impulse force of high on-time discharges.

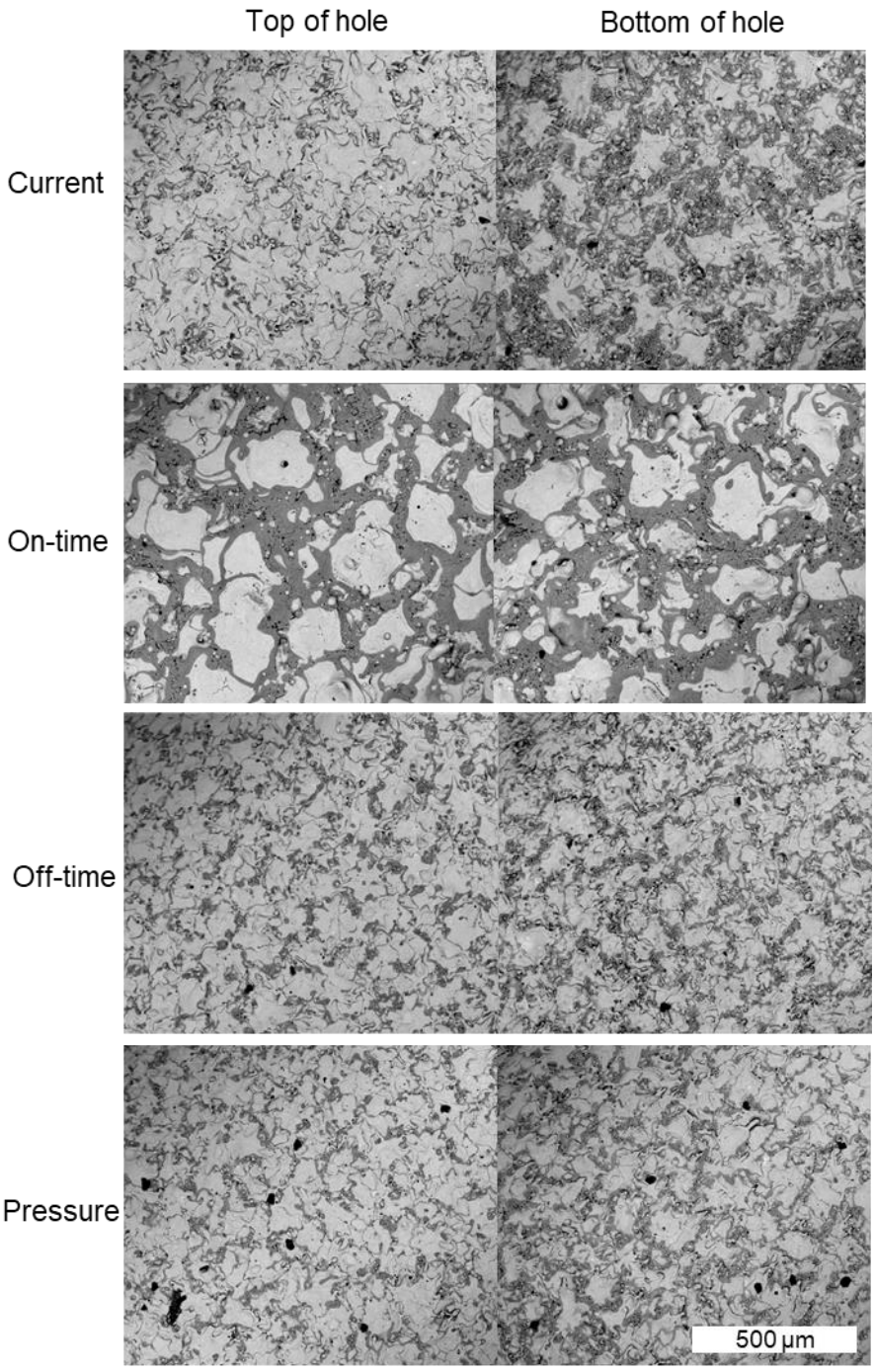

Figure 41. Showing example changes in surface topography with depth for parameters. Current shows a large change in oxide geometry with depth due to differences in pulse parameters. On-time, off-time, and pressure have a small change in comparison.

By relating the power to the gas rate an interesting result can be observed which confirms the above discussion. At a set discharge power, as shown in Figure 31, on-time was shown to produce the least amount of gas, while the

other parameters behaved similarly to each other. Once we compare this to Figure 32 we can relate this decreased gas production at higher energies with an increased oxide percentage. This means that at higher on-times, and thus high discharge energy's, some of the energy was used in production of oxides instead of production of gas. This is because there is a decreased amount of H_2O in the gap due to gas saturation in the local gap, which prevents further gas production. It may also be the case that instead of producing gas (which sometimes occurs when a surface is covered by oxides [105]), further oxides are formed. This confirms that the increased exposure time of molten metal to the increased on-times resulted directly in oxidation of the molten material instead of gas generation. This may be because at higher on-times the spark gap is full of gases due to the longer plasma duration (which keeps the gas bubble expanding). The gases within the spark gap and the energy supplied thus have an increased opportunity to oxidise the molten material. The energy also has more chance to be lost into the spark gap, such as for increasing gap temperature and oxidation rate, and heating and vaporisation of the molten metal (which also increases mixing).

To confirm effects of parameters on impulse force, a constant energy experiment was conducted, with results shown in Figure 33. The increase in oxide levels at constant energy parameters can be attributed to the method of molten material removal. The difference between high and low impulse, which was discussed previously, is the main factor in this. Even though the current is higher, the oxide levels are lower due to this change in impulse force. This may explain why some parameter combinations do not show expected levels

of change in surface oxides, as their energies or difference in metal ejection depend on the combination of current and on-time. Figure 42 shows the difference in crater morphology. The high on-time and low current parameter shows shallow craters which are pushed and spread out with oxides concentrated heavily around craters. The low on-time high current parameter, however, shows deeper craters with remnants of ejected material in the form of blobs surrounding the edges. These findings confirm previous discussion concerning effect of crater impulse force.

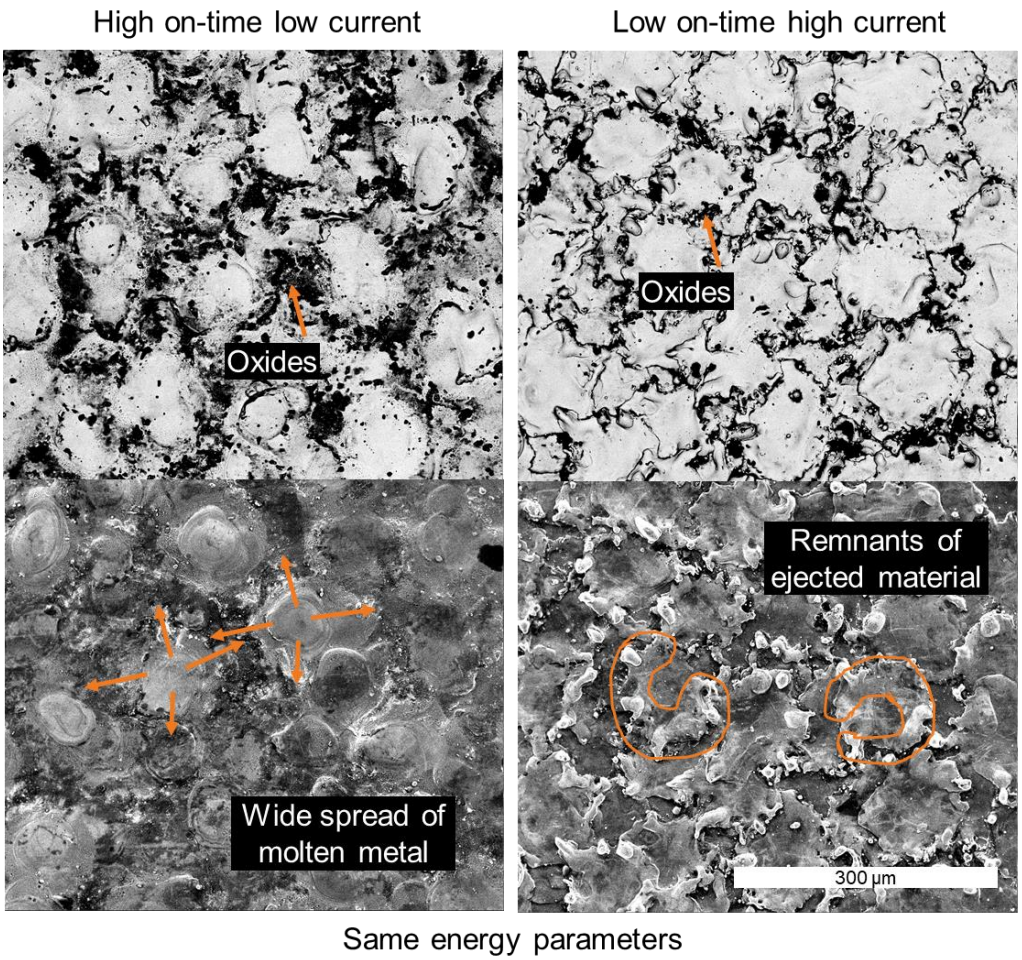

Figure 42. Shows surfaces of same energy parameters which differ in crater geometry. Highlighted areas show differences in crater morphology.

For improved cooling and flushing conditions, spark off-time was increased as well as the flushing pressure. This results in the gas bubbles being flushed away from the spark gap reducing the amount of available gases at any instant for oxidation, as well decreasing gases due to less sparking (longer times between sparks) (Figure 30). The temperature of the spark gap is also likely to decrease, reducing H_2O spitting and oxidation through decreased reaction temperatures. Molten debris will also be removed and cooled faster. Thus, the molten debris will have less exposure time to the high temperature spark gap and gasses, reducing the total oxidised material. This was confirmed by the reduced oxides with an increase in off-time, however pressure did not show a clear result. Although flushing pressure was shown to have an effect on oxides in Chapter 4.2.2, in Chapter 4.2.3 there was no significant trend. This may be explained by the difference in hole size between the initial main effects experiment and detailed parameter experiment. The smaller 0.3 mm holes showed decreased oxides for increased pressure, while the larger 1.9 mm hole showed no change. The increased flushing pressure may have had more of an influence due to the smaller surface area which promotes higher temperatures and reduces flushing ability. The flushing pressure may also have a limited influence on the discharge scale of the process, at least for the pressures tested. For short on-times the effect of increased pressure may be small, therefore not affecting molten metal oxide formation.

A balance between oxide surface area and outputs relevant to industry must be made. An increase in current was shown to increase the MRR, resulting in faster machining, however resulted in more oxides, electrode wear, and surface roughness. The increase in oxides can also further increase MRR due

to the heat generated through the reaction and due to oxides having a lower melting temperature than the bulk [87]. An increased on-time was shown to have an increase in MRR, however resulted in an increase in oxide area and slight increase in roughness. An increase in off-time was shown to decrease the MRR while decreasing the oxide area, with no effect on roughness. Pressure was shown to have an increase in MRR, a decrease in oxide area (for the 0.3 mm holes), and a decrease in roughness. Therefore, a surface with the least oxides must have a low current, low on-time, high off-time, and increased flushing. This would result in a hole with the lowest roughness and best surface finish, with the least electrode wear, however the machining time would be considerably high. Therefore, acceptable parameters must be chosen relative to the requirements of the machined part and intended use.

4.5 Conclusion

It was shown that current, on-time and discharge power increase oxides, while off-time and pressure decrease oxides. The importance of discharge crater formation characteristics was also linked to oxide formation.

Discharge power increases oxides by increasing gases, molten metal, and temperatures, while a high off-time and flushing removes gases and debris and reduces temperatures, reducing oxides. However the combination of on-time and current is more important than solely discharge power. A change in current was shown to increase oxides due to increased gas production, and was linked to an increase in molten metal, metal vapour, and gap temperature. On-time was similarly shown to increase oxides due to the same reasons, in addition to molten metal exposure time. However longer on-times produced more oxides at similar power levels. This was explained by the decrease in discharge impulse force of longer on-times, which reduces material ejection, increases molten metal exposure to oxygen, and increases gap temperatures. This results in oxide and debris concentration around craters due to forces on the molten pool. The decreased gas production also implies a higher energy fraction into oxide formation. Higher currents however increase metal ejection and removal of oxides and spall off existing oxides, resulting in marginal increases in oxides at similar power levels. Even at the same energy, a low on-time high current parameter exhibits lower oxides than a high on-time low current parameter. An increase in off-time and flushing pressure results in decreased oxides due to decreased gases, and was linked to decreased gap temperatures, improved cooling, and reduced debris. Discharge impulse

forces must be high to ensure molten metal ejection, prevent increased concentration around edges, and longer exposure times to gases and energy.

To achieve a hole with a low amount of oxides, a small on-time and lower discharge energy is needed, as well as increased flushing and off-time. This results in a parameter with high discharge impulse and high gap flushing and cooling. This would result in a hole with decreased oxides as well as surface roughness, decreased recast layer depth and increased surface integrity while also decreasing the electrode wear. However, the machine time would also increase which may be unwanted. A balance is therefore required depending on the usage case using the fundamental understanding of oxide formation as a basis.

5 Electrolytic-Dielectrics: A route to zero recast EDM

5.1 Introduction

In EDM the recast layer is unwanted and removal is highly desired for parts where surface integrity is key. The literature review revealed multi-step methods which removed the recast layer, however at the disadvantage of multiple steps increasing production cost and complexity. Some past attempts at incorporating EDM and chemical machining was made, however the entire recast layer was not removed, there was inability to control the surface, and fundamental understanding of the mechanisms was lacking.

This chapter aims to develop a single-step process to simultaneously machine via EDM and remove the recast layer via ECM. Sodium salts are often used in ECM, with NaCl being the most common non-acidic electrolyte. NaCl will therefore be used to understand the basic mechanisms of the process. Different salts produce different surfaces in ECM; therefore this idea will be used to explore control over the removal of the recast layer in this process. Altered removal mechanisms will be used to understand fundamental mechanisms in this process to enable future control and improvement of the process.

5.2 Methodology and Experimental Process

The electrodes used were 1.9 mm diameter brass , with a multi-hole deionised water channel to ensure no central material remains after machining, at 5 MPa internal pressure. Brass was used due to its improved wear and MRR compared to Cu [125], as it has a higher melting point, which

is factored in its erosion index (a measure of a materials suitability as an electrode) [126]. The workpiece was an Inconel 718 rectangular piece (nominal dimensions 25 mm by 25 mm by 10 mm), which is used in high-temperature aerospace applications due to its resistance to corrosion and good high-temperature properties [128, 129]. The nominal composition of Inconel 718 is listed in Table 4. The theoretical electrochemical equivalent for the alloy, calculated for the upper and lower ranges of the nominal composition as shown in Table 4, was calculated as 0.258 – 0.295 mg/C) according to $\frac{m}{Fz}$, where F is the Faraday constant, m is the atomic mass, and z is the ion valency.

Electrolytic-dielectrics were produced using the deionised water mixed with the selected salts, using a magnetic stirrer until the conductivity reading stabilised and the required levels for experimentation were obtained.

5.2.1 Sodium chloride based electrolytic-dielectric

To show the principles of machining and recast layer using electrolytic-dielectrics, five electrolytic conductivities were used to assess the effect of conductivity and increased electrochemical action on the EDM recast layer. Conductivities of 1, 200, 400, 600, 800, and 1000 µS/cm ± 0.5 µS/cm were used, using NaCl (Fisher Scientific, >98%). These electrolytic conductivities, which are an order of magnitude greater than conventional EDM dielectrics, and an order of magnitude lower than conventional ECM electrolytes, were selected to allow both anodic dissolution and discharges thus enabling both modes of material removal.

Machining was conducted for a fixed time of 60 seconds, with three repeats per conductivity level. Blind holes were machined instead of through holes to increase process understanding through EDM and ECM zone data, as through holes may result in significantly reduced or no EDM zone depending on process method. EDM parameters were fixed during experimentation and were set to 18 A peak current, 5 µs on-time, and 10 µs off-time, which were chosen as they produced good MRR and wear performance with the DI dielectric.

20X objective was used to measure the surface roughness using the Alicona G4 focus variation instrument. BSE and SE microscopy was used to assess the influence of the salt and conductivity on the recast surface. The portion of the hole surfaces analysed was measured from the same distance (0.3 mm) from the top of each hole, in the electrochemical zone.

The change in roughness with depth was obtained by separating the lateral profiles along the depth of each hole and calculating Ra. The resulting change in Ra with depth curve was smoothed by a moving mean method with a smoothing factor of 1.5, processed in Matlab, to ease figure understanding. The Rz parameter was also calculated, which is the mean of the sum of the peaks and valleys for five sampling steps for each sample profile. This parameter thus gives a more relevant parameter to take into account pitting. This was then plotted with different conductivities using NaCl. The 3D equivalent of Rz, which is Sz, was also calculated for the 3D surfaces similarly.

5.2.2 Altered Electrolytic-dielectric composition

To manipulate the electrochemistry of electrolytic-dielectrics to control surface morphology , six sodium salts were chosen to alter the electrochemical machining mechanisms and behaviour on the EDM recast layer. NaCl (chloride), $NaHCO_3$ (carbonate), $NaNO_3$ (nitrate), Na_2SO_4 (sulfate), $NaNO_2$ (nitrite), and Na_2SO_3 (sulfite) were used. All salts were purchased from Fisher Scientific and were >98% purity.

Two conductivity levels of 600 and 1200 µS/cm were used for each salt with 40 seconds of machining time, which was selected due to the depth limitation of the Inconel 718 workpiece. The two levels were used to clearly show a difference in electrochemical removal. Control holes machined using DI were also drilled for comparison.

Prior to machining with each dielectric, the tool electrode was redressed on a graphite surface using DI to remove electrode curvature. After this, the dielectric was switched to the electrolytic solution and the fluid system flushed to ensure correct conductivity levels.

Recast layer depth measurements were obtained by calculating the recast layer area for 15 SEM areas of 90 by 80 µm and dividing the length of each area to obtain an average recast layer measurement.

The overcut of the holes were also measured using the Alicona G4. The overcut is defined as the increase in entrance hole diameter, which is always the largest increase in diameter across the hole, as compared to the size of the 1.9 mm electrode. The overcut is calculated as the resulting entrance hole

diameter minus the size of the electrode, and converted to a percentage increase.

The lateral gap was measured using 3D surface profilometry for all holes. This was then compared to the frontal gap, which was measured using sodium sulfite. The frontal gap is the same using all dielectrics, due to the similar electrical characteristics analysed in Chapter 6. This was then compared to the lateral gap to prove process mechanisms.

5.3 Results

5.3.1 Sodium chloride based electrolytic-dielectric

Figure 43 shows holes machined using NaCl formed electrolytic-dielectrics at varying conductivities, at the EDM parameters of 18 A peak current, 5 µs on-time, and 10 µs off-time. The surface view of the hole is shown in Figure 43a. Figure 43b shows the surface of the machined holes, with higher magnifications shown in Figure 43c-h.

The surface of the DI machined hole is shown in Figure 43c and is covered with typical recast layer features such as re-solidified material, workpiece and electrode debris, cracks, and oxides. The oxides are shown by the darker regions which usually surround the craters, while the lighter regions correspond to re-solidified material (craters). When the conductivity is increased to 200 µS/cm by increasing chloride anions available for electrochemical action, at the same EDM parameters, the surface shows two distinct zones. The upper region exhibits a zone in which the surface morphology is evidently dominated by electrochemical removal, whilst the lower zone still exhibits a characteristic EDM surface. The division between the EDM dominated zone and the electrochemical dominated zone is not step-wise, instead a transition occurs in which EDM pits decrease in frequency from the bottom of the hole towards the top. The bottom of the transition zone has a surface fully covered with EDM craters with minimal signs of electrochemical removal, while the top of the transition zone has a surface with no recast layer due to electrochemical removal. The centre of this transition zone is therefore

defined as the separation between the EDM and ECM zone and is used to calculate the EDM zone ratio, determined manually through SEM images which clearly show the transition zone, as shown in Figure 43. Although recast layer cross sections may aid in determination of the zero-recast point, due to the variable nature of the surface a single cross-section is not precise and may not be accurate, and as it is not possible to take several cross sections of the same hole due to the small size, surface SEM and roughness data which produce data over the entire surface are a necessary compromise. In this case, electrochemical removal has resulted in pitting of the recast layer through anodic dissolution resulting in its removal. The size of the discharge-dominated zone decreases with increased conductivity from 36% at 200 µS/cm to 11% at 1000 µS/cm as shown in Figure 44, due to the increased dissolution with increased conductivity. In this process, similarly with conventional electrochemical machining, no salts are observed on or below the surface in the SEM analysis. This is because they are either flushed away or react with the material and are then flushed away. Any residual electrolyte on the surface is washed away easily, thus salt contamination is never a concern with ECM

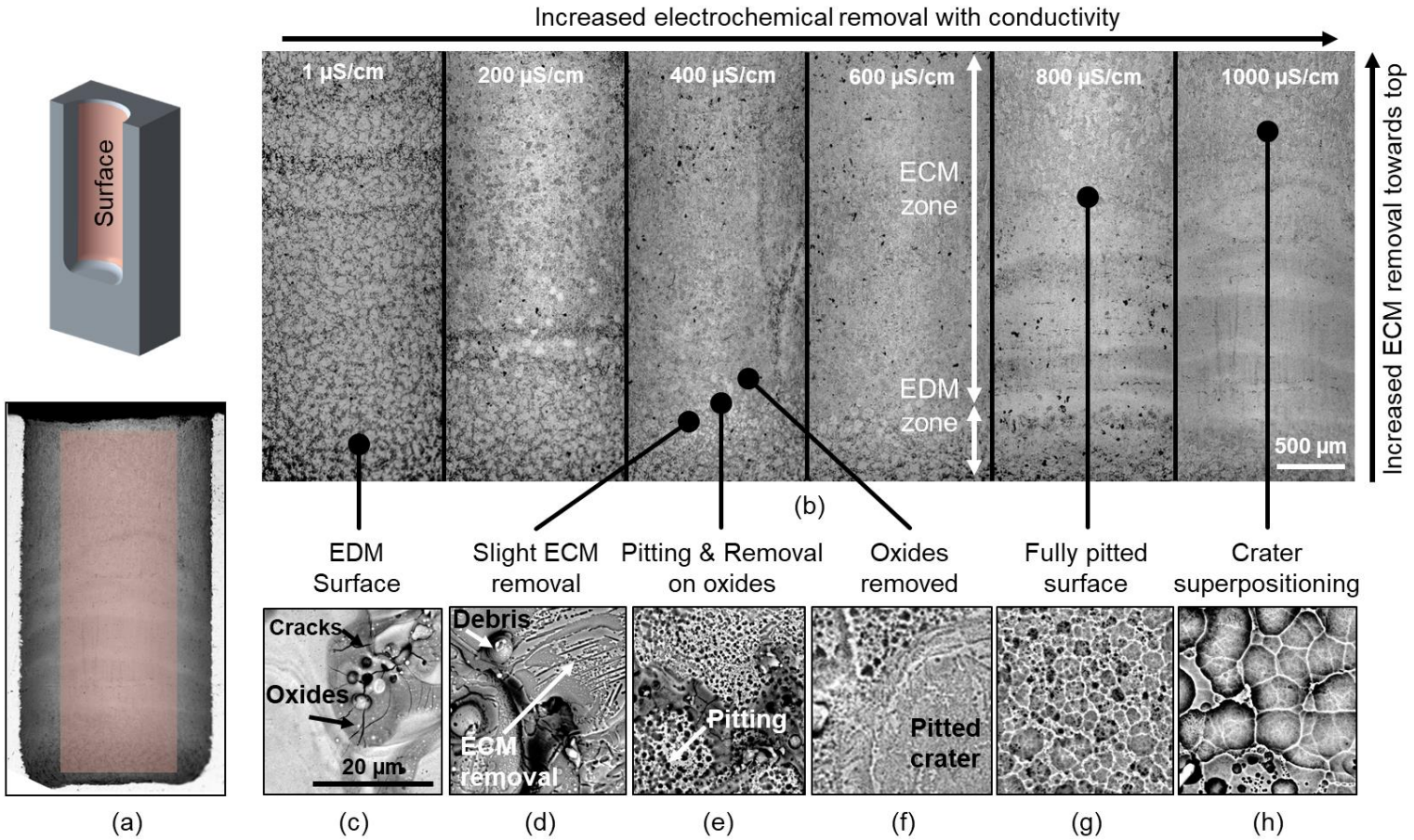

Figure 43 – Dissolution behaviour through SEM analysis. SEM back-scattered images showing the recast surface of holes. (a) Figure showing SEM view used in b-h and image of full hole and corresponding surface. (b) Holes from 1 to 1000 µS/cm conductivity using chloride to induce electrochemical dissolution. (c-h) High magnification micrographs of the surface showing increased chemical action. 3 holes were machined at each conductivity level.

Gradual electrochemical removal from the discharge zone to the dissolution zone is shown through Figure 43c–h, which takes place along the hole axis, and with the increase in conductivity from 1 to 1000 µS/cm. Slight electrochemical removal can be observed in Figure 43d. At this level however the EDM surface oxides are not removed. Increased electrochemical removal causes pitting and cracking of the oxides (Figure 43e), followed by removal of all oxides (Figure 43f), and finally a homogeneous surface with the entire recast layer removed (Figure 43g,h). The pit diameter is shown to increase from less than 1 µm to 5 µm at 1000 µS/cm.

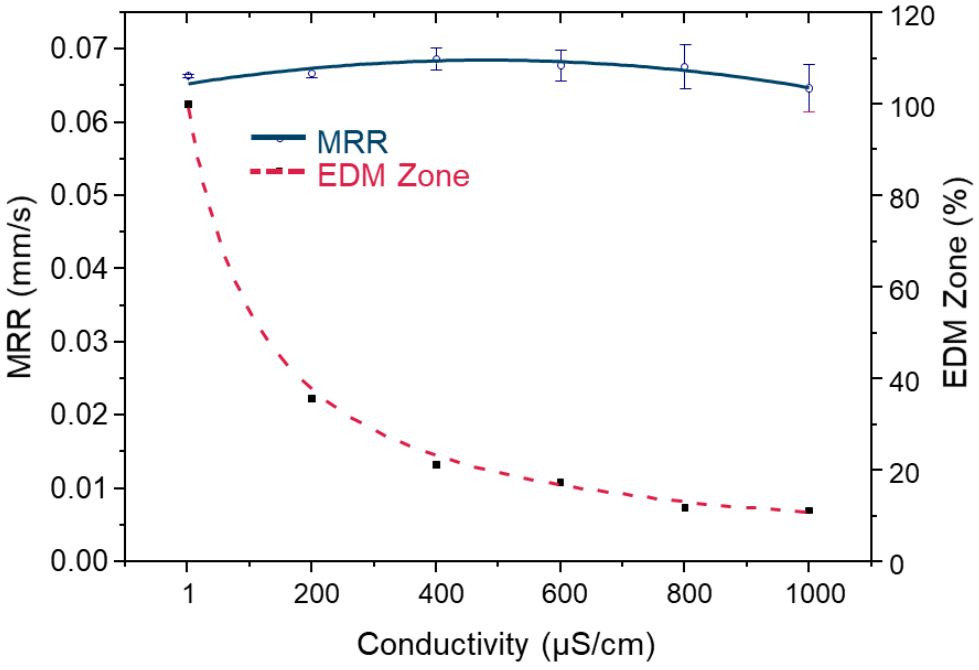

Figure 44. MRR and EDM zone data. Change in MRR and the EDM Zone (area dominated by EDM discharges compared to the ECM removed area) with conductivity, using NaCl to enable dissolution at five conductivity levels. MRR error bars represent ± SD from mean n = 3.

The increase in conductivity was also shown to have little influence on the overall material removal rate (MRR), shown in Figure 44, which implies that ECM removal has a very limited influence on the EDM removal mechanisms,

however with increasing conductivity a decreasing trend can be seen after 600 µS/cm. The EDM Zone was also shown to decrease with an increase in conductivity due to increased electrochemical strength.

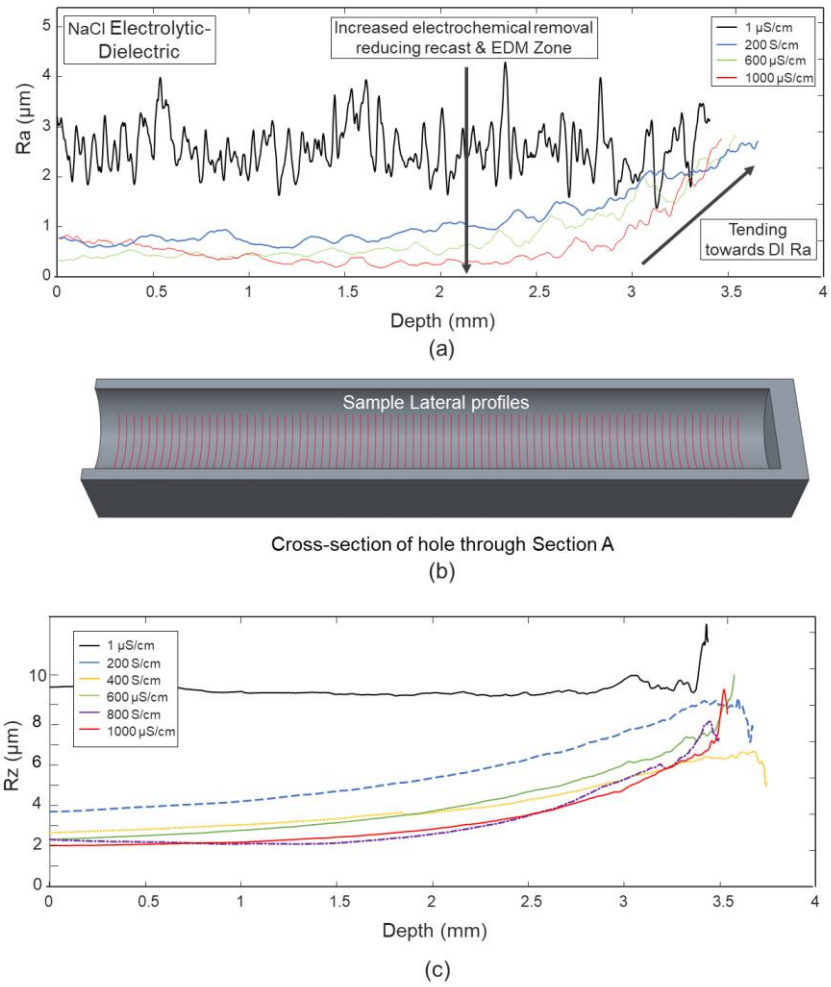

Figure 45. Clarifying the EDM and ECM zone through roughness analysis. (a) Effect of NaCl conductivity on the change in roughness with depth, showing two distinct roughness zones corresponding to the EDM and ECM zones(b) Diagram clarifying locations of sampled lateral profiles. c) Effect of NaCl conductivity on the change in Rz, a measure of the maximum heights measuring the largest amplitude of peaks and valleys across the surface.

Figure 45 shows a comparison of the change in Ra roughness along the depth of holes machined with NaCl electrolytic-dielectrics at 1, 200, 600, and 1000 µS/cm (400 and 800 µS/cm omitted for figure clarity). An increase from 1 to 200 µS/cm causes a profile with a considerably reduced roughness, with two

distinct zones. The top portion has a low roughness, which at 1.5 – 2 mm depth begins to rapidly increase tending towards the roughness of DI. By comparing to Figure 43 and Figure 44 we can correspond this to the EDM and ECM zones, relating the presence of EDM craters to the increased roughness and the smoothing of electrochemical removal to the decreased roughness. An increase in conductivity increases electrochemical strength causing more recast removal and smoothing and increasing the length of the low roughness ECM zone. NaCl at 1000 µS/cm shows a significantly reduced roughness and only begins to increase in roughness between 2.5 – 3 mm. The change in roughness data thus shows increased ECM removal in the ECM zone due to surface smoothing and increased roughness in the EDM zone due to electrical discharges. The lower roughness at the transition is due simultaneous ECM, however the high roughness of the EDM is not observed as this data could not be captured on the Alicona G5 due to the gradient of the hole end (curve upwards resulting in reduced light capture for height analysis). The Rz parameter was also used as this may be more relevant for pitted surfaces as it accounts for the maximum heights across a surface by considering the average of the largest heights (sum of valleys and peaks) across a surface. A similar trend to the Ra parameter was seen, however a larger roughness is seen for all surfaces as this parameter takes into account the largest heights as compared to the Ra mean parameter. Although this data shows recast removal through surface smoothing, it cannot be used to obtain the EDM zone or the zero recast point as it only shows a change in roughness. Thus SEM images, which clearly show craters and electrochemically removed surface, are currently the preferred method.

Figure 46 shows the decrease in roughness with an increase in dielectric conductivity and shows a clear comparison in surface roughness between an EDM surface and an electrochemically smoothed surface. The portion of the hole surfaces analysed was measured from the same distance (0.3 mm) from the top of each hole, in the electrochemical zone. Although the volume of material removed from the recast layer was not analysed, it can be assumed that a decrease in roughness, i.e., anodic levelling, correlates to increased material removed from the recast layer.

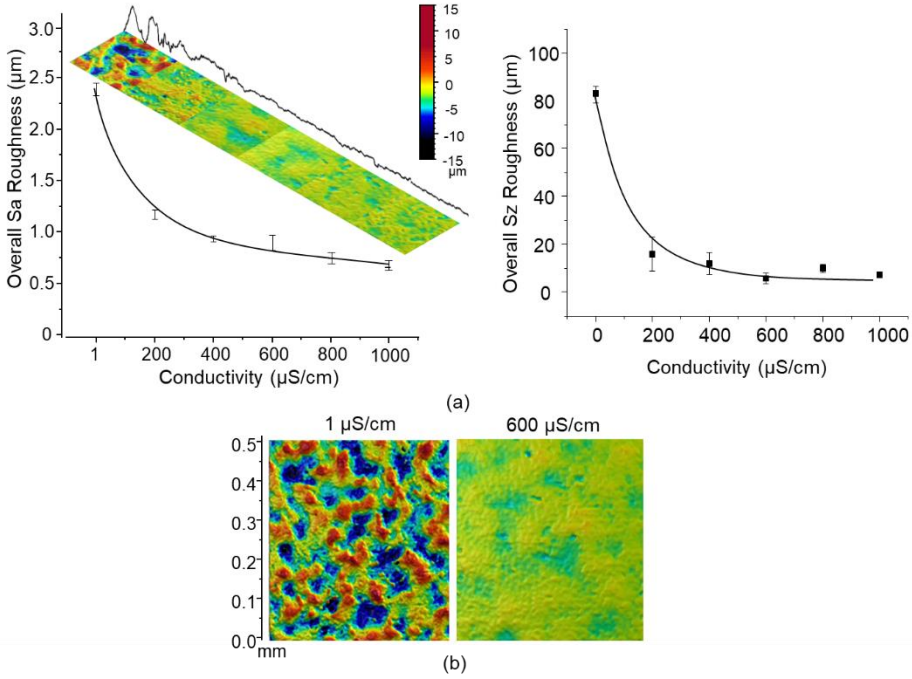

Figure 46. Roughness analysis of surfaces. a) Showing the change in roughness with conductivity in Sa and Sz with accompanying 3D/2D surface maps to visually show the change. Roughness error bars represent ± SD from mean n = 3. b) A close up of the difference between two conductivity levels caused by dissolution.

5.3.2 Altered Electrolytic-dielectric composition

Using NaCl, it was shown that electrochemical removal during EDM hole drilling can result in a hole with zero recast layer along the majority of the hole. In the case of chloride anions, anodic dissolution occurs by aggressive electrochemical pitting, which rapidly removes material. Within conventional ECM, both the current density distribution and the electrolyte can be altered to allow a higher degree of control over the material removal mechanism and ensure a high surface quality is generated [139-141].

Given the limited ability to control the electrical conditions across the inter-electrode gap (IEG) within this hybrid setup, different salts were used to control machined surface quality by altering the precise mechanism of electrochemical dissolution. With NaCl, aggressive chloride ions result in strong active dissolution [142]. Carbonate (HCO_3), nitrate (NO_3), and sulfate (SO_4) were chosen as less aggressive salts capable of forming passivating oxide layers when voltages are applied [103]. Nitrite (NO_2) was selected as it is commonly used as an anodic corrosion inhibitor due to its ability to form an effective compact passivating layer [143], while sulfite (SO_3) was selected due to its application as a corrosion inhibitor by acting as an oxygen scavenger [144].

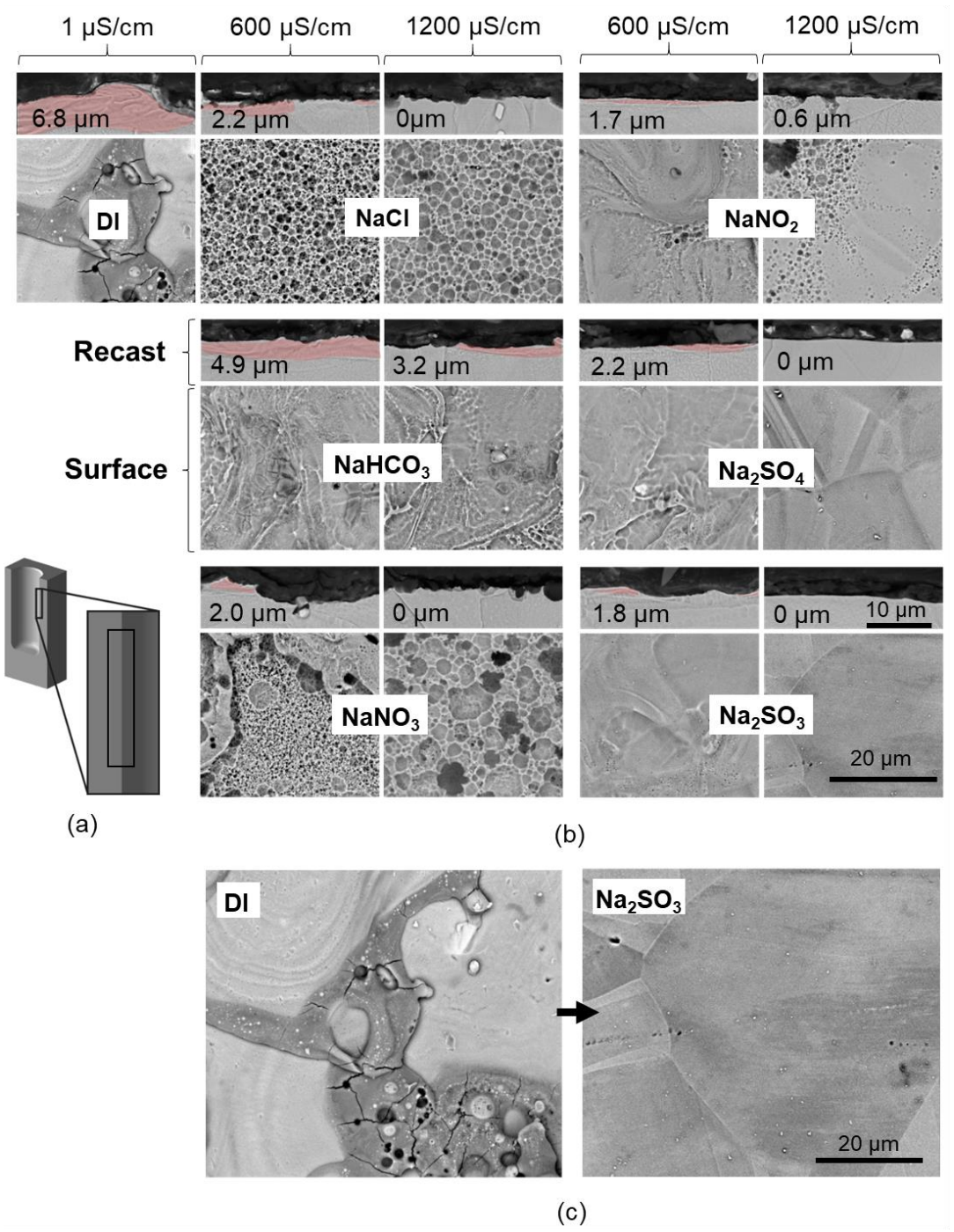

Figure 47. SEM analysis of surface and recast layers. a) Surface and recast layer views for both 600 and 1200 µS/cm holes, with recast area highlights in red. b) SEM-BS views of the surface and recast layer of the holes machined with the salt additives showing average recast layer depth c) Enlarged images of DI compared to sulfite.

Figure 47b shows that DI of 1 µS/cm conductivity produces an average recast layer depth of 6.8 µm. The recast layer is highlighted in red manually to visually

distinguish the layer from the bulk material for ease of viewing. At 600 µS/cm, NaCl causes pitting on the recast surface. This pitting removes material from the recast layer to an average recast layer depth of 2.2 µm, a reduction of 68% from deionised water, while the depth of the hole is the same as deionised water with a similar MRR as shown in Figure 68. When the conductivity is increased to 1200 µS/cm by increasing the amount of dissolved NaCl, the pitting action increases due to increased concentration of chloride ions able to transfer charge for material removal. The pit diameter and depth increases, shown in the SEM recast images in Figure 47b, and the entire recast layer is removed. The MRR of the hole, as shown in Figure 68, is similar at 600 µS/cm to DI (0.073 mm/s to 0.074 mm/s), however at 1200 µS/cm the change is more significant, from 0.074 mm/s to 0.057 mm/s (21.6%). This is likely due to the reduction in electrical discharges due to the higher electrical conductivity and increased charge transferred by anodic dissolution in the electrolytic-dielectric. In both cases, dissolution of the recast layer shows increased removal along the hole due to increased exposure time.

The EDM zone is seen to decrease with an increase in conductivity, with NaCl having the smallest zone followed by Na_2SO_3. $NaHCO_3$ is shown to have little decrease in EDM zone, while the other electrolytic-dielectrics have a similar decrease with conductivity. A decrease in MRR also results in a decreased EDM zone for all holes.

The accuracy of the process is shown in Figure 48, which shows a comparison of the overcuts between the electrolytic-dielectrics. With an increase in conductivity, the overcut increases, from a minimum of 3.8 % using Na2SO3 at 600 µS/cm to a maximum of 8.4 % using NaCl at 1200 µS/cm. The

overcut is the amount of diameter increase compared to the size of the electrode (1.9 mm). For example, a hole of top diameter 2.09 mm has an overcut of 0.19 mm (increase in diameter) or 8.4 %, and a lateral gap width is 0.09 mm (half of the overcut, or radius increase). For comparison, DI produces an overcut of 4.6 %. A hole with a small EDM zone, which has increased ECM removal, is thus shown to result in a larger overcut.

The overcut also confirms that the lateral gap where ECM occurs is larger than the frontal gap, as the increase in lateral gap ranged from 50 to 92 µm at 1200 µS/cm, which is larger than then the gap width in hole drilling EDM which can range from 5 – 50 µm. The lateral gaps are shown in Figure 49 for the electrolyte-dielectrics, which also show the frontal gap width. The estimated gap width can be calculated by E = V/d, where E is the electric field or dielectric breakdown limit of DI in V/m, V is the voltage in Volts, and d is the gap distance in m. As the concentration of the 1200 µS/cm electrolytic-dielectric in moles is very small (0.12 Moles for NaCl) the effect on the dielectric breakdown limit is negligible and can be ignored thus can be taken as 80 V/m [145, 146]. At the current setting of 19A the machining voltage is 14V, which is the same for all electrolytic-dielectrics for the EDM pulses (as obtained from the waveform experiments in Chapter 6), and the dielectric strength of DI is 80 x 10^6 V/m, therefore d = 14 / 80 = 17.5 µm. This is the minimum gap width that can be expected, which is the width produced at the point where EDM occurs. However, gap conditions (such as amount of debris, gas, turbulence) can affect this value.

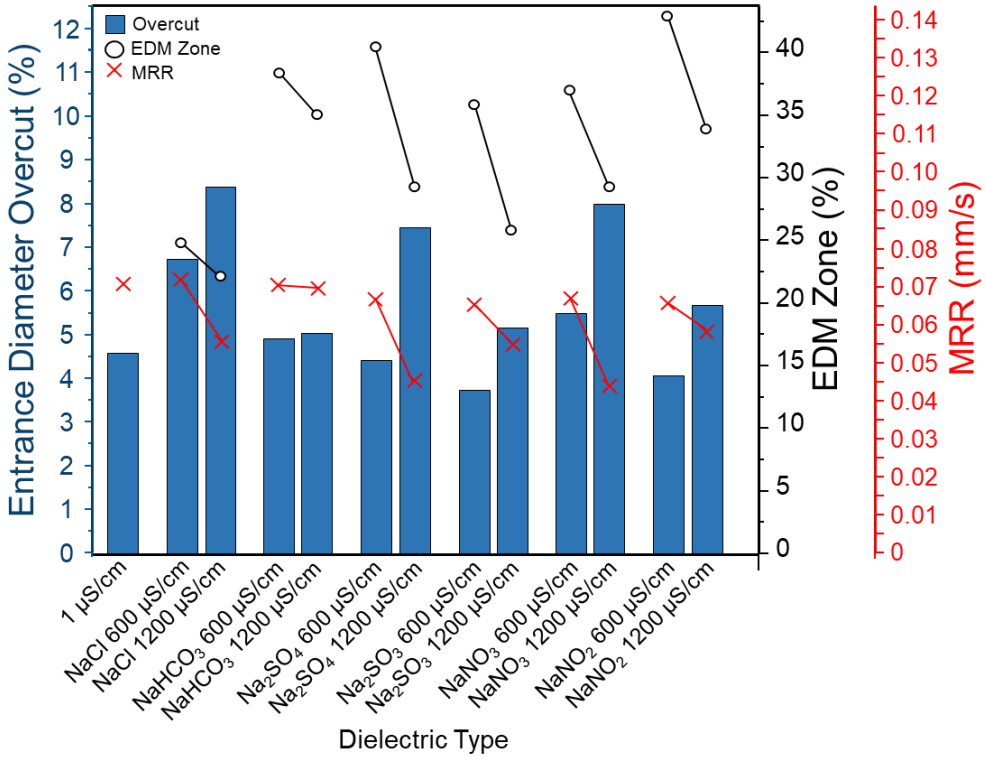

Figure 48 – MRR data, EDM Zone percentage, and Overcut. MRR and EDM zone for electrolytic-dielectrics at 600 and 1200 µS/cm compared to DI, showing a decreasing trend in MRR and EDM Zone at higher conductivities. A corresponding change in entrance hole diameter overcut is stated.

To confirm this value experiments to calculate the frontal gap were undertaken. The frontal gap is only affected by the EDM side of the process, which was confirmed in Chapter 6, thus the pulse characteristics (pulse shape, voltage, current) and breakdown limit are the same between electrolytic-dielectrics. Machining was halted at 3 points during the machining of the hole and the frontal gap was measured. The frontal gap changed from 15 µm at 5 seconds to 22 µm at 15 seconds, due to the gap being contaminated with debris and bubbles, and stayed around that width for machining. The frontal gap was also measured for Di and was similar around 20 µm, however both measurements varied by 2 – 5 µm due to gap conditions. The frontal gaps measured are smaller than all of the lateral gaps measured, which confirms

the hypothesis that a larger lateral gap is needed for electrochemical removal. The lateral gap also increases with conductivity, linking to the decreased EDM zone and larger zero recast area. The point at which the lateral gap is equal to the frontal gap is the point at which EDM discharges will occur and the EDM zone begins, which is shown through the EDM zone data discussed.

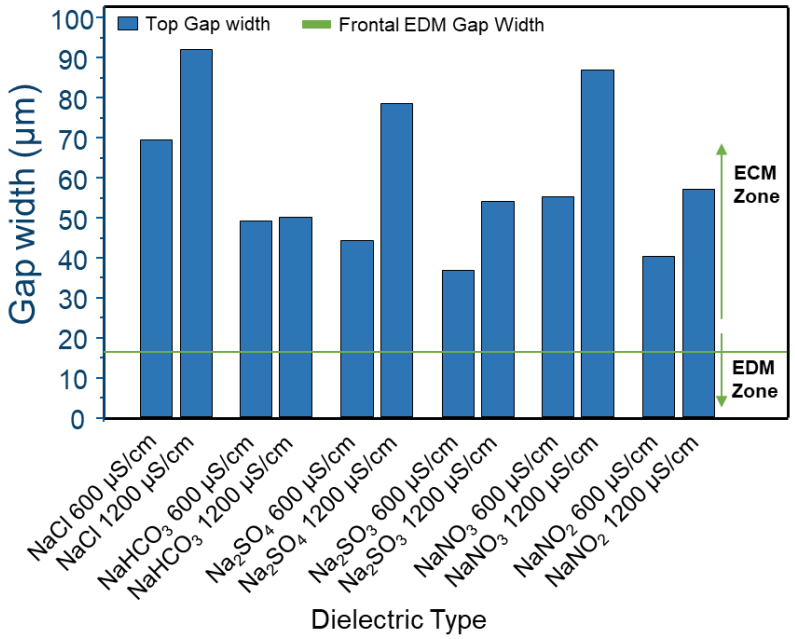

Figure 49. Showing the maximum gap widths in the machined holes for the electrolytic-dielectrics from the top diameter, and the Frontal EDM Gap width.

$NaHCO_3$ exhibits a surface with a protective oxide layer. These oxides are spread across the surface as compared to the EDM oxides, which are concentrated around craters. They can also be inferred to be mechanically weaker as surface oxides are reduced following sample preparation to view the surface, and no oxides remained after post-process polishing to view the recast layer, while EDM oxides remained attached. The reduced surface oxides are shown in Figure 47b, while an example of an undisturbed $NaHCO_3$ surface is shown in Figure *56*on the 3D surface (which was cut via W-EDM to reduce cutting force). This oxide layer is brittle and is prone to cracking, as

shown in Figure 47b by the darker angular sections and cracked regions, which results in the oxide layer spalling and being removed away by the high pressure flushing and thermal gradients. Regions of pitting are also observed. The recast layer depth at 600 µS/cm is 4.9 µm with only a 1.5% reduction in MRR compared to deionised water due to the restricted electrochemical machining of the recast layer, likely due to passive layer formation. An increase to 1200 µS/cm reduces the recast layer depth to 3.2 µm due to the increased ability to carry charge, with a reduction in MRR of only 2.6%. In both cases, the MRR is similar to that of deionised water which may be explained by the limited electrochemical removal due to the oxide layer, in which electrical charge is used in oxide layer formation rather than material removal.

$NaNO_3$ at 600 µS/cm produces a complex surface with sections of completely removed recast layer while some areas are only partially dissolved as shown by the two district regions in Figure 47b, likely due to the variable electrical conditions within the IEG. The average recast layer depth is 2.0 µm with a reduced MRR of 6.1%. This value is similar to the recast depth for NaCl, which may be accurate for the chemically removed areas, however due to the method of measuring average recast depth, by sectioning the hole, it is possible that the true average recast thickness is larger if all non-removed sections of the recast layer are factored in. When the conductivity is increased to 1200 µS/cm the surface is covered by pits and the entire recast layer is removed due to increased chemical effects.

$NaNO_2$ produces a surface with minimal pitting with no apparent oxides on the surface remaining, however with some regions with increased pitting due to preferential chemical machining as discussed earlier. Due to this the recast

layer has decreased to 1.7 µm with a reduction in MRR of 7.8%. With an increase to 1200 µS/cm the recast layer depth is only 0.6 µm with a reduction in MRR of 18.4% and a similar decrease in MRR compared to $NaNO_3$. All craters and protrusions have been mostly removed through electropolishing and a surface is produced with regions of pitted and smooth metal. However, at certain preferential electrochemical machining regions pitting occurs excessively.

The surface of the Na_2SO_4 hole is similar to $NaNO_2$, however less recast layer is removed but with minimal pitting of the surface. Anodic dissolution is thus more uniform and does not form oxides or excessive pitting. At 600 µS/cm the recast layer depth is 2.2 µm with a reduced MRR of 6.7% compared to deionised water, and a higher MRR compared to $NaNO_3$ and $NaNO_2$. When the conductivity is increased, the recast layer is significantly levelled with no sign of pitting or oxide layers. Preferential removal at grain boundaries can be seen. The MRR is also decreased by 35.8%.

Na_2SO_3 has an average recast layer depth of 1.8 µm and no pitting, with a reduced MRR of 8.4%. At 1200 µS/cm the entire recast layer is removed and a finely polished surface can be seen showing the grain boundaries with no edge removal in a similar mechanism to Na_2SO_4. In this case the MRR has only reduced by 22.6%.

5.4 Discussion

5.4.1 Removal Mechanism

It is now possible to deduce the working mechanisms of the process. From Figure 43 it was shown that two distinct regions on the surface are present, the EDM zone and the ECM zone, separated by a transition area. These zones change proportions with increased conductivity, which then reduces the EDM zone.

This change in EDM zone can be explain by the macro-scale of the process. When machining starts, the discharge gap, D_d in Figure 50, is equal on the frontal and side areas. This results in electrical discharges throughout the entire surface, therefore dominating removal while electrochemical removal is limited. Once the side gap, D_c, begins to expand larger than the discharge gap, due to simultaneous electrochemical removal, secondary discharges [64], and debris bridges, removal at the side walls begins to be dominated by anodic dissolution. Although anodic dissolution occurs throughout the entire surface which is exposed to electrolytic dielectric, EDM only occurs on the frontal area of the electrode, i.e. where the gap distance is shortest. When a sufficient side gap is reached, only electrochemical removal occurs as the gap is so large the likelihood of discharge is effectively reduced to zero. Thus, electrolytic behaviour of the working fluid dominates in this region. The larger lateral gap compared to the frontal gap was shown in Figure 49 which that a larger lateral is needed for ECM removal, and that increased ECM removal is linked to a larger lateral gap. The reduced electrical discharges on the side walls also results in reduced electrode side wear proportional to the conductivity,

resulting in reduced electrode frontal curvature due to discharges focussing on the frontal area. The minimum EDM zone can therefore be defined as shown in Figure 51, in which the fixed EDM zone is equal to the sum of the corner radius and spark gap, as this region is the area that, in addition to the frontal area, advances towards the workpiece material to initiate electrical discharges.

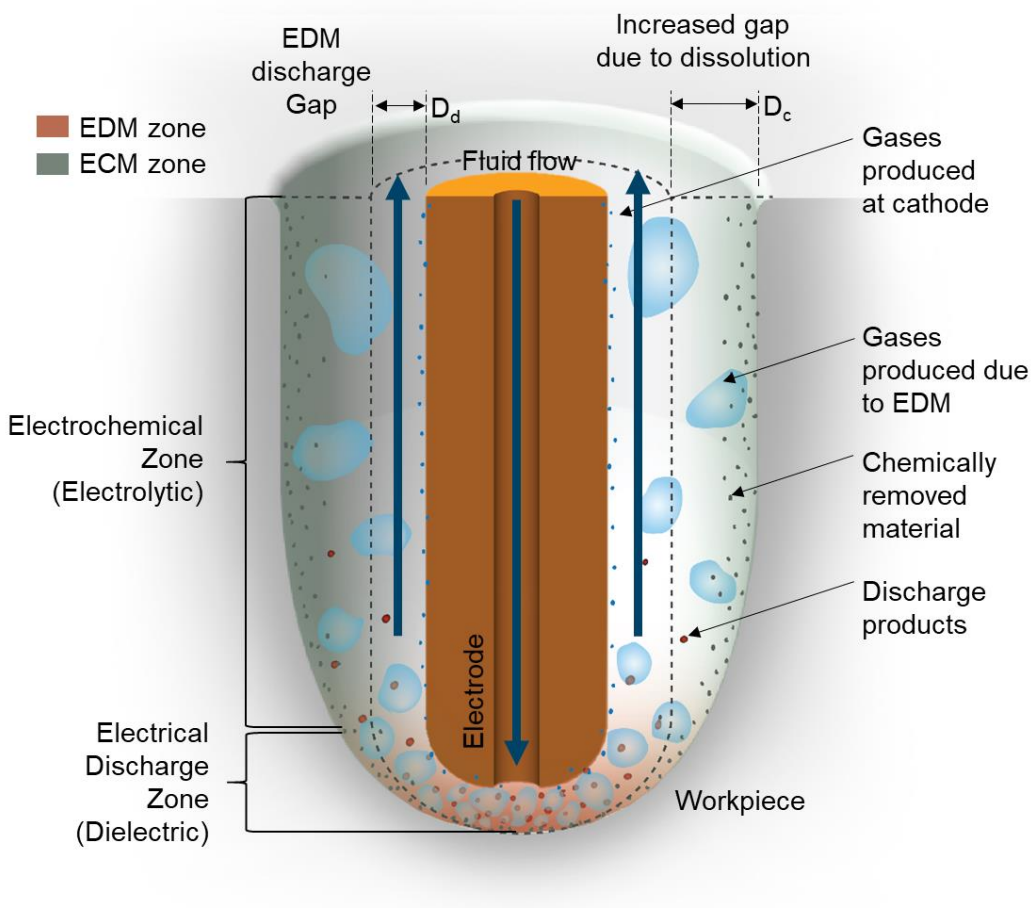

Figure 50. Proposed process mechanisms. EDM and ECM hybrid process showing simultaneous chemical and discharge removal. Distinct EDM and ECM zones are present in the process. ECM zones caused due to increasing gap, reducing discharges in the regions. Frontal area gap is smaller than EDM discharge gap resulting in sparks.

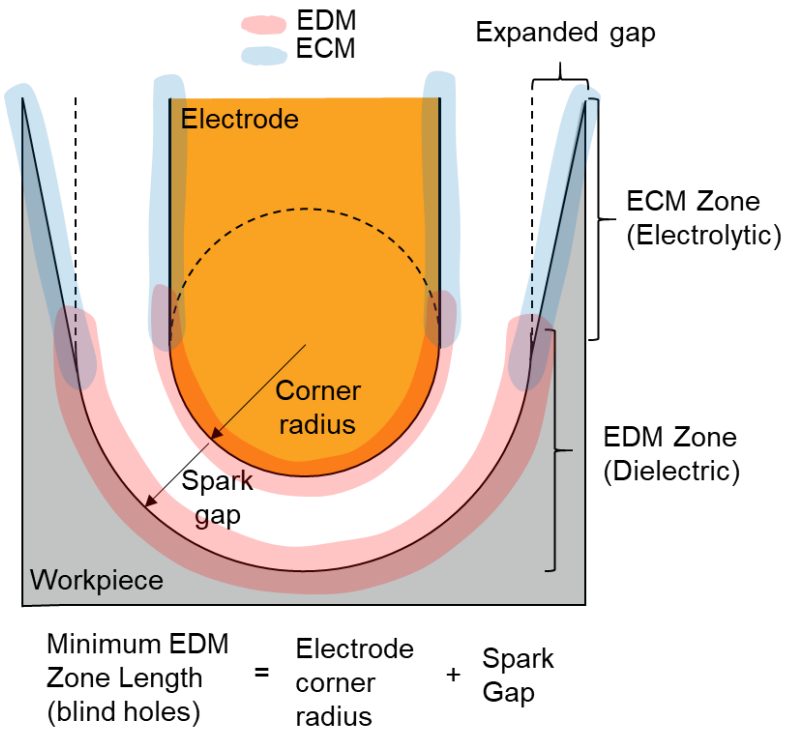

Figure 51. Showing theoretical calculation of the EDM zone length for blind holes. Red and blue highlighted regions show areas dominated by EDM and ECM removal.

Therefore, the side area can be considered electrolytic locally, while the frontal area as dielectric. EDM discharges are thus used to advance hole depth, while anodic dissolution is used to remove recast layer, simultaneously. In this case, the electrochemical side does not significantly affect the EDM side, as shown by the minimal change in MRR with conductivity and EDM zone. This may be due to the increase in gases (due to production of cathodic hydrogen and anodic oxygen, which increase with conductivity) and so promotes EDM sparking due a decreased breakdown strength and preferential discharge paths caused by debris accumulation at bubble interfaces. It may also be the case that at the low conductivities used, electrical breakdown is not significantly hindered, therefore breakdown still occurs. If the dielectric conductivity is increased by a magnitude, then it can be predicted that pulse

energy would cause high electrochemical current through the electrolyte which would clearly hinder breakdown. This is the case in ECDM in which current causes electrochemical gas generation instead of a standard discharge, and the actual discharge only occurs between the boundary of the large gas bubble and electrode, EDM and anodic dissolution can therefore be considered to occur simultaneously on the macro scale, while on the individual discharge scale they occur concurrently.

The white dotted line region in Figure 50 shows electrochemically removed material, while the inverse region of diameter D_d shows the material removed via EDM only. This results in a surface characteristic of anodic dissolution, whilst exhibiting zero discharges on its surface. The red region shows the EDM zone, which is also the zone with increased temperature. The green zone shows the ECM zone, in which the concentration of ECM removed material reduces further away from the surface (shown by the gradient).

On the microscale, increased anodic dissolution through pitting occurs when conductivity is increased, due to a higher concentration of aggressive chloride anions (increasing charge passed) reacting with the anode workpiece surface liberating metallic hydroxides into the fluid due to its non-passivating nature. This increase in dissolution is also seen along the axis of holes due to increased exposure time of the workpiece surface to the anions available in the electrolytic dielectric, with larger and deeper pits occurring towards the entrance of the hole which coalesce into a smoothed surface. The decrease in roughness can also be explained by anodic levelling, in which protruding sections of recast are preferentially removed by the primary current distribution

[147], which is intensified with an increase in dielectric conductivity and exposure time.

5.4.2 Manipulating anodic dissolution mechanisms to control surface morphology

In the case of chloride anions, anodic dissolution occurs by aggressive electrochemical pitting (due to its non-passivating nature), which rapidly removes material. Between Figure 43d–h, the change in pit morphology can be explained by superposition of pits. As machining time increases the pits increase in diameter and begin to overlap which cause the holes to merge, resulting in a markedly smoother surface [36]. This is shown more clearly in Figure 52, where an EDM crater shows gradual chemical removal with areas of pit super-positioning.

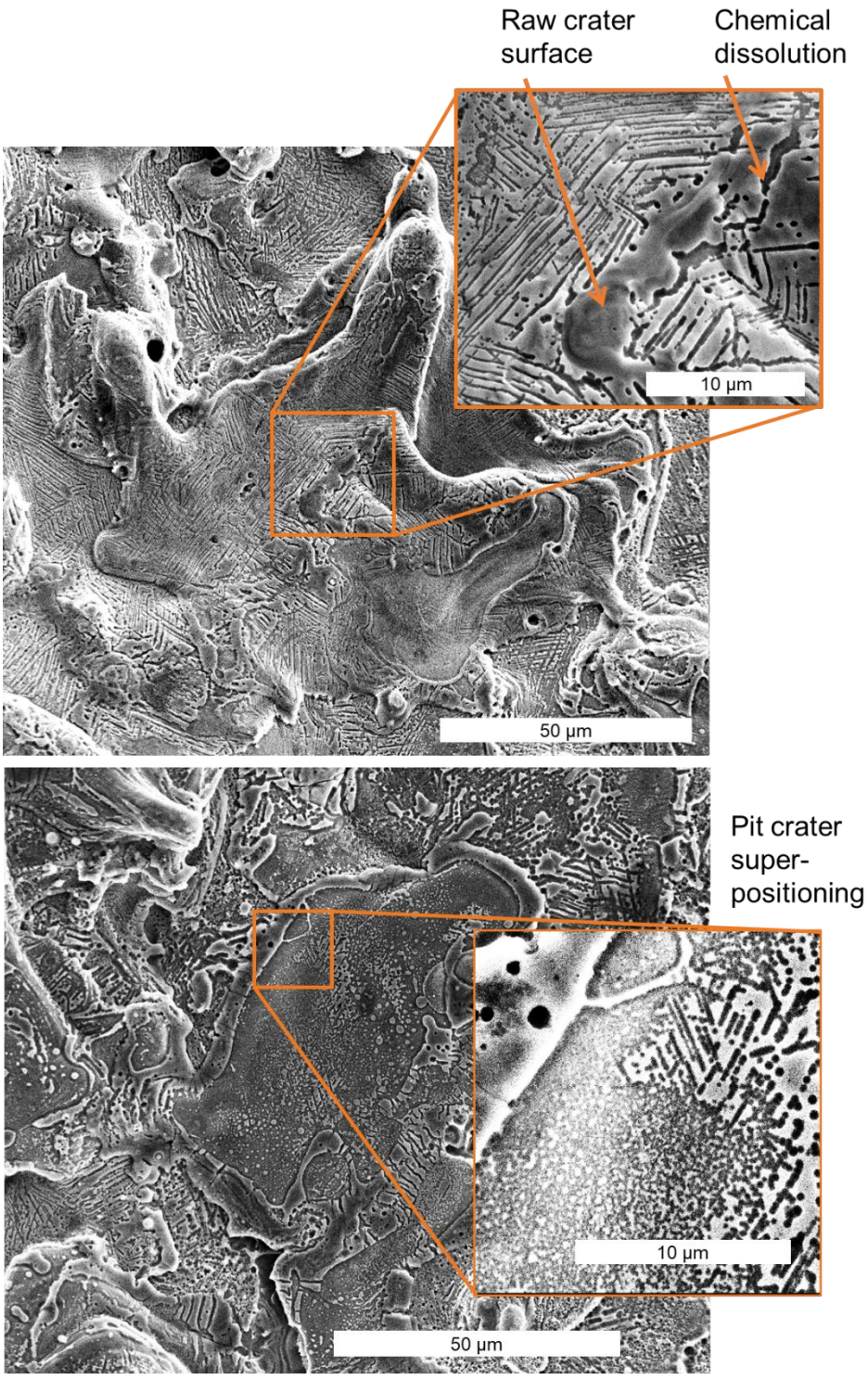

Figure 52. SEM images showing electrochemical dissolution via pitting and super positioning of pit craters.

Figure 53 shows that for NaCl the aggressive pitting results in a small EDM zone as a considerable amount of material is removed. The transition zone shows strong pitting of craters. In the mid-section of the 600 µS/cm hole, crater

outlines can be seen where, due to the geometry of the craters and preferential anodic dissolution at crater edges, remnants of craters are observed even though most of the recast layer has been removed. At the top of the hole the surface then becomes homogenous. The 600 µS/cm hole can thus be shown to have a large change in surface morphology along the hole. With an increase in conductivity, the hole surface morphology is more consistent along the hole, however pit superposition is more pronounced and electrochemical removal can result in large pits and excessive removal and so is considered to have limited control.

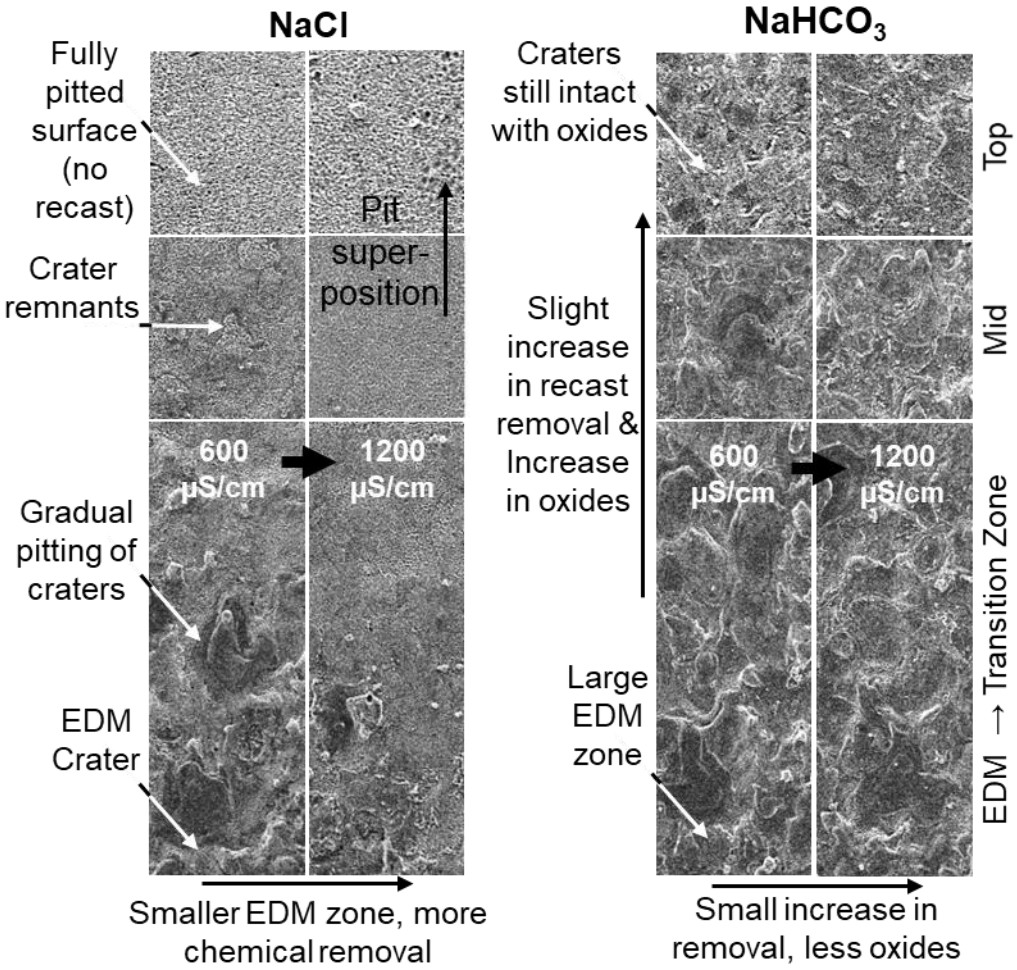

Figure 53. Change in surface morphology along the hole surface for NaCl and $NaHCO_3$ electrolytic-dielectrics.

For $NaHCO_3$ the electrochemical effect on the recast layer is notably different. With passivating electrolytes, the anions (e.g. bicarbonate) cause electrolysis and cause oxygen to react with the base material to produce a protective oxide layer, which restricts further chemical removal of the metal [147]. This oxide layer is seen throughout the surface, as compared to the concentrated EDM oxides, and is also mechanically weaker. This was because in Chapter 5.3.2, in which the samples were sectioned for recast depth analysis, no ECM generated were observed on the recast layer, however EDM oxides could be seen for DI. During the process, due to the brittle nature, cracks and spalling occur due to flushing and temperature gradients. The bicarbonate ions then react with the exposed metal to remove more of the recast layer. Oxide film breakdown can also be explained by transpassive dissolution due to the formation of unstable oxides, in which the oxide film begins to break down, further aiding oxide film spalling, thus enabling further pitting or oxide formation [103]. Other areas on the surface also exhibit electrochemical removal by mild pitting (compared with chloride). At certain conditions pitting can occur which leads to a reasonably smooth surface as pits superimpose [105]. This implies that a cyclic process of passive layer formation, layer removal, pitting, and passive layer reformation occurs throughout the machining of a hole. From Figure 53 there is little difference between the EDM zone and the electrochemically removed area due to the generation of oxides limiting electrochemical removal. Craters are mostly intact with some of the recast removed. There is also little change in surface morphology along the hole depth due to the limited electrochemical removal,

thus the electrochemical removal is more controlled, albeit with limited recast removal and generation of surface oxides.

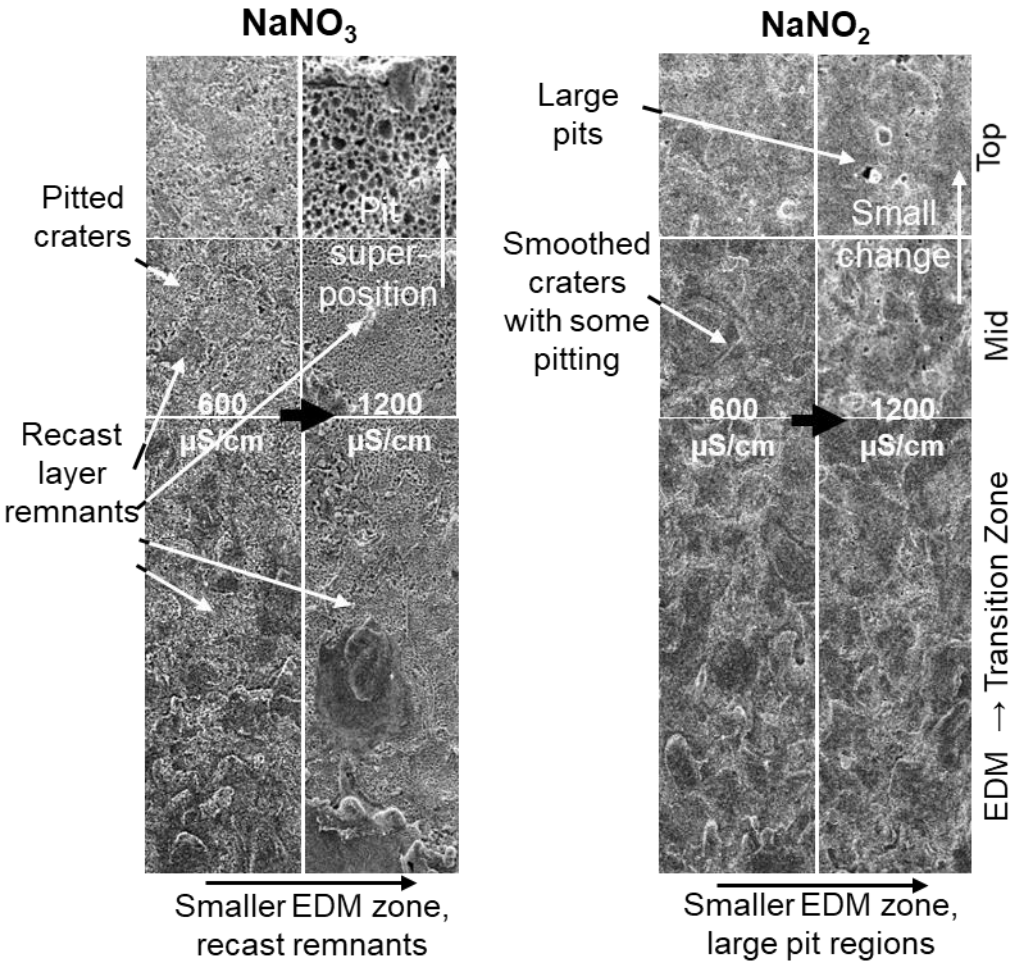

Figure 54. Showing the chance in surface topography along the hole due to differences in electrochemical effects with $NaNO_3$ and $NaNO_2$.

Figure 54 shows the change in surface for $NaNO_3$ and $NaNO_2$. Unlike $NaHCO_3$, for $NaNO_3$ the oxide layer is not clearly visible on the surface after machining, which may be due to the increased electrochemical removal compared to oxide formation which results in the oxide layer not building up and instead being continuously removed (due to the high-pressure flushing, thermal gradients, and pitting). Localised dissolution may be due to the electrochemically generated oxide film breakdown at defect sites such as

pores within the oxide layer, which causes localised breakdown and pitting [148]. Further removal occurs more easily in these ‘activated’ areas compared to areas protected by oxides, compounding material removal. Even after re-formation of the oxide layer in the pitted areas, and the removal of the oxide layer in other areas, the two distinct regions will remain. Another possible reason for localised electrochemical removal is that anodic dissolution is reduced on the areas with EDM generated oxides, which usually surround the craters. Thus, dissolution first occurs on the exposed metal followed by the EDM oxide regions after these oxides have spalled off. This is also seen for $NaHCO_3$, but not for NaCl due to breakdown being actively promoted with more breakdown points per unit area, while for $NaHCO_3$ and $NaNO_3$ there are fewer breakdown points, which then enlarge. Conversely, in some areas the EDM generated oxides may spall off first, which then results in dissolution in those areas due to preferential chemical dissolution. The pits are considerably larger than NaCl. One explanation for this is due to the hole depth and MRR being significantly less than NaCl (a reduction of 37.7% in MRR from deionised water), due to reduced electrical discharges, which would increase the time for electrochemical machining on the smaller hole internal surface, compared to the deeper and thus larger area NaCl machined hole. This implies that if there are fewer electrical discharges occurring per second, which would result in a shallower hole, then anodic dissolution of the recast layer will increase due to the smaller electrochemical machining area that effectively focuses the current density. Thus, controlling the amount of electrical discharges is key to controlling the amount of dissolution of the recast layer. Figure 54 shows a change in surface morphology similar to NaCl. For 600 µS/cm craters are

gradually removed via pitting leading to a fully pitted surface. However due to the dissolution mechanisms as discussed, controllability is limited due to electrochemical removal resulting in areas of non-removed recast. At 1200 µS/cm pit superposition and localised attack occurs resulting in large pits, while some portions of the surface have remaining recast.

The nitrite ion from $NaNO_2$ is well known to be a passivating corrosion inhibitor due to it easily forming an effective oxide film on a surface [143, 149]. Compared to $NaNO_3$ it can be assumed that the formed oxide layer is more stable thus reducing the rate of electrochemical dissolution resulting in a surface which is more uniformly machined with reduced pitting. This can be explained though the diffusion-controlled removal mechanisms, in which electrochemical removal is limited due to either a viscous layer, salt layer, or thin oxide film [147]. Figure 54 shows that surface morphology is more controlled than $NaNO_3$ with no remaining recast regions, however preferential pitting occurs resulting in areas of excessive electrochemical removal.

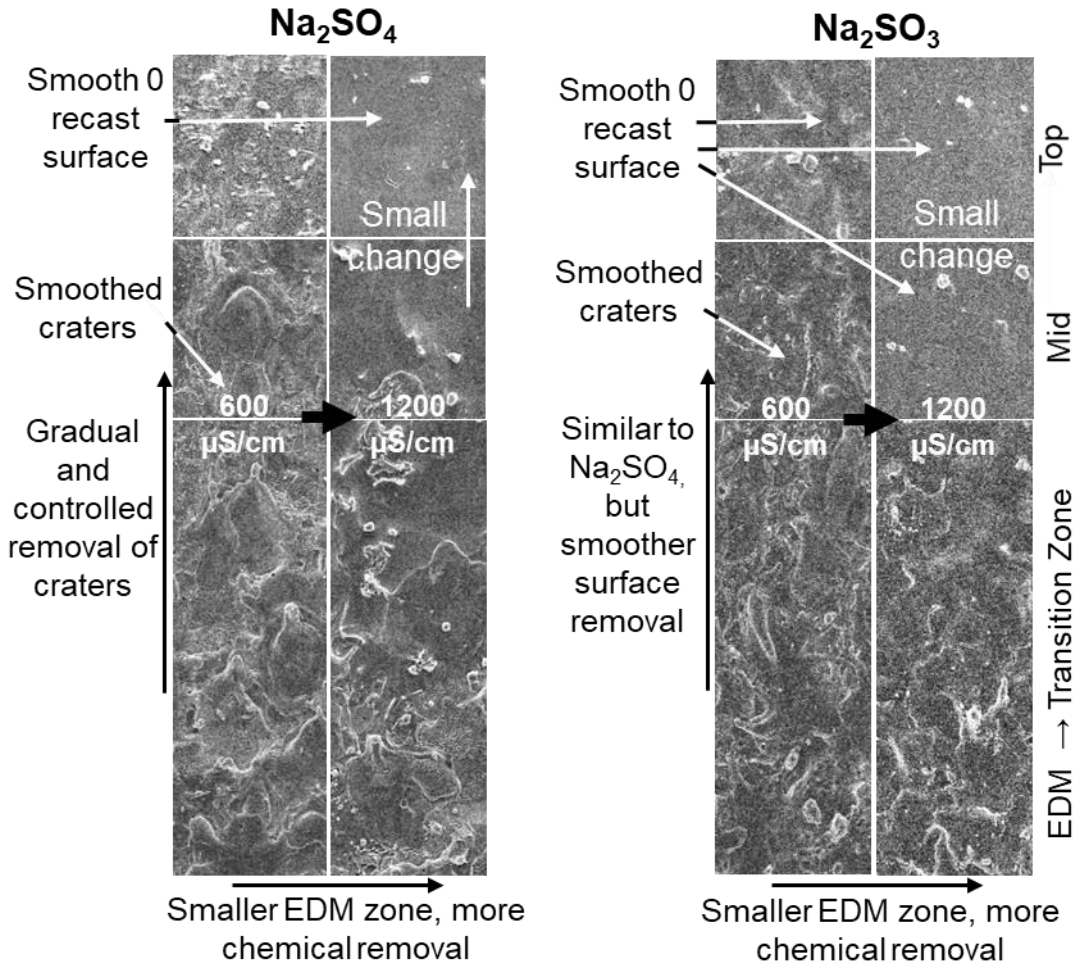

Figure 55. Showing the chance in surface topography along the hole due to differences in electrochemical effects with Na_2SO_4 and Na_2SO_3.

At 1200 µS/cm Na_2SO_4 exhibits increased removal with no sign of pitting or oxide layers, as shown in Figure 55, explained due to the oxide layer formed controlling chemical removal of the base material via controlled diffusion, resulting in a polished surface. To achieve this, a thin and compact film must form which is contaminated by significant amounts of anions from the solution while also having sufficient ionic conductivity to allow for the passage of cations at a high rate [105]. Figure 55 shows a controlled and gradual removal of the surface recast layer leading to smooth surface near the top of the hole, for the 600 µS/cm hole. At 1200 µS/cm a large portion of the surface has

similar morphology (smoothed) thus can be considered to be a controllable surface with no excessive electrochemical removal.

Na_2SO_3 exhibits a finely polished surface showing grain boundaries and little edge removal. Na_2SO_3 is a reducing agent, commonly used as a corrosion inhibitor by the mechanisms of oxygen scavenging which removes dissolved oxygen from the solution by oxidising to Na_2SO_4 [144]. A decrease in oxygen content would then decrease the acidification of the zone [103] thus reducing the rate of chemical dissolution further, as compared to Na_2SO_4. Na_2SO_3 is therefore shown to produce the most favourable surface in terms of surface integrity with no apparent surface defects at this length scale. Figure 55 shows a change in surface morphology similar to Na_2SO_4 but with increased electrochemical removal and leading to a smoother surface. Na_2SO_3 can be considered to be the most controllable, in terms of no excessive electrochemical removal and with a large proportion of the surface exhibiting similar and preferred surface morphology.

The small reduction in MRR between conductivities can be attributed to the reduction in electrical discharges due to the higher electrical conductivity and increased charge transferred by anodic dissolution in the electrolytic-dielectric. Another explanation is that the increased electrical conductivity increases gap width which increases the machining voltage, thus resulting in less material removed per discharge (even at the same energy) due to decreased energy density, energy dissipation, and heat flux [134]. The increased gap width also may result in increased high voltage intervals due to the larger gap [150, 151]. An increase in gap was also shown to increase the bubble diameter, likely due

to increased energy used in bubble generation instead of metal removal, which was also shown to increase impulse force [45] and vapour jet force [36] however due to decreased material melting MRR is not affected by the increase in impulse force. Although there are limited studies on the effect of conductivity on spark gap, a comparison can be made with studies that added conductive powder to the dielectric. In all cases the gap width and voltage was said to increase with the breakdown limit decreasing [152-154].

From Figure 68 it was shown that the EDM zone decreases with conductivity for all electrolytic-dielectrics. This is due to increased ions available for anodic dissolution increasing charge passed and removed material, as shown through Faraday's Law which relates charge to material removed. NaCl was shown to have the smallest EDM zone due to it being the most aggressive additive (non-passivating) and due to its likely higher current efficiency due to being non-passivating, followed by Na_2SO_3 which was explained to be the least aggressive (passivating). A smaller difference with an increase in conductivity was also shown for Na_2SO_3 and $NaNO_2$, as compared to Na_2SO_3 and $NaNO_3$ respectively. This is also due to these salts being less aggressive due to the differences in chemical dissolution mechanisms as discussed previously (corrosion inhibition for $NaNO_2$ and oxygen scavenging for Na_2SO_3).

It was shown that hole accuracy was influenced by the electrolytic-dielectrics in terms of affecting the overcut. Electrolytic-dielectrics with increased electrochemical removal, such as NaCl and higher conductivities, will remove more material on the sidewalls in addition to the EDM overcut,

therefore potentially negatively affecting hole accuracy. Compared to DI, which had a 4.6 % overcut, NaCl at 1200 µS/cm produced the lowest accuracy with a 8.4 % overcut. However, Na2SO4, which was shown to be least aggressive and most controllable salt, produced an overcut of only 5.2 % at 1200 µS/cm, an increase of only 1.4 % overcut compared to DI. This small increase in overcut and decrease in MRR is a fair compromise for a surface with no recast, and can easily be addressed through improvements to process control, process optimisation, and electrolytic-dielectric composition which will be discussion in Chapter 6 and in future work.

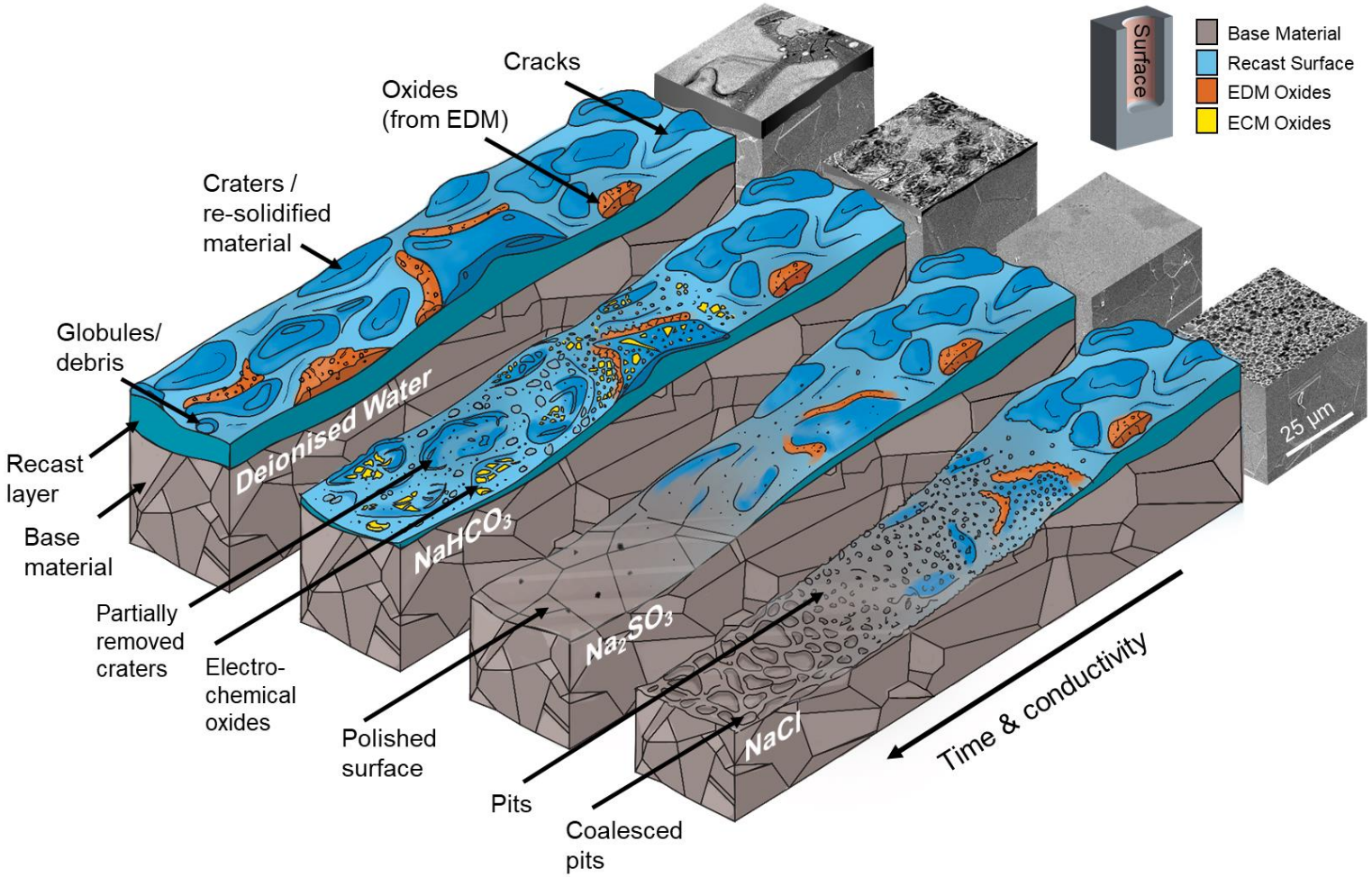

Figure 56. Altered surfaces through different chemical mechanisms. Showing the different surface morphologies due to different types of chemical effects on the recast layer. SEM images of each surface to relate illustration to machined hole surfaces.

The electrochemical part of the process can thus be generalised into three discreet mechanisms - oxide-limited passive removal, electropolishing, and aggressive (non-passivating) removal, as shown in Figure 56 with $NaHCO_3$, Na_2SO_3, and NaCl, respectively.

DI shows a typical EDM recast layer with surface defects. $NaHCO_3$ shows a surface with limited electrochemical removal and the presence of electrochemically induced oxides. Here electrochemical removal is limited due to energy (charge) being used in production of surface oxides instead of removing recast layer material. Material is gradually removed, which increase with time and conductivity leaving a surface with partial craters and oxides, as also shown in Figure 57. In electrochemical machining, gas is generated from the cathode via hydrogen evolution. Oxygen can also be generated on the anode surface, which is promoted when oxide layers are present [103]. For $NaHCO_3$ it can be assumed that gas generation is high due to the oxide layers formed on the surface, while for Na_2SO_3 gas generation may be low due to no presence of oxides. More energy is thus used for $NaHCO_3$ instead of removing material compared to Na_2SO_3, resulting in a lower current efficiency.

The second mechanism combines electrical discharges with electropolishing. Here the recast layer is removed gently through mass transport controlled means, resulting in a surface with little pitting with most of the recast layer removed. This may be through a compact thin film or viscous salt layer. Na_2SO_4 is shown to gently remove material with some pitting which shows breakdown of the layer, while Na_2SO_3 gently removes the recast layer with minimal pitting, leading to a smooth and controlled surface with no pitting. SO_3^{2-} is also an oxygen scavenger which removes dissolved oxygen from the

solution by oxidizing to SO_4^{2-} [144]. This might alter the pH of the machining zone, leading to slow and controlled dissolution resulting in a polished surface.

The third mechanism involves aggressive pitting, and these pits grow in size with time and increased conductivity, ultimately coalescing into a smooth, yet pitted surface. In Figure 57, NaCl is shown to remove material via aggressive pitting which lead to pit superimposition.

$NaNO_3$ and $NaNO_2$ show surfaces with a mixture of electro-polishing and pitting. As shown in Figure 57, $NaNO_3$ removes material by pitting in some areas, while having limited removal in some, leading to a mostly pitted surface with spots of remaining recast. $NaNO_2$ shows a surface with minimal pitting, leading to a smooth surface with large pits at preferential areas.

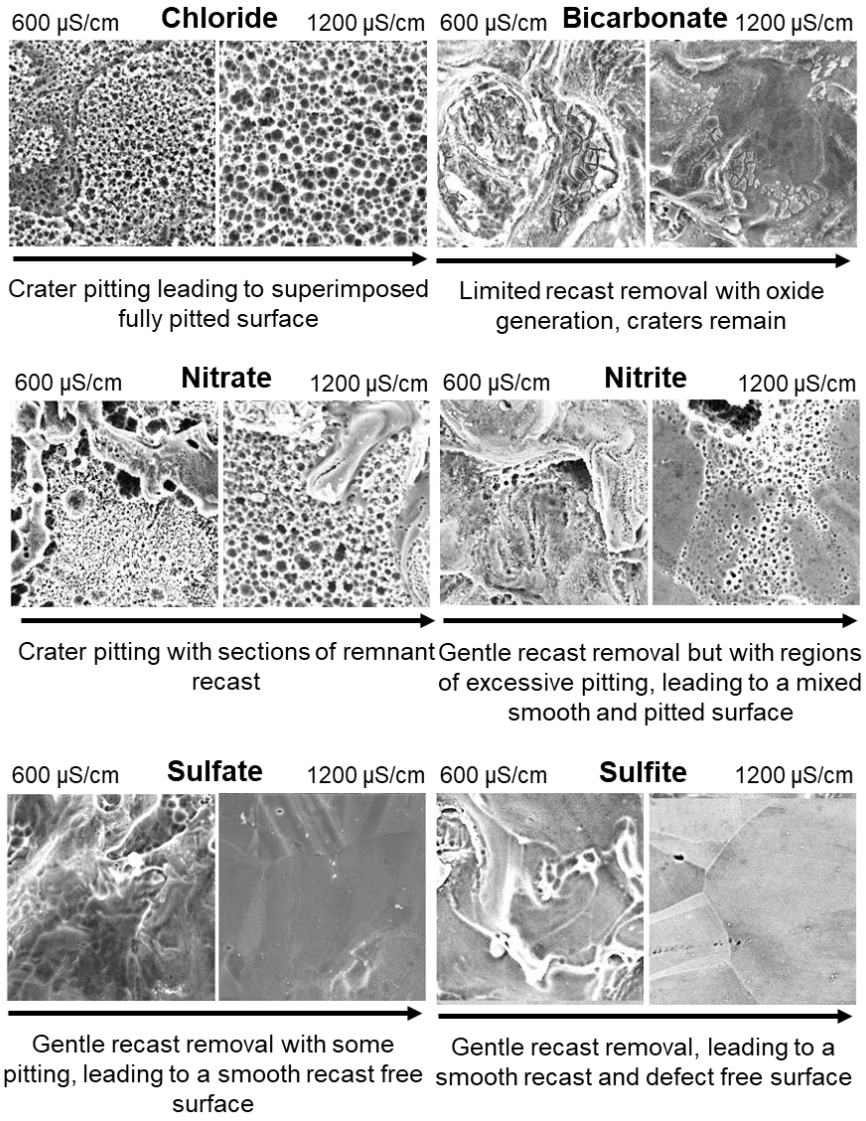

Figure 57. Shows a summary of the electrochemical removal mechanisms of each electrolytic-dielectric.

5.5 Conclusion

A method to remove the recast layer in a single stage process was produced and was shown to effectively remove the recast while having minimal effect on the EDM side of the process. Increasing conductivity was shown to increase removal of the recast layer with NaCl, as well as exposure time shown through an increase with depth. NaCl produced a pitted surface, therefore the aim was to control electrochemical dissolution mechanisms to

control the resulting surface. $NaHCO_3$ was shown to result in a surface with passive oxides with limited recast layer removal. $NaNO_3$ and $NaNO_2$ produced surfaces with removed recast layers, however with regions of excessive electrochemical pitting and removal. Finally, Na_2SO_4 and Na_2SO_3 produced smooth surfaces with removed recast, with Na_2SO_3 removing the recast through controlled electro-polishing. The change of surface morphology with depth was also least with Na_2SO_3 and largest with $NaNO_3$, showing the difference in surface controllability between electrolytic-dielectrics.

6 Enhanced understanding of Electrolytic-dielectrics by waveform and gas analysis

6.1 Introduction

The balance between EDM and ECM was shown to be crucial in the resulting surfaces, therefore understanding at the discharge scale is needed to control the process and produce tailored surfaces.

This chapter aims to understand the altered surface removal mechanisms due to different salts which alter the balance at the discharge scale, to enable future selection and development of electrolytic-dielectrics. Discharge waveform analysis is thus needed to quantify this balance.

Gas generated is a crucial metric for both EDM and ECM and can give substantial information about gap conditions and removal rates. By linking this to the different electrolytic-dielectrics, machining outputs, and waveform analysis, the process can be further elucidated.

The chapter them aims to propose a simple model to illustrate the overall process balance and zero-recast point by using fundamental electrochemical theory and process pulse data.

6.2 Methodology and Experimental Process

6.2.1 Waveform and pulse analysis

Waveform analysis was conducted to measure the proportion of different types of pulses in machining. Waveform data was measured for 1.2 seconds at three instances for each dielectric, at 3, 20, and 35 seconds after the start of machining, using the set-up showed in Figure 11. Due to the size of the data set (2,000,000 points) and inability to record data continuously, 1.2 seconds were recorded at 166,670 Samples/s of machining at three instances to assess the change in pulse type ratios with machining time and depth.

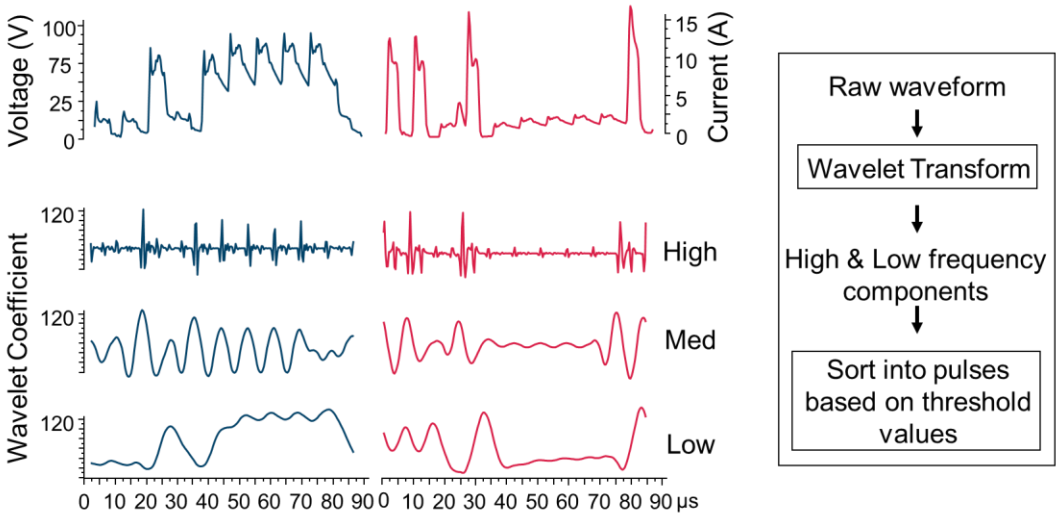

Figure 58. Waveform and pulse analysis. Method of discriminating waveform pulses based on amplitudes of wavelets.

Waveform data was analysed in Matlab. Pulse start and end points were calculated by differentiating the waveform, revealing large changes in voltage and current which relate to pulse start and end times. Pulse discrimination was achieved using the discrete wavelet transform with the Daubechies wavelets, which matches well with EDM waveforms in terms of shape [155] as shown in Figure 58. While the Fourier transform can extract only frequency information, the wavelet transform can extract both temporal and frequency information, revealing localised information from signals. The wavelet transform utilises a wavelet, which is a finite length oscillating wave which starts and ends with zero amplitude, to separate a signal by its frequencies. By compressing a wavelet in the time domain using the scaling factor in the wavelet transform and shifting it across the length of a signal while convoluting it with the waveform (amount of overlap), it is possible to extract the high frequency components [156]. Similarly, by stretching the wavelet and shifting it across a signal it is possible to extract the low frequency components, shown in Figure 58, which shows the high, medium, and low frequency transformed data. By using the amplitude values from the transformed voltage and current waveforms and comparing them against threshold values, it is possible to count and discriminate pulses into different types. Threshold values must be manually chosen by first understanding which types of pulses are present in the raw current and voltage data, and then relating the different types of pulses to the values of the corresponding wavelet transformed pulses by manual sampling. The exact values of the ranges will differ when electrical parameters and experimental equipment are changed. In this way, if the threshold

condition for both the current and voltage is met for a certain pulse type the pulse can be automatically categorised. Different pulse types have discreet thresholds, for example an electrochemical pulse will have a very high voltage and a very low current, while an EDM pulse will have a medium voltage and medium current, and a semi-arc pulse will have a low voltage and high current. By going through each pulse sequentially and comparing to these discrete pulse signatures, pulses can be categorised. The wavelet transform allows this signature to be more easily categorised by essentially simplifying the waveforms to reveal clear pulse signatures.

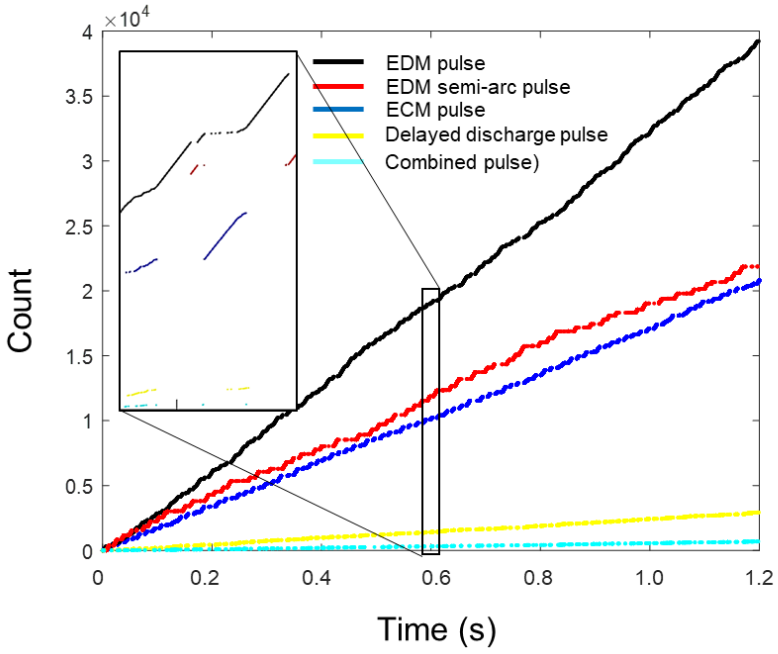

Figure 59. Example of counts for different types of pulses varying with time, done at 3 instances for each hole.

Figure 59 shows the counting of pulses at one of the recording instances. The zoom in shows that when the EDM pulses stop (black line), the ECM pulses begin to rise (blue line). The ratio of pulses was then calculated at 3, 20, and 35 seconds, as well as the overall ratio for all three periods.

High voltage intervals were measured by counting areas of sustained high voltage (ignoring smaller intervals of high voltage due to discharge delay) and comparing to normal machining waveforms.

6.2.2 Process model

To understand the process balance between the electrical-discharge and electrochemical aspects of the process, and the influence of altered dielectrics, a process model was needed. ECM pulse data is needed to simulate electrochemical removal, while EDM process data is needed to simulate hole advance. The theoretical zero recast point can thus be calculated, and with a current efficiency this point can be corrected. Thus, the model can help illustrate the importance of balancing the EDM:ECM pulse ratio to achieve a desired surface.

Current-time values from pulse analysis were used to obtain average charge and pulse data, for electrochemical pulses observed in the process.

Current efficiency was calculated by first machining a hole with DI to produce a generalised EDM surface exhibiting an altered recast layer serving as a baseline for this study. Following this, the dielectric was altered to a 1200 µS/cm sulfite dielectric and the same electrode was lowered into the hole. The same pulse parameters selected previously were used. Electrode advance speed was minimised so that no electrical pulses were observed on the oscilloscope, as the electrode was essentially stationary in the hole. This results in the pulses causing electrochemical machining on the surface of the hole. The amount and charge of pulses were recorded for use in the model.

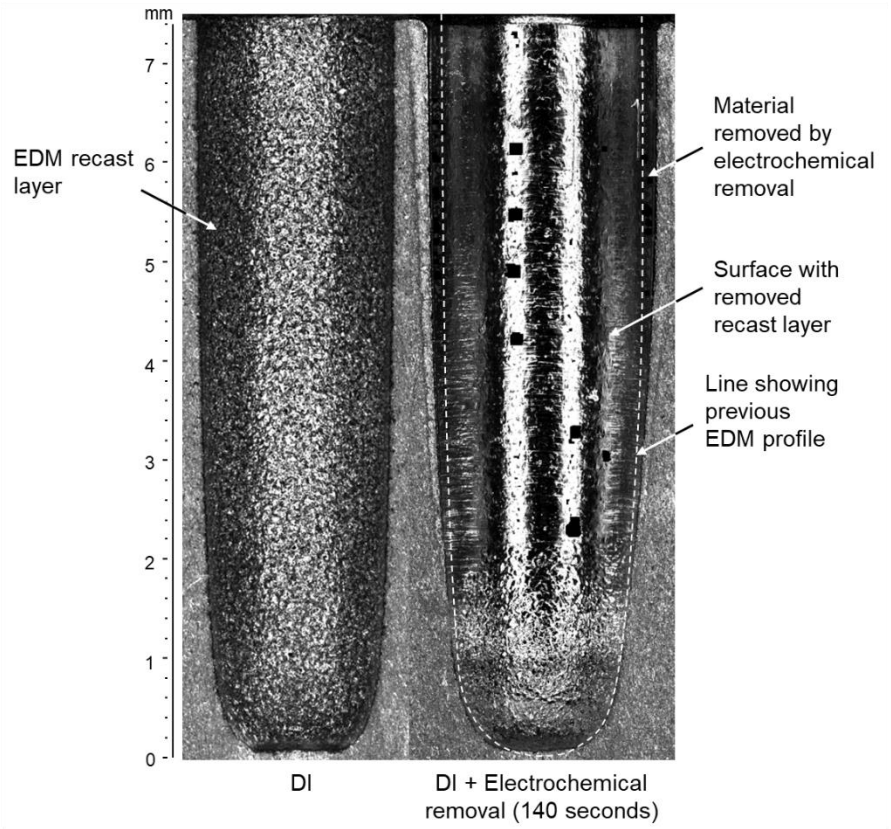

Figure 60. EDM recast layer and resulting surface after 140 seconds of pure electrochemical machining by preventing EDM pulses, showing the electrochemical material removed.

The holes were drilled in the centre of a two-part workpiece clamped together to accurately assess the total material removed. 3D profilometry using the Alicona G4 was used to measure total volumes removed by EDM and electrochemically, on both sides of the holes. This total volume was converted to mass using the density of the material. The material removed was compared to that calculated by Faraday's Law using the total charge measured to calculate the true current efficiency, which was then used in the model.

6.3 Results

6.3.1 Understanding EDM-ECM balance through waveform analysis

To help understand the different chemical interactions and surfaces produced with different salts, DI, NaCl, $NaHCO_3$, and Na_2SO_3 were used to machine holes, at 600 and 1200 µS/cm, due to their discrete removal mechanisms. For each hole, waveforms were captured using the set-up shown in Figure 6, at 3, 20, and 35 seconds after machining.

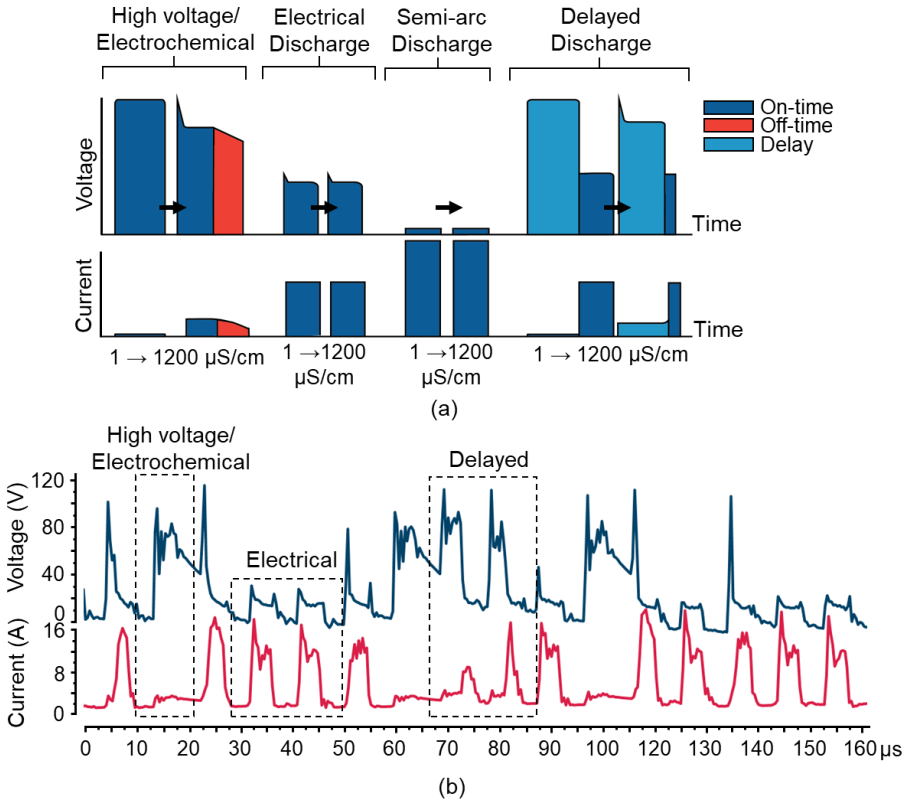

Figure 61. Pulse types found through waveform analysis. a) Showing the different types of current and voltage pulses recorded for DI at 1 µS/cm and Na_2SO_3 at1200S/cm. b) Showing a captured waveform highlighting different pulse types.

Figure 61 illustrates the different distinct pulses recorded on the scale of individual discharges. The high voltage pulse, i.e., where current does not increase to the nominal discharge current, occurs when voltage breakdown cannot occur due to the breakdown strength of the gap not being overcome, owing to gap conditions at the instant of the pulse. In deionised water, this results in a high voltage (near-zero current) pulse. When the conductivity is increased, this high voltage pulse instead causes electrochemical machining to occur, due to the introduced ions. When a high voltage pulse occurs, the voltage drops from open voltage due to the anodic dissolution current flowing. Once the pulse stops the voltage and current slowly decrease, however current still flows in the off-time.

The electrical discharge pulse is identical for both deionised water and high conductivity fluids. In this discharge, high voltage occurs and causes voltage breakdown resulting in current flow. This type of pulse is the same for both conductivities due to the fact that the discharge gap is full of gaseous products and debris which promote discharges, and thus locally the region can be considered dielectric leading to the breakdown limit being similar to deionised water. Thus, the frontal area fluid can be interpreted as acting as a dielectric locally, while the fluid on the side areas acts as an electrolyte.

A semi-arc pulse can occur in situations such as when insufficient debris flushing occurs, fluid dielectric properties are not restored after a pulse, or the discharge gap is too small. This results in high currents flowing. This is also the same for both deionised water and high conductivity liquids due to only occurring in the frontal area.

Finally, a delayed discharge can occur if a pulse struggles to cause a spark resulting in a discharge delay, which then finally sparks after a certain time. In deionised water even if the discharge delay is long, once breakdown occurs the entire pulse duration of a spark still occurs. However, in higher conductivity liquids the initial discharge delay causes electrochemical machining to occur dropping the voltage and increasing the current slightly. The machine however recognises this as a pulse and so when discharge occurs the voltage pulse is stopped prematurely before the entire on-time duration resulting in a combination pulse type. If the discharge delay is larger than the on-time then no spark occurs.

Pulses were sorted into pulse types by comparing the values of the wavelet transformed pulses from the current and voltage waveforms. These values then fit into discrete threshold ranges, which were obtained from sampling waveform data for different pulse types, and thus were used to classify the pulses. For example, the threshold range for electrochemical pulse types is between 0.1 and 10 for the current wavelet transformed pulse (the value is dimensionless as they are wavelet transformed) and between 24 and 100 for the voltage wavelet transformed pulse. For EDM discharges, the threshold ranges are 15 to 45 and 5 to 40, for the current and voltage wavelet transformed pulses, respectively. As each type of pulse has a very distinct signature due to the nature of the pulse voltage and current characteristics, the threshold ranges are discrete and can thus be sorted into certain pulse types.

In the EDM ratio calculation, both normal electrical discharges and semi-arc discharges were counted towards the EDM pulse count, whilst the high

voltage type pulses were counted as the electrochemical pulse. To control the level of electrochemical machining, the amount of high voltage pulses must be controlled as this pulse type is the main contributor to anodic dissolution.

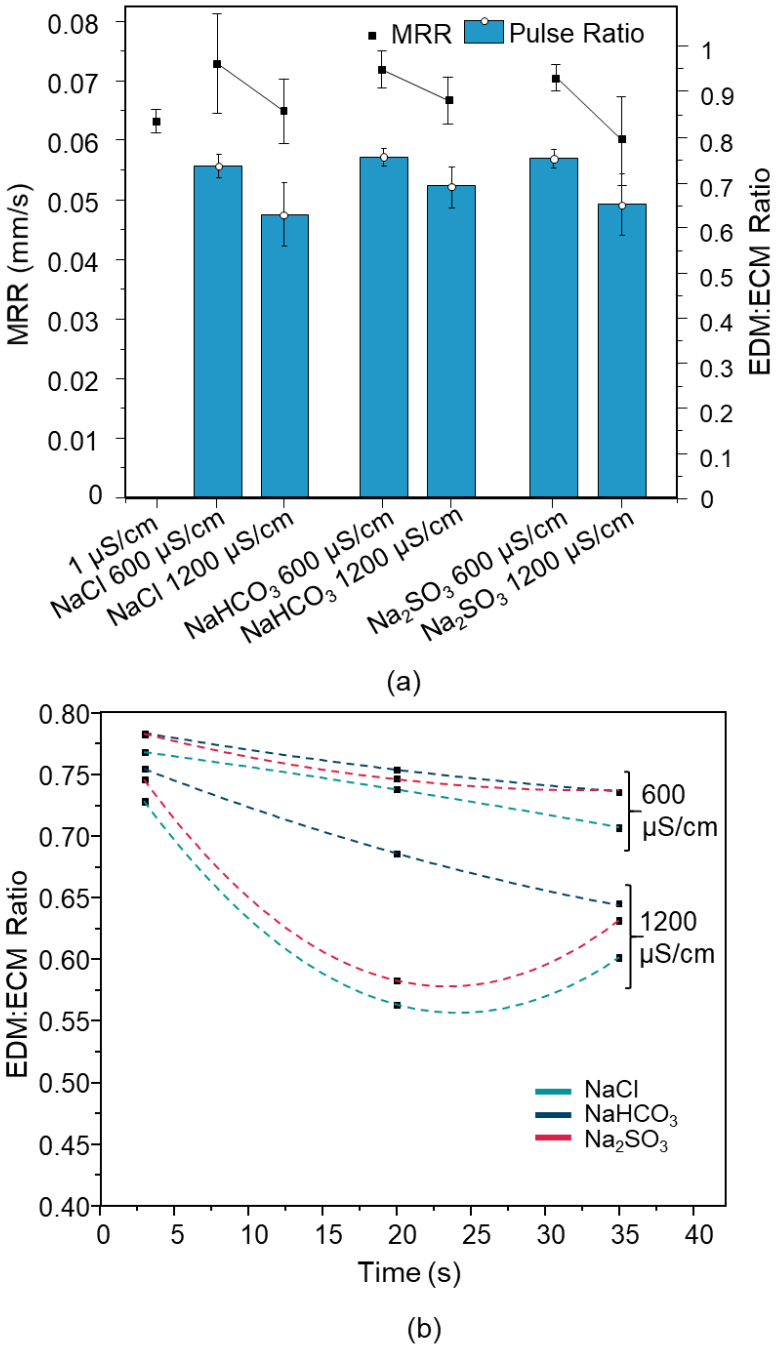

Figure 62. Pulse balance. a) MRR and average EDM ratio from all recorded for each additive. MRR and pulse ratio error bars represent ± SD from mean n = 3. b) Change in EDM to ECM pulse ratios recorded at 3, 20, and 35 seconds from start of machining for NaCl, $NaHCO_3$, Na_2SO_3 at 600 and 1200 µS/cm conductivity.

Figure 62a shows that at 600 µS/cm, the EDM pulse ratio (EDM pulse count compared to the ECM pulse count), is 76%, 76%, and 74%, and at 1200 µS/cm 65%, 70%, and 63%, for Na_2SO_3, $NaHCO_3$, and NaCl respectively. At 600 µS/cm, NaCl has the most ECM pulses. Although the difference at 600 µS/cm is not large due to the low conductivity, at 1200 µS/cm the magnitude of difference is larger and NaCl has the most ECM pulses whilst $NaHCO_3$ has the most EDM discharges. The increase in conductivity thus increases ECM pulse count. As expected, the decrease in EDM discharges is also accompanied by a decrease in MRR.

Figure 62b shows that after 3 seconds EDM discharges dominate machining. At 20 seconds at 1200 µS/cm ECM pulses increase due to the increased ECM area, whilst for $NaHCO_3$ the decrease is less. At 35 seconds for both NaCl and Na_2SO_3 EDM pulses increase. Compared to 1200 µS/cm, at 600 µS/cm there are considerably more EDM discharges, and the increase in ECM pulses is less steep indicating limited anodic dissolution due to reduced ions for anodic dissolution.

To further explore the differences in pulses between dielectric solutions, the charges were analysed for electrochemical pulses using the waveform pulse data for electrochemical pulses. The average electrochemical pulse charge was similar between the sulfite, chloride, and bicarbonate anion solutions, of 7.62, 7.67, and 7.53 x 10^{-5} C, at 1200 µS/cm respectively, and 7.46, 7.52, and 7.32 x 10^{-5} C at 600 µS/cm respectively. Chloride has a slightly higher charge, and bicarbonate the lowest, with an increase in charge with an increase in conductivity. The average charge transferred during electrochemical pulses was shown to increase with time, from 6.56 x 10^{-5} C to 9.56 x 10^{-5} C. A

decrease in solution conductivity from 1200 µS/cm to 600 µS/cm resulted in only a slight decrease in electrochemical pulse charge of ~2%.

Figure 63 shows the roughness of the surfaces produced. The Sa parameter was used as a general comparison between electrolytic-dielectrics. Although peak to peak may be more relevant for NaCl due to pits, the Alicona focus variation instrument cannot obtain data of pit depths at the magnification and size needed. It is shown that NaCl is significantly smoother than the other electrolytic-dielectrics, followed by Na_2SO_3 and $NaHCO_3$. Only Na_2SO_3 shows a decrease in roughness with an increase in conductivity.

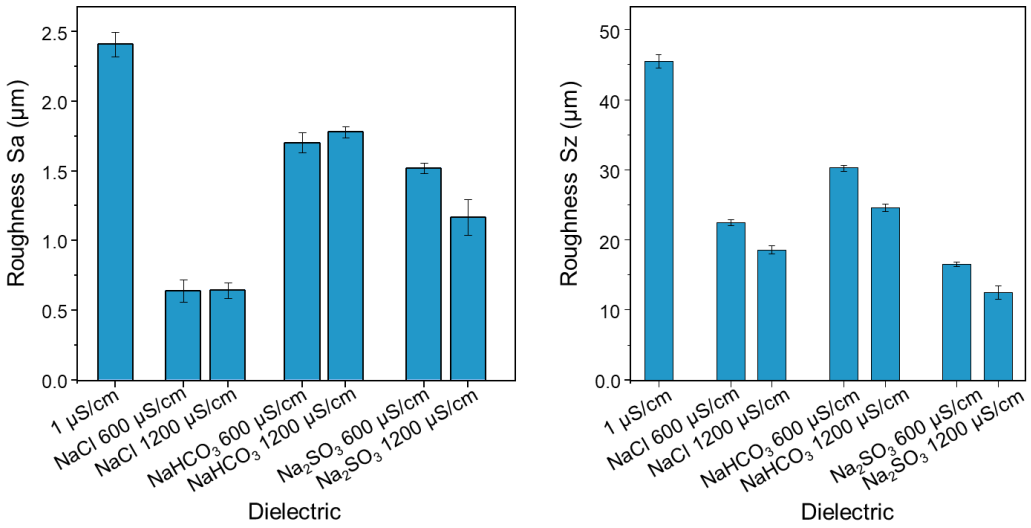

Figure 63. Roughness Sz and Sa parameters of hole surfaces with different electrolytic-dielectrics at 600 and 1200 µS/cm conductivity. Error bars represent ± SD from mean n = 3.

To confirm whether gap conditions were crucial to the process, the percentage of high voltage intervals were measured for each electrolytic-dielectric, for the two conductivity levels. As shown in Figure 64, NaCl showed the highest percentage of high voltage intervals; while $NaHCO_3$ showed the

least out of the electrolytic-dielectrics (DI is most stable). The difference is small at 600 µS/cm however is clearer at 1200 µS/cm.

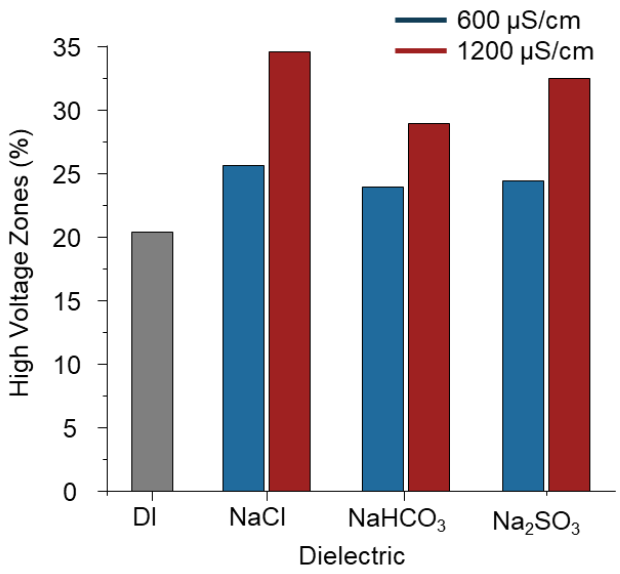

Figure 64. Change in instability percentage for different electrolytic-dielectrics at 600 and 1200 µS/cm conductivity .

As shown in Figure 65, at 600 µS/cm, the high voltage intervals increase with depth. At 600 µS/cm the change is linear for the electrolytic-dielectrics, however DI increases significantly after 20 s. With an increase in conductivity the relationship can be seen more clearly. Both NaCl and Na_2SO_3 show a larger increase in high voltage intervals. From 20 to 25 seconds, they also show a slight decrease in high voltage intervals, while $NaHCO_3$ remains linear as compared to 600 µS/cm.

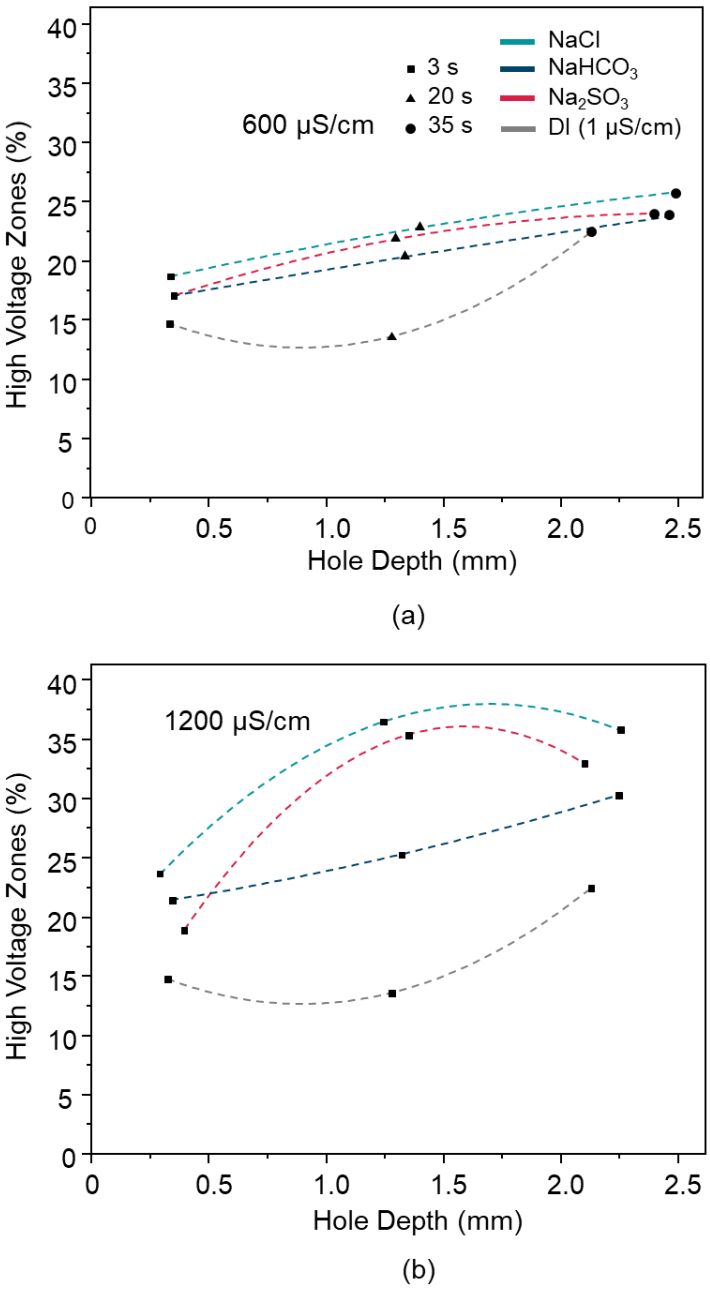

Figure 65. Percentage of Instability regions for each electrolytic-dielectric, plotted against current machined depth at three time intervals. a) At 600 µS/cm. b) At 1200 µS/cm.

6.3.2 Electrolytic-Dielectric Gas Analysis

Gas was collected for the holes machined in Chapter 5.2.1 using NaCl at increasing conductivities and the total volume was measured using the eudiometer tube. A gas volume generated per second was calculated using

the total machined time of the hole. From Figure 66, the rate of gas generation per second was shown to increase from around 215 ml/s to 260 ml/s, with a final volume from 13ml to 16ml between 1 and 1000µS/cm, possibly due to increased anodic dissolution. The trend was shown to level off towards 1000 µS/cm. EDM MRR was shown to be minimally affected (and therefore likely EDM ratio) by the increase in conductivity, with the MRR beginning to trend downwards approaching 1000 µS/cm. The increase in gasses, especially around the EDM zone, is the likely explanation why the MRR was not considerably affected, where electrical discharges were maintained due to the decreased dielectric strength and discharges caused by debris accumulation at bubble interfaces, promoting sparks and secondary discharges.

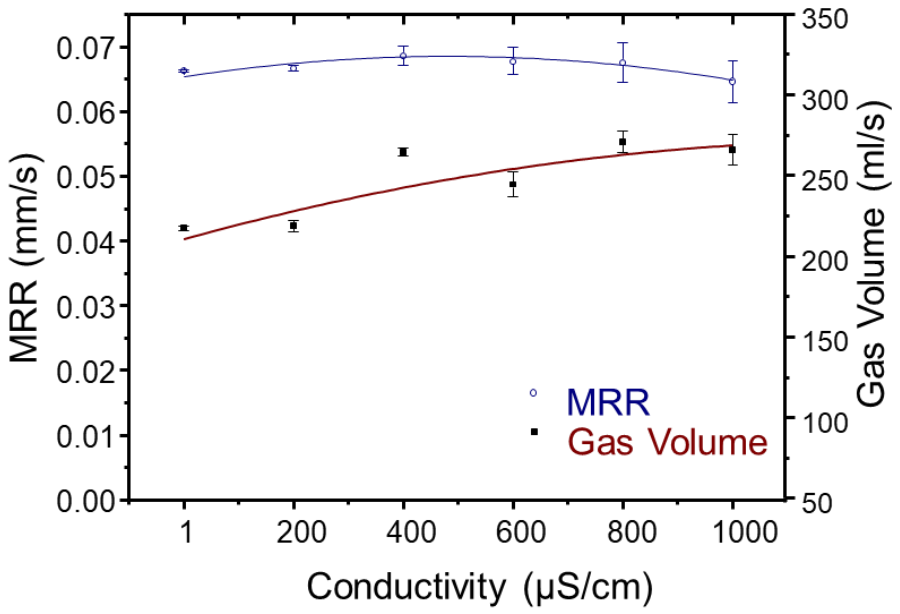

Figure 66. Change in MRR and generated gas volume with conductivity using NaCl additive. MRR and gas error bars represent ± SD from mean n = 3.

Gas was similarly collected for the holes machined in Chapter 6.3.1 using sodium sulfite, sodium bicarbonate, sodium chloride, and DI, as shown in Figure 67. Between electrolytic-dielectrics, gas generation was shown to

decrease with an increase in conductivity which was accompanied by a decrease in the EDM MRR, similar to the previous results with NaCl at varying conductivities. Gas generation was similar between DI and Na_2SO_3 at 600 µS/cm, with a decrease at 1200 µS/cm. $NaHCHO_3$ and NaCl have a similar gas generation rate, both significantly higher than DI or Na_2SO_3. In all cases the decrease in gas is accompanied by a decrease in the EDM MRR.

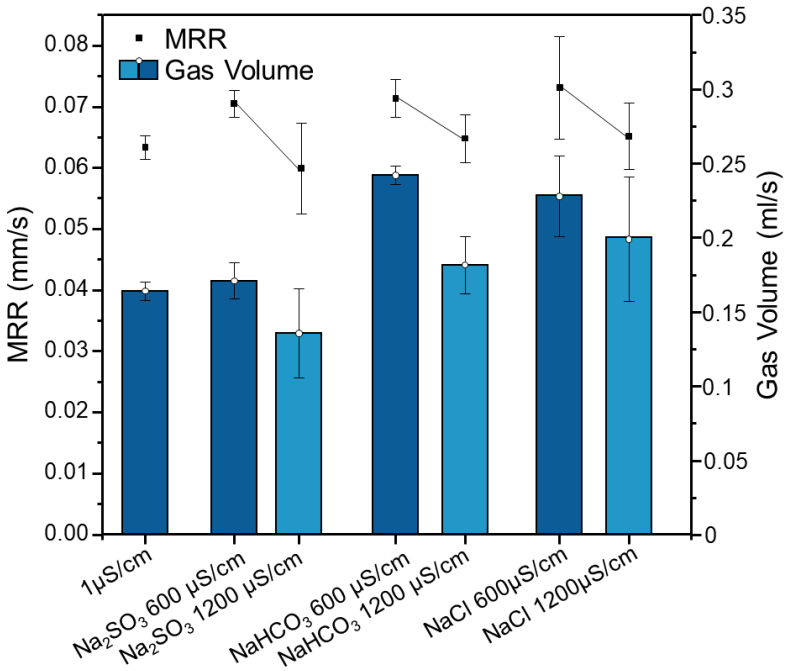

Figure 67. Change in MRR and generated gas volume with conductivity using various electrolytic-dielectrics. MRR and gas error bars represent ± SD from mean n = 3.

Figure 68 shows the results of the gas collection and detection of gas analysis via video analysis. This data was collected to observe any change of gases generated with different electrolytic-dielectrics. It can be seen that for most of the hole depth Na_2SO_3 generates less gas compared to DI, and also compared to the other electrolytic-dielectrics. $NaHCO_3$ is shown to produce the most gas out of all holes at 600 µS/cm, with NaCl with a similar curve. This is followed by NaCl at 1200 µS/cm and then $NaHCO_3$ at 1200 µS/cm. DI is

shown to have a near-linear (a slight increase with time) increase in gas generation throughout. For Na_2SO_3 at 600 µS/cm gas rate is linear until around 25 - 30 seconds, and then increases. This is also seen at 1200 µS/cm however the change in gas rate is less pronounced. At 600 µS/cm $NaHCO_3$ has a linear gas rate until 25 seconds, and then a slight increase is seen. At 1200 µS/cm gas rate behaves similarly with an increase in gas rate at 25 seconds. NaCl also shows an increase in gas rate from 27 seconds. However, in this case at 1200 µS/cm the gas rate increase is smaller than that at 600 µS/cm.

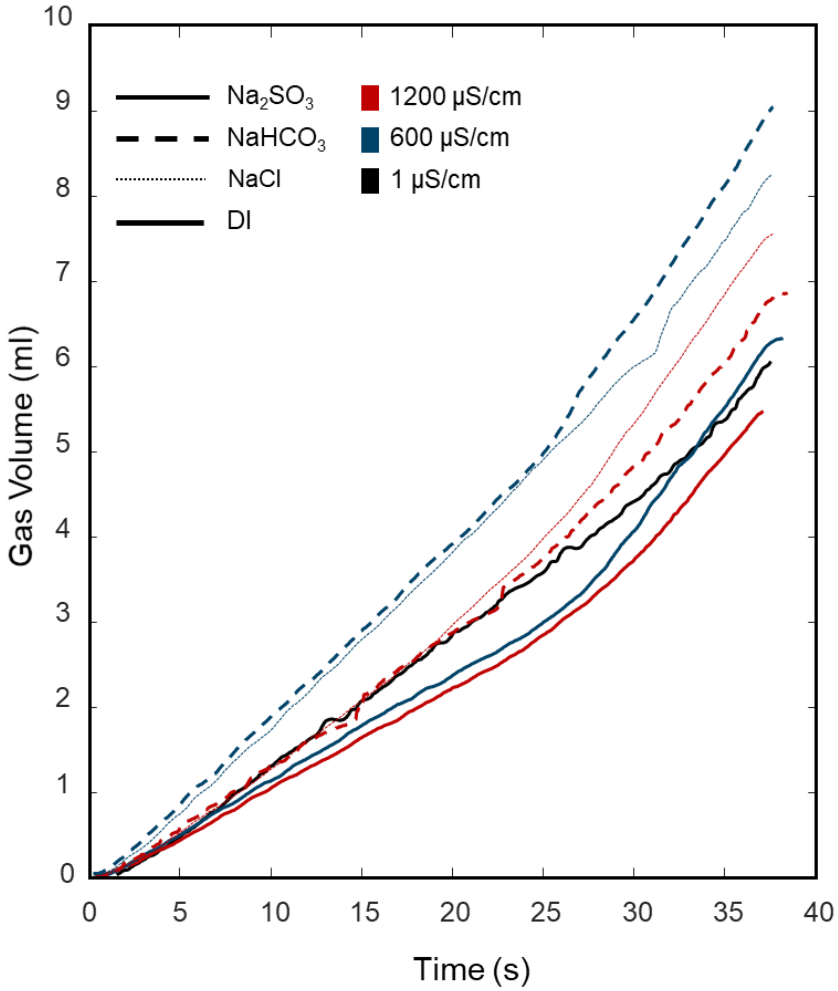

Figure 68. Gas volume showing changes in gas rate for all electrolytic-dielectrics compared to DI, at 600 and 1200 µS/cm. Each curve is an average of curves at each time point (n=3).

To understand why the gas volume changes with time, the relation with depth, conductivity, and electrolytic-dielectrics was shown in Figure 69. Figure 69 shows the relationship between the gas volume generated and hole depth at 600 µS/cm, while Figure 70 shows it at 1200 µS/cm. It was shown that for DI that there is a linear relationship between current hole depth and gas volume generated. For Na_2SO_3 the increase in gas volume trend is reflected in the change in hold depth. When the rate of depth advancement increases, the rate of gas generation also does, linking to the increase in electrical discharges. This is also shown at 1200 µS/cm in Figure 70 and similarly for the other electrolytic-dielectrics. The differences between electrolytes will be discussed in Section 6.4.1.

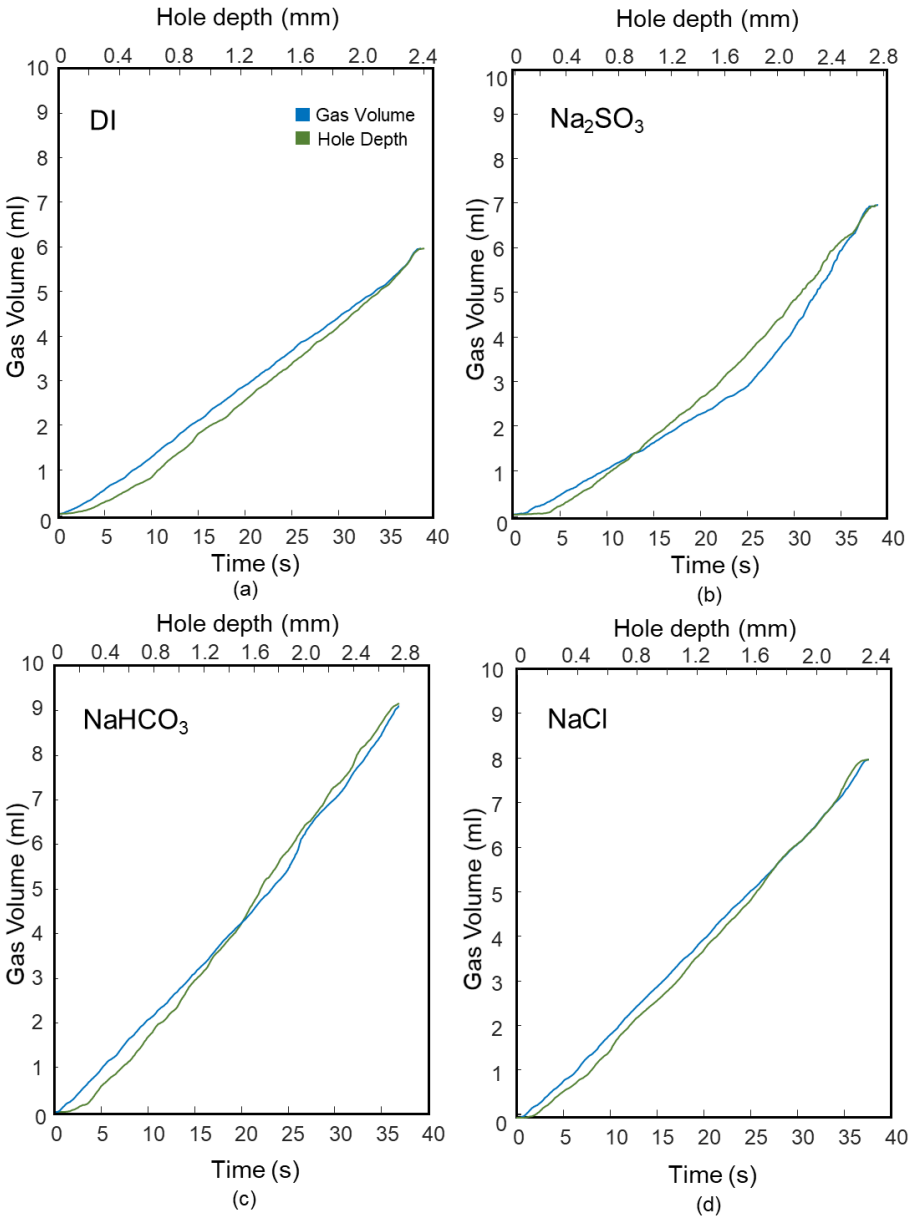

Figure 69. Comparison of change in gas volume with time and change in gas volume with hole depth at 600 µS/cm.

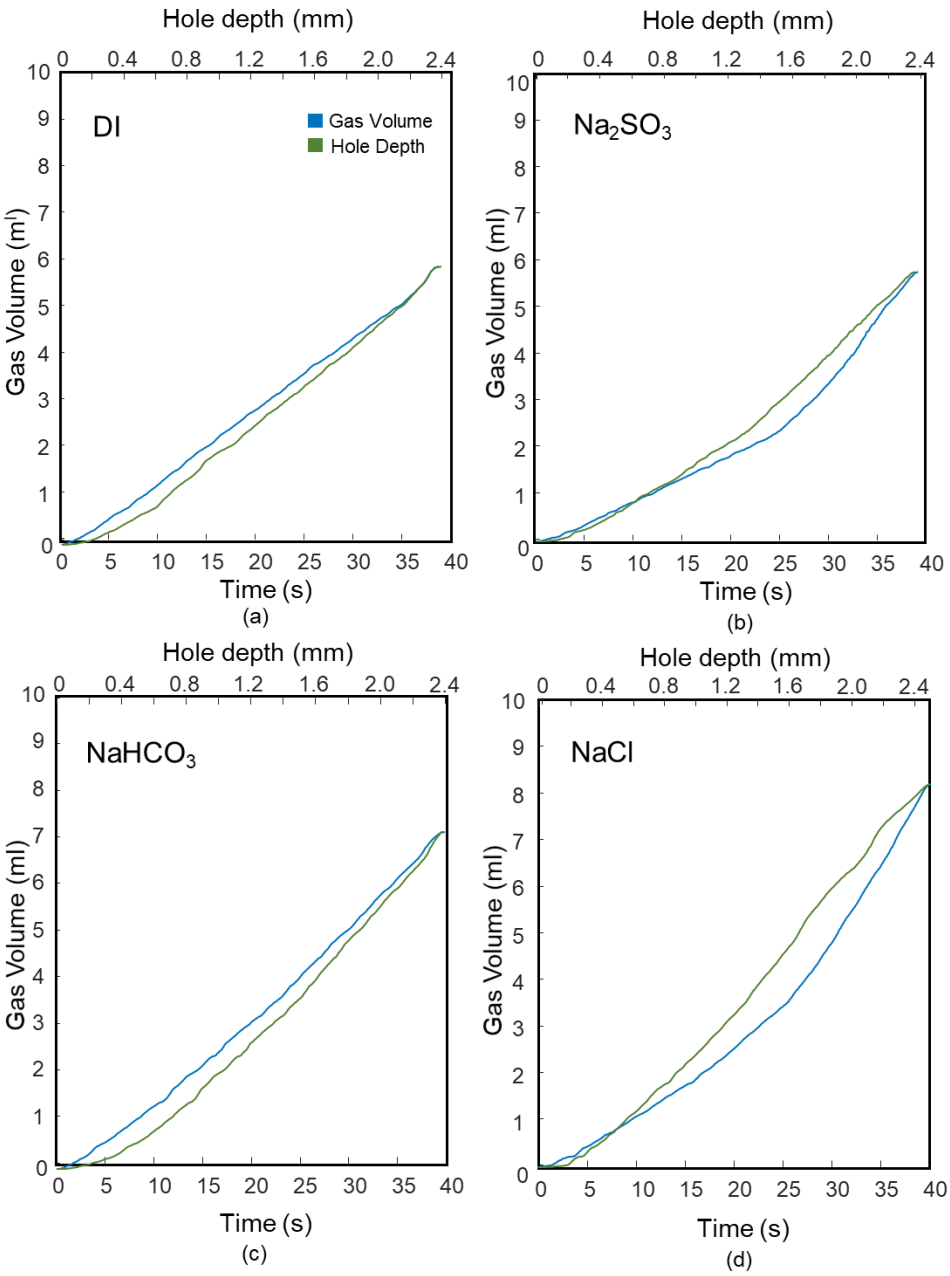

Figure 70. Comparison of change in gas volume with time and change in gas volume with hole depth at 1200 µS/cm.

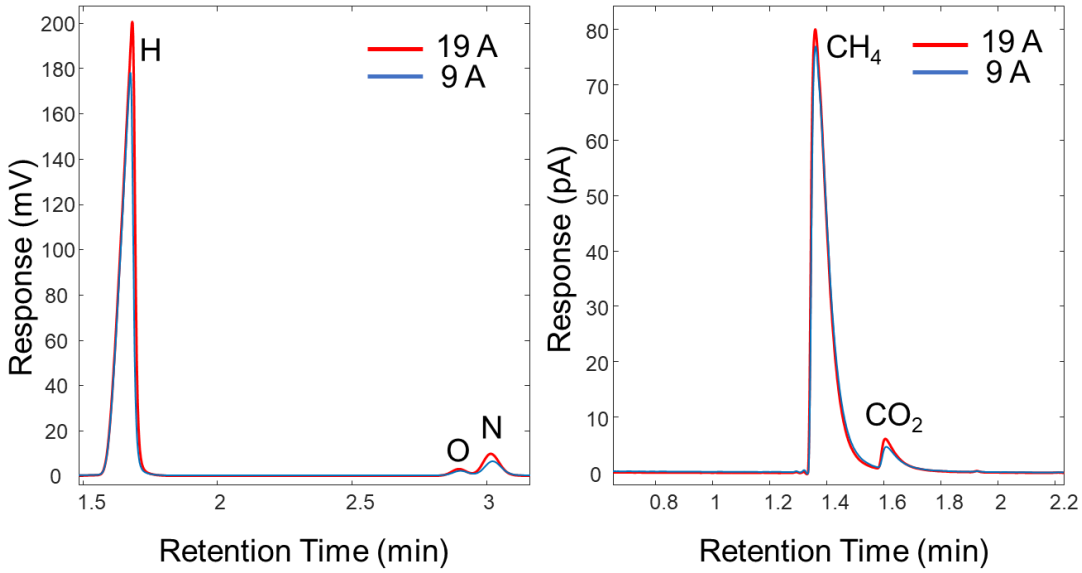

Figure 71. Gas Chromatography results showing gas composition, left using TCD detector, and right using the FID detector.

To further understand gases generated the bubbles were analysed using gas chromatography. H, O, N, CO_2, and CH_4 were found. Two currents were tested to see the effect on gases. From Figure 71 it can be seen that an increase in current alters the gas proportion. The change in proportion cannot be analysed as the current machine used was not capable of gas proportion analysis. Gas chromatography can be a good method to understand differences in chemical mechanisms between electrolytic-dielectrics, and EDM parameters, and should be explored further.

6.4 Discussion

6.4.1 Understanding the EDM-ECM balance

Through capturing waveforms, it was shown that distinct pulse types are present. The most important pulse type in this process is the high voltage/electrochemical pulse as this is the pulse that drives electrochemical dissolution of the EDM recast layer. This pulse type occurs in regions where a high voltage is observed. Though in DI this high voltage causes near-zero current to flow, when conductivity is increased, by addition of ions, a current can flow in both the on and off-time causing electrochemical machining. The current flow in the off-time can be explained due to the capacitance in the system. The capacitance is likely caused by the charging of the electric double layer. The electric double layer is formed when the charged anode attracts oppositely charged ions forming two layers, one of which is the compact oppositely charged layer and the other is the diffuse layer in which the concentration decreases further from the anode surface. In the on-time this capacitive layer is charged and subsequently discharged in the off-time [102]. Therefore, the regions of high voltage are crucial in controlling the dissolution process.

These high voltage intervals normally occur when dielectric breakdown cannot occur due to a large IEG [157]. This may be at the instance when the electrode is advancing towards the workpiece to initiate voltage breakdown, when enough material is removed that the gap is too large, or when the electrode is retracted due to unfavourable gap conditions (as in leading to arcing or short circuits). High voltage intervals can also occur as discharge

delay regions, which occur at the start of delayed pulses. These delayed regions occur also due to too large IEGs, but can also be significantly affected by factors that can alter the local dielectric strength such as fluid dielectric constant, open voltage, gas volume, temperature, electrode workpiece geometry, and contaminants/debris.

Through waveform analysis, it was observed that the majority of the electrochemical pulses were grouped together in packets, with a small number interspaced between electrical discharge or semi-arc pulses (< 1 %). Discharge delayed pulses, which have a portion of electrochemical machining at the start of the pulse, only accounted for 1 % to 2.5 % of pulses. Therefore, it can be assumed that the main driver of electrochemical removal are the pulses which occur in large packets. These regions can be inferred to correlate to the instances of electrode halt or retraction due to gap conditions (inability to cause breakdown). In this case, the pulse energy due to the high voltage causes electrochemical dissolution as opposed to an electrical discharge. Whether the energy causes ECM or EDM therefore depends on gap conditions and is the basis for the need to control pulse ratio.

The EDM zone, as shown in Figure 50, is the zone where EDM discharges occur. Due to the smaller IEG and increased gas and debris in the region, this zone locally acts as a dielectric causing electrical breakdown. This explains why EDM discharges are identical between conductivities. However, in regions of high voltage no breakdown occurs thus the region acts as an electrolyte. The balance between EDM and ECM discharges therefore is heavily influenced by gap conditions, which are affected by EDM parameters

as well as dielectric and salt additives. By controlling the amount of EDM pulses the dissolution of the recast layer can also be controlled.

The influence of gap conditions on the process was shown in Figure 64 and Figure 65. NaCl showed the most high voltage intervals, followed by Na_2SO_3, $NaHCO_3$, and DI, with the difference being more clear at 1200 µS/cm. The increase in conductivity was shown to increase the high voltage intervals for all electrolytic-dielectrics, showing that the cause of the high voltage intervals and instability is electrochemical machining. This may be due to the increased anions, which cause a charge to be transferred and thus hinders electrical discharges. This can also be explained by the electrochemical charge causing the EDM gap to increase due to flowing current, therefore increasing machining voltage and also increasing likelihood of high voltage intervals due to the enlarged gap. If the current flow or charge being stored is too large it can also reduce electrode advance due to essentially tricking the EDM pulse controller into thinking that a discharge is happening due to detected current and voltage values. NaCl shows the largest high voltage interval percentage, which implies the electrochemical machining it causes has the largest effect on the gap. This is confirmed by the waveform pulse analysis which showed that pulse charge for NaCl was the largest, followed by Na_2SO_3, and $NaHCO_3$.

The increase in high voltage intervals and instability was also shown to increase with the depth of the hole, this can generally be explained by the increase in debris and bubbles, which causing debris bridges, arcing, and promotes unstable sparking resulting in electrode retraction. This is also explored in the pulse type analysis and shows that the EDM semi-arc discharge type was counted as 26,000 at 3 seconds, 27,000 at 20 seconds,

and 28,000 at 35 seconds. However, the EDM arc pulses did not increase for the electrolytic-dielectrics, conversely they were shown to decrease with time, which suggest that the higher instability for the electrolytic-dielectrics is caused by electrochemical factors (enlargement of the gap due to electrochemical current flow). For example, at 1200 µS/cm the EDM semi-arc pulse counts were, ~21000, 10000, 12000 for Na_2SO_3, at 3, 20, and 35 seconds. $NaHCO_3$ showed 28,000, 16,000, 17,000, and NaCl showed 26,000, 11,000, and 14,000. $NaHCO_3$ showed the most semi-arc discharges compared to the other electrolytic-dielectrics, explained by the reduced electrochemical machining. Figure 65 then shows that, although at 600 µS/cm the electrolytic dielectrics all increase in high voltage intervals linearly with depth, at 1200 µS/cm only $NaHCO_3$ remains a linear increase while NaCl and Na_2SO_3 increase sharply then decrease. For $NaHCO_3$ the increase in conductivity shifted the curve up slightly, with no change in trend implying that the increase in anions for charge transfer slightly increases the high voltage intervals. $NaHCO_3$ has likely a small change with conductivity (and depth) due to the limited electrochemical removal as compared to the other salts. For the other electrolytic-dielectrics the change is larger, and shows a sharp increase which tapers off. In this case, electrochemical machining is more pronounced due to the removal mechanisms as discussed previously, resulting in a large increase in these zones. With depth the average electrochemical pulse charge increased from 6.56×10^{-5} C to 9.56×10^{-5} C, possibly due to the increased ions, area, stored charge, or conductivity, which subsequently results in the increase in high voltage intervals. As both NaCl and NA_2SO_3 have increased electrochemical

machining compared to $NaHCO_3$, this increase in charge has a larger effect on high voltage intervals.

Each salt additive is likely to also cause different gap conditions in both the ECM and EDM zones, such as different volumes of gas, altered surfaces which can affect discharges, and different types of debris (ECM oxide spalling and size of debris or sludge due to dissolution), which would then result in different amounts of high voltage intervals.

The effect of these high voltage intervals can be seen in the waveform pulse analysis which categorises each individual pulse into types. NaCl has the most ECM pulses, with $NaHCO_3$ has the least. The EDM pulse ratio also decreases with time and depth, resulting in increased electrochemical pulses and decreased electrical discharges, linking an increase in high voltage intervals with increased electrochemical pulses. The pulse ratio results are reflected in the high voltage intervals trends, showing that both are directly linked. The increase in high voltage intervals thus results in more ECM pulse types and a reduction in EDM pulses. Therefore, the percentage of high voltage intervals is a more efficient way to measure and control the balance between the EDM and ECM sides of the process. The results also confirmed that the electrochemical pulses scattered throughout machining can be essentially ignored, in favour of the electrochemical pulses in the instability regions of high voltage. Thus, this is a better measure for EDM ECM balance and a method to control anodic dissolution of the recast layer.

The EDM MRR should be proportional to the amount of EDM discharges. This should result in the order of MRR from highest to lowest being $NaHCO_3$,

Na_2SO_3, and NaCl, due to changes in pulse ratio. However, NaCl has similar MRR to $NaHCO_3$, and significantly higher than Na_2SO_3 at a similar pulse ratio.

One way we can understand this is through gas analysis. In Figure 67 it is shown that for all additives gas generation decreases when conductivity is increased, while the MRR also decreases. This may be due to the decrease in EDM discharges, which generate more gas than anodic dissolution, while also driving the bulk material removal. To confirm whether EDM discharges are the main driver of gas volume increase, Figure 69 and Figure 70 were plotted using the change in gas volume data obtained from the video recording of the gas eudiometer tube and the change in hole depth, which was produced from the change in machining depth and the wear. It was shown that the change in hole depth is reflected in the change in gas volume with time. At the instance that hole advance increases, the gas generation increases, thus confirming the differences in gas generation in different electrolytic-dielectrics related to the amount of EDM pulses (compared to ECM pulses). For DI, gas accumulation is linear however for the other additives gas generation increases with time (and depth) and is more pronounced for lower conductivities. This can be explained by the increase in EDM pulses with time, shown as the increase in gradient from 20 to 35 seconds in Figure 62. An increase in gas generation can also result in changes in the conductivity and current density for electrochemical removal. This can reduce anodic dissolution; however, it is not possible to directly relate this to results because an increase in gas generation is also followed by an increase in electrical discharges and reduction in electrochemical pulses. Therefore, if there is a reduction it will be obfuscated, however a decrease is expected [158-160].

NaCl was shown to have larger gas generation than the other electrolytic-dielectrics. This should imply that NaCl has more EDM pulses, however this was not the case. Therefore, a significant proportion of this extra gas generated must be from electrochemical machining. The larger spark gap also results in larger gas bubble diameters, likely due to increased energy used in bubble generation instead of metal removal, which was also shown to increase impulse force [45] and vapour jet force [36]. The combination of increased bubbles, increased heat released, and increased molten material removal may have increased the MRR using NaCl.

Na_2SO_3 produces the lowest gas volume, while NaCl and $NaHCO_3$ produce significantly more. Considering the small difference in EDM pulse ratio in comparison to the larger difference in volume generated for Na_2SO_3, compared to the other additives, it can be assumed that more of the energy is going into material removal rather than formation of an oxide layer and generation of gases. SO_3^{2-} is also an oxygen scavenger which removes dissolved oxygen from the solution by oxidizing to SO_4^{2-} [144]. A decrease in oxygen content would also decrease the acidification of the zone thus reducing the rate of anodic dissolution.

To summarise the relationships, comparing Figure 70 (change in gas with time and depth) to Figure 62 (change in EDM pulse ratio), it can be seen that the increase in hole depth rate (MRR) and resulting gas generation after 20 seconds is linked to the sharp increase in EDM pulse ratio for Na_2SO_3 and NaCl. $NaHCO_3$ is mostly linear in gas and depth rate, which is reflected in the pulse ratio plot showing no deviation from the trend. This can then be linked back to Figure 65 where the high voltage intervals level off for Na_2SO_3 and

NaCl, while they do not for DI and $NaHCO_3$, which is the cause of the increased pulse ratio. The increased high voltage intervals (compared to DI) are initially caused by a combination of the charge and current due to electrochemical machining (inhibiting sparking) which differ in different electrolytic-dielectrics. The differences in gases, charge, current density, surface types, and ECM removed material then interact with each other in the IEG and can affect the high voltage intervals.

In general, due to the points mentioned above when a pulse begins the energy can either be used in formation of an electrical discharge or in the anodic dissolution of the workpiece. This depends on gap conditions, mainly the size of the gap and likelihood of electrical discharges. If the conductivity is too high, or if an aggressive (non-passivating) salt like NaCl is used, there will be too much current and charge due to anodic dissolution (which also occurs in the off-time) thereby shifting the likelihood towards electrochemical machining.

6.4.4 Zero-recast point prediction

In order to model the process it was assumed that the direct interactions between electrical discharges and electrochemical machining were negligible i.e. electrical discharges are solely used to advance hole depth and create the EDM overcut, while electrochemical discharges are solely used to remove material from the recast layer (normal to the direction of hole advance). The EDM material removal can be modelled by using the MRR from machining with DI, while the electrochemical material removal can be modelled by Faradays Law in Equation (5).

$$m = \frac{1}{F}\left(\frac{M}{v}\right)\int_{t_0}^{t_f} I\,dt = ZQ \qquad (5)$$

m is the mass removed by electrochemical removal, F is Faradays number, M is molar mass, v is ion valency, I is current, and t_0 and t_f are the time limits over which the current time integral is taken. The equation can be simplified further where Z is the electrochemical equivalent of the material shown in Table 4, and Q is the charge passed.

The recast layer/workpiece depth removed can then be calculated by Equation (6) which converts the mass to a volume removed from the sidewalls, and then to a recast depth removed. Y is the recast depth removed, h is the depth over which the volume is removed, ρ is the density of the metal, and D_1 is the total diameter of the electrode and EDM overcut.

$$y = \frac{1}{2}\left(\sqrt{\frac{4m}{\pi h\rho} + {D_1}^2} - D_1\right) \qquad (6)$$

Figure 72 shows that after one time step, two volumes of material are removed. The EDM removed material depends on the MRR and is the area through which the electrode and spark gap/overcut removes material through the workpiece, in one time step. At the same time the electrochemically removed material, calculated by Equation (1), is removed from the recast layer. The amount of electrochemically removed material is calculated using the current-time values obtained previously in which pulse analysis was used to obtain average charge and pulses per second data, for electrochemical

pulses observed in the process. After each step the area increases, however the ECM removed material per pulse remains the same resulting in the removal over a larger area. This concentrates the removal in areas which are machined for more time.

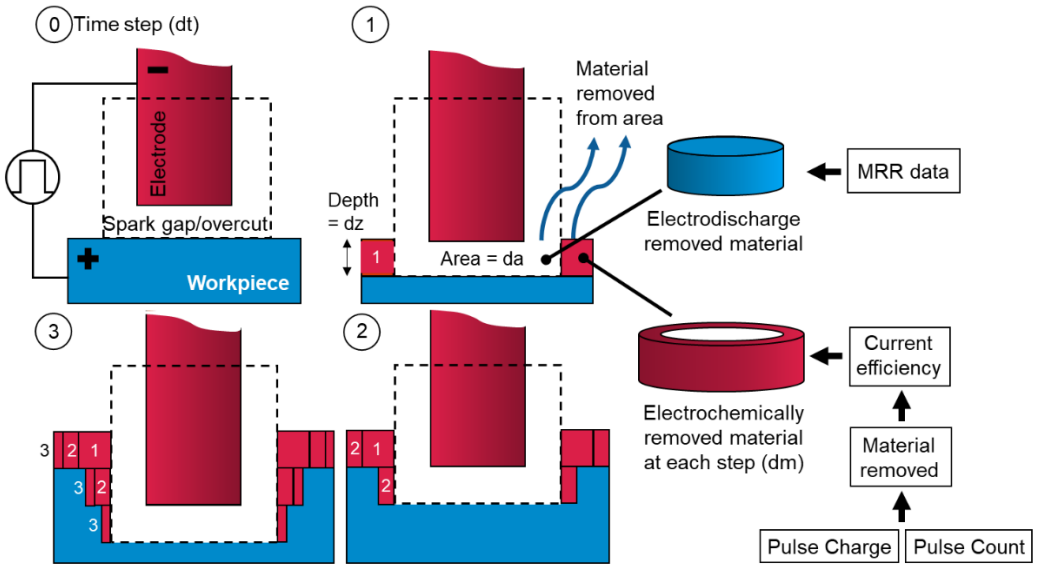

Figure 72. Process model explanation. Showing 4 time steps and resulting material removal.

While Equation (1) calculates the material removed due to electrochemical machining, it does not account for the energy not used to remove material, such as in the generation of gas, oxides, and heat loss [161]. To account for this a current efficiency is needed to correct the calculated mass removed, which was calculated by drilling a hole with DI producing an EDM recast layer, then machining this with pure electrochemical machining with the same process conditions and equipment used in this paper.

The current efficiency was estimated as 15.2 % using sulfite, and Figure 73 shows the results of the model. Figure 73a shows the change in charge per area as the hole advances. The area increases as depth advances which

reduces the amount of charge on an individual area, resulting in the expected hole geometry. Figure 73b shows the amount of recast depth removed and essentially shows the resulting hole profile. The current efficiency has a large influence on the resulting profile; however, it is a more accurate representation of real machining.

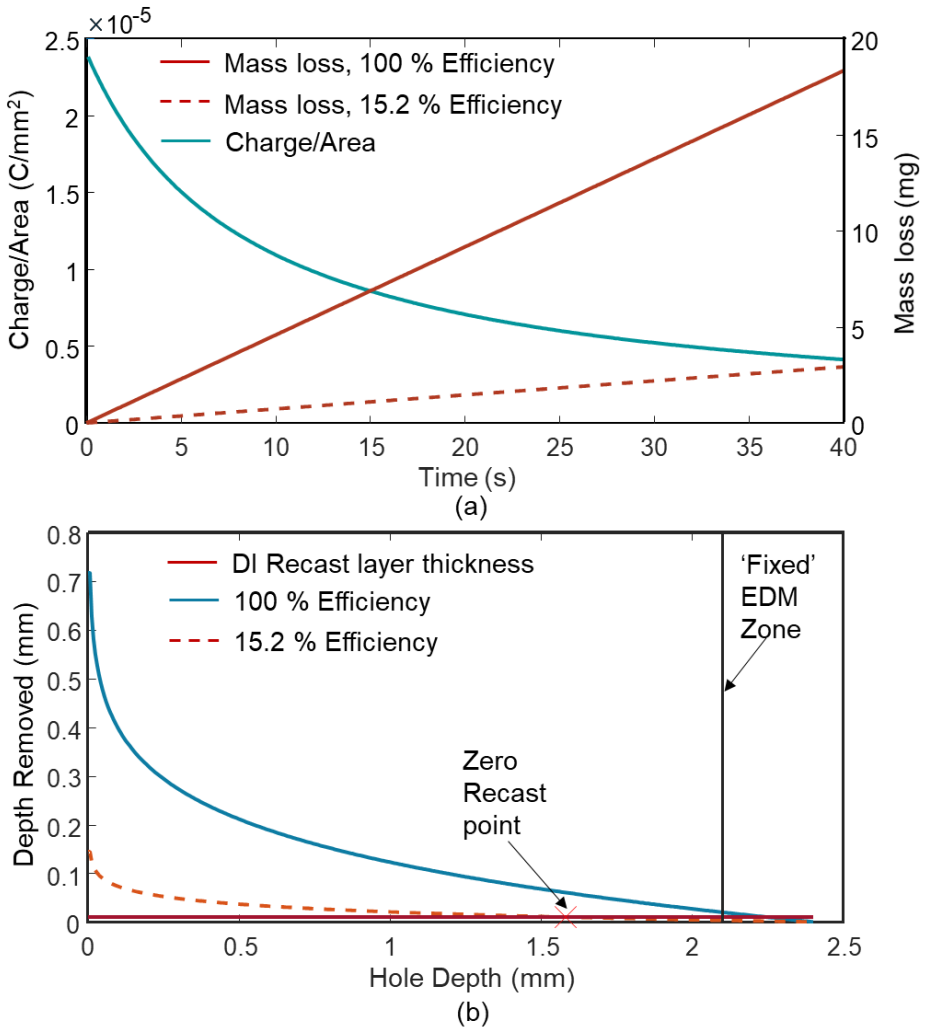

Figure 73. Results of model. a) Change in Charge per Area and mass loss with time, at 1200 µS/cm. b) Amount of recast depth removed with depth, showing the zero recast point, fixed EDM zone, and affect of current efficiency on the model.

One factor not considered in the model was the influence of gap distance on gap resistance and the influence on electrochemical machining. Although from Figure 73b it shows considerably more material is removed between 0

and 0.5 mm compared to 0.5 mm to the end, in a real example this difference is less pronounced due to reduced material removal at areas of increased gap distance. This relationship can be described by Equation (7) in which an increase in gap distance increases resistance along the path, where R is the resistance, V is the voltage, I is the current, y is the gap, A is the area, and k is the conductivity. This resistance ultimately reduces electrochemical material removal at areas of high resistance. Although the total material removed will be the same, the distribution will differ. The end result of this will be that the predicted zero-recast point will be further down the hole.

$$R = \frac{V}{I} = \frac{y}{Ak} \tag{7}$$

Figure 73b also shows a fixed EDM discharge zone. This zone is entirely influenced by the electrode corner wear. Although in this model no electrode wear was assumed, in reality corner wear will occur. This will result in a fixed EDM zone that is equal to the sum of the corner radius and spark gap, as this region is the area that, in addition to the frontal area, advances towards the workpiece material to initiate electrical discharges.

Figure 74 shows the results of the model for Na_2SO_3 at the two conductivity levels. With an increase in conductivity the material removed increases, while the zero recast point also shifts further down the hole resulting in a larger zero recast surface. The final hole depth was achieved using to the MRR data.

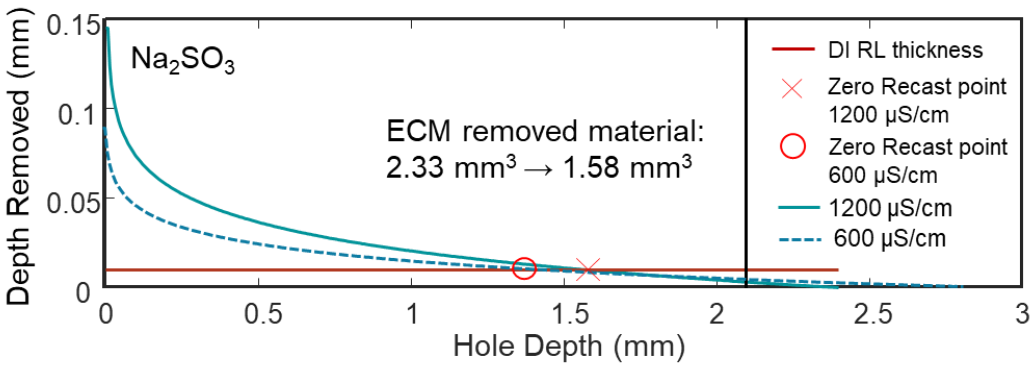

Figure 74. Modelled recast layer profile. Shows resulting model hole profile for the sodium sulfite based on pulse data captured at the calculated current efficiency. A zero-recast point is shown for each profile at two conductivity levels and the total removed volume is shown.

The actual zero recast point was measured as a range, from the optical and SEM surface images, and confirmed with recast layer cross sections. An example of the difference in zero recast layer zones is shown in Figure 75, and the values shown in Table 6. The discrepancy between the actual and modelled values can be attributed to the influence of resistance in the gap. Although the total volume is likely to be similar, the spread of the removed recast layer will be different, essentially spreading material removal across the surface and not compounding near the entrance. This pushes the zero recast point further down the hole and is likely to match the real surfaces better. Adding resistance to the model is difficult due to the gap being full of debris and gases, therefore it is hard to model, however this should be considered for further development of this process model in future.

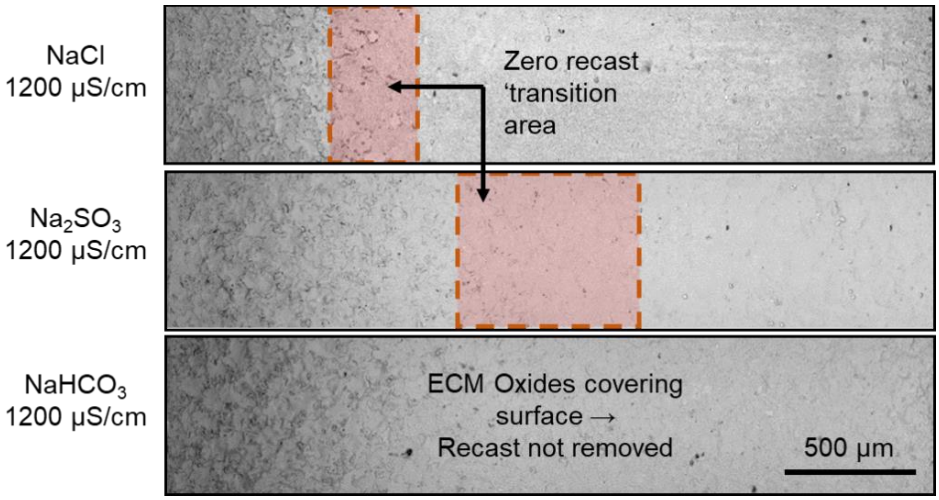

Figure 75. Example differences in zero recast zones for three dielectrics. The zero-recast transition area is highlighted in red, and is the area where zero recast occurs. NaHCO[3] shows no zero recast area due to surface oxides.

In Figure 75 $NaHCO_3$ exhibits a surface which never reaches zero recast due to oxide formation due to ECM. The material removed in the model does not include oxide generation, as in reality the material is mostly oxidised and remains on the surface with some spalling... The difference in current efficiency for different electrolytic-dielectrics can be used as a way to encapsulate the various influences on the ECM side of the process as an easily applied corrective factor. Although gap conditions won't be the same due to hole advance and EDM gases and debris, it is a good method to characterise different electrolytic-dielectrics for use in selection and should be considered for future work.

Table 6 - Zero recast point ranges for machined holes compared to the model. Ranges calculated from 3 holes.

	Zero recast point (mm)	
Dielectric	**Model**	**Experiment**
Na_2SO_3 600 µS/cm	1.38	0.65 – 0.93
Na_2SO_3 1200 µS/cm	1.58	0.82 – 1.40

6.5 Conclusion

Discrete pulse types were described through pulse waveform analysis of the process. The process was split into four pulse types: electrical, semi-arc, delayed, and electrochemical. It was shown that regions of high-voltage, when using DI, would result in regions of electrochemical machining when conductivity was increased. These pulse types were considered a major aspect of the process.

It was shown that the balance between electrical and electrochemical discharges was crucial to process understanding and was directly affected by the high voltage intervals which occur when electrode advance has halted or is retracting due to gap conditions, thus pulse energy causes dissolution. The high voltage intervals and pulse ratio are both good measures of the balance between the EDM and ECM side, with high voltage intervals being easier to measure and control. The electrochemical difference between electrolytic-dielectrics was shown through the EDM:ECM pulse ratio, showing that NaCl, which is the most aggressive non-passivating salt, has the most ECM pulses, while $NaHCO_3$ which is the least aggressive has the most EDM pulses. Differences in electrolytic-dielectrics were explained due to dissolution mechanisms and pulse charge, which increase the high voltage intervals and ECM pulses. Similarly, an increase in conductivity and depth increases ECM pulses and charge, similarly hindering EDM pulses, while also increasing the high voltage intervals due to increased anions carrying charge. With time and depth the pulse ratio decreases while the high voltage intervals increase, due to the mechanisms discussed above.

This was linked to gas-time analysis which showed that an increase in current hole depth is reflected as an increase in gas produced, which was linked to the increased EDM pulses, MRR, and decreased instability regions (high voltage intervals) which also increase with depth. It can be inferred that increased bubbles and debris result in EDM sparking, which reduces the high voltage instability intervals, while increased electrochemical machining causes high voltage instability intervals. Na_2SO_3 showed decreased gas production relative to the MRR and pulse ratios, which was explained by the different electrochemical behaviour (oxygen scavenger), while NaCl showed a high MRR and increased gas production even though it had a lower EDM pulse ratio, which was explained by increased bubbles, increased heat released, which promote electrical discharges, and increased molten material removal.

A mathematical model was used to illustrate the overall process balance through fundamental electrochemical theory and process pulse data. Through this model, the point during machining at which complete recast layer removal occurs is predicted and validated through experimental analysis. It showed that NaCl will have the largest recast free area (lower zero recast point) while $NaHCO_3$ will have the smallest recast free area, explained due to the process pulse data.

By altering the electrolytic-dielectric through the choice of salt additives and therefore conductivity, the resulting hole profile, accuracy, and zero recast point can be controlled, as well as the resulting surface integrity. Similarly, by altering the pulse charge and frequency for ECM and EDM pulses throughout machining of the hole the recast layer can also be fine-tuned. This ‘pivot-point’ mechanism between EDM and ECM and the resulting zero-recast point is

crucial to producing a tailored surface and should be explored further through altering of EDM parameters. Process optimisation can then be used to achieve desired hole surface morphology and accuracy, through the understanding gained through this work. This process adaptation and its fundamental understanding have significant implications for implementing electrolytic-dielectrics in current EDM setups in high value applications, where varying hole depths as well as predictable and good mechanical properties are required.

7 Conclusions and Outlook

7.1 General Conclusions

EDM hole drilling is a high-value manufacturing process crucial in many industries, especially in aerospace, and enables repeatable, high-quality, and cost-effective manufacture of cooling holes for turbine blades. The recast layer is something that the industry has had to accept as a side effect of the process, resulting in large and costly initiatives to minimise the effect of the recast layer on part integrity, and even then, a recast layer remains limiting potential part integrity. This work has first proposed a route to minimise the influence of the recast layer, in terms of oxides, by parametric and fundamental analysis. Oxides have not been extensively explored; therefore this works helps to enable the control of oxides in the recast layer. Secondly this work has proposed a route to a zero-recast single-step process to enable the manufacturing of defect free EDM surfaces by formation of a hybrid EDM-ECM method utilising electrolytic-dielectrics. The proposed hybrid EDM ECM method utilising electrolytic-dielectrics can be a valuable process in high value

manufacturing due to its low cost and ease of machine adaption and implementation, combining the accuracy of EDM with the surface integrity of ECM. The work has wider implications in that it can be used for any EDM process, therefore enabling die-sinking of moulds or W-EDM cutting to produce parts with surfaces free of defects.

The process understanding and theory proposed in this study open up a route to zero recast machining through control of process fundamentals and key process parameters, which has not been explored previously. The notion of control of resulting surfaces through tailored electrolytic-dielectrics was shown and is key to future control of the surface, as well as the idea that the balance of EDM and ECM, which is elucidated through the EDM:ECM pulse ratio, is critical to producing a tailored and desired surface. Further control of the process is envisioned through control of EDM parameters to fine tune pulse energies and characteristics, as well direct control of the pulse ratio

In **Chapter 4**, a route to reduced oxides in the recast layer was conducted. Through parametric analysis, current, on-time and discharge power were shown to increase oxides, while off-time and pressure decrease oxides. A change in current increases oxides due to increased gas production, molten metal, metal vapour, and gap temperature, similarly with on-time in addition to molten metal exposure time. However longer on-times produced more oxides at similar power levels, due to increase exposure time and decrease in discharge impulse force of longer on-times, which reduces material ejection, increases exposure to oxygen, and increases gap temperatures. Higher currents however increase metal ejection and removal of oxides, resulting in

marginal increases in oxides at similar power levels. An increase in off-time and flushing pressure results in decreased oxides due to decrease gases, and was linked to decreased gap temperatures, improved cooling, and reduced debris.

In summary, discharge impulse forces must be high to ensure molten metal ejection, prevent increased concentration around edges, and longer exposure times to gases and energy. To achieve a hole with a low amount of oxides, a small on-time and lower discharge energy is needed, as well as increased flushing and off-time. This results in a parameter with high discharge impulse and high gap flushing and cooling. This would result in a hole with decreased oxides as well as surface roughness, decreased recast layer depth and an expected increase in surface integrity while also decreasing the electrode wear. However, the machine time would also increase which may be unwanted. A balance is therefore required depending on the usage case using the fundamental understanding of oxide formation as a basis.

In **Chapter 5**, a route to a zero-recast EDM surface was conducted. Through combination of EDM and ECM in a simultaneous process a surface which exhibits zero recast can be produced and controlled through altering dissolution mechanisms. In the process electrochemical machining is acting throughout the hole surface, however EDM discharges only occur on the frontal area due to side gap widening. This side gap increase is enhanced by an increase in electrochemical removal and depth. The side areas thus act as an electrolyte, while the frontal area acts a dielectric.

Increasing conductivity was shown to increase removal of the recast layer with NaCl, as well as exposure time shown through an increase with depth. NaCl produced a pitted surface, therefore the aim was to control electrochemical dissolution mechanisms to control the resulting surface. $NaHCO_3$ was shown to result in a surface with passive oxides with limited recast layer removal. $NaNO_3$ and $NaNO_2$ produced surfaces with removed recast layers, however with regions of excessive electrochemical pitting and removal. Finally, Na_2SO_4 and Na_2SO_3 produced smooth surfaces with removed recast, with Na_2SO_3 removing the recast through controlled electro-polishing. The change of surface morphology with depth was also least with Na_2SO_3 and largest with $NaNO_3$, showing the difference in surface controllability between electrolytic-dielectrics. Control of the recast layer was thus shown, and a desired zero-recast surface was produced.

In **Chapter 6**, the process mechanisms were further explored by waveform and gas analysis. The process was split into four pulse types: electrical, semi-arc, delayed, and electrochemical. It was shown that regions of high-voltage, when using DI, would result in regions of ECM machining when conductivity was increased. The balance between electrical and ECM discharges was crucial to process understanding and was directly affected by the high voltage intervals which occur when electrode advance has halted or is retracting due to gap conditions. The electrochemical difference between electrolytic-dielectrics was shown through the EDM:ECM pulse ratio, showing that NaCl, which is the most aggressive non-passivating salt, has the most ECM pulses, while $NaHCO_3$ which is the least aggressive has the most EDM pulses.

Differences in electrolytic-dielectrics were explained due to dissolution mechanisms and pulse charge, which increase the high voltage intervals and ECM pulses. Similarly, an increase in conductivity and depth increases ECM pulses and charge, similarly hindering EDM pulses. This was linked to gas-time analysis showing that an increase in current hole depth is reflected as an increase in gas, linked to the increased EDM pulses, MRR, and high voltage intervals, which also increase with depth. Increased bubbles and debris result in EDM sparking, which reduces the high voltage instability intervals, while increased ECM causes high voltage instability intervals. Na_2SO_3 showed decreased gas production relative to the MRR and pulse ratios, which was explained by the different electrochemical behaviour (oxygen scavenger), while NaCl showed a high MRR and increased gas production even though it had a lower EDM pulse ratio, which was explained by electrochemical gas production.

A mathematical model was used to illustrate the overall process balance through fundamental electrochemical theory and process pulse data. Through this model, the point during machining at which complete recast layer removal occurs is predicted and validated through experimental analysis. It showed that NaCl will have the largest recast free area (lower zero recast point) while $NaHCO_3$ will have the smallest recast free area, explained due to the process pulse data.

By altering the electrolytic-dielectric through the choice of salt additives and therefore conductivity, the resulting hole profile, zero recast point, and expected surface integrity can be controlled. Similarly, by altering the pulse charge and frequency for ECM and EDM pulses throughout machining of the

hole the recast layer can also be fine-tuned. This ‘pivot-point’ mechanism between EDM and ECM and the resulting zero-recast point is crucial to producing a tailored surface.

7.2 Outlook

From the current work there are still some gaps which require further work to understand this unique process:

Although the surface integrity is expected to increase due to reduction of recast layer features such as cracks and brittle surfaces, the difference in surface integrity was not compared experimentally. The effect on different types of fatigue failure (thermal and mechanical) is a good way to numerically compare surfaces. Other tests such as micro pillar compression are also a good way to compare the EDM recast layer surface and the surface produced by electrolytic-dielectrics.

EDM parameters were not changed for the electrolytic-dielectrics in this work, however it is expected that parameters will have a large impact on the process. From research in the oxidation chapter, we can apply the logic used to control oxides to control the amount of electrochemical machining. Parameters which cause high oxides are parameters which cause increased electrochemical machining, and conversely low oxide parameters will cause decreased electrochemical machining. A higher on-time is likely to increase electrochemical machining, while a short on-time may hinder it. Using this, and the effect of the other parameters, it may be possible to further control the process to produce desired surfaces dynamically throughout machining in conjunction with high voltage intervals and gas data.

Electrolytic-dielectrics produced surfaces are heavily dependant on the ratio of EDM and ECM pulses. Although in this work the removal mechanisms were only altered chemically by conductivity and salt additives, another way to shift the pivot point of the process is addition of additives to promote EDM sparking. Micro or nano-conductive particles can be added to the electrolytic-dielectrics to force hole advance via EDM discharges even when electrochemical aspects try to hinder discharges. This can possibly enable higher chemical dissolution rates without affected EDM and can increase EDM MRR and even improve the resultant surface.

The process is expected to behave significantly differently when the workpiece is altered. The route laid out in this work can still be used with any workpiece and electrode, however dissolution mechanisms will differ and must be explored further. The effect of electrode size was shown to have a small effect for oxides, however for electrolytic-dielectrics where the pulse ratio is important a significant difference may be observed. Small holes are machined significantly faster; therefore a high EDM pulse ratio may result in minimal electrochemical dissolution due to time for electrochemical removal. In this case the pulse ratio must be shifted towards electrochemical pulses to ensure sufficient recast layer removal. Therefore, the effect of the electrode and workpiece must be explored further.

Gas analysis can be used to link directly to chemical mechanisms by analysis of the gas proportions and constituents. By understanding the effect of parameters and dielectrics on the resultant gas, chemical dissolution mechanisms can be further quantified. For the oxides, the proportion of O can be directly measured and compared for different EDM parameters, while for

electrolytic-dielectrics the proportions and constituents can be linked to altered chemical dissolution mechanisms. The effect of EDM parameters on gases can also reveal the influence of current, on-time, and off-time on the chemical mechanisms in a fundamental way. To view the change in gas more directly, an improved gas collection method must be used. The entry path to the eudiometer tube should reduce any gas coalescence and lag, due to path geometry. This can be used to allow a more time correct and high-resolution viewing of the change in gas rate and EDM ratio.

To enable better understanding of the process, improvements can be made to the process model. Current efficiency for each electrolytic-dielectric can enable better comparison, while the addition of gap resistance can result in a more realistic recast remove distribution. Waveform capture can also be improved with equipment that can enable a larger capture region or preferably capture pulses for the entire machining duration. This can enable better understanding of changes with depth and can improve process modelling by varying pulses and charge values with time.

The process can also be adapted for through holes, as well as EDM die-sinking and W-EDM to produce recast free surfaces. Through holes can produce recast free surfaces throughout the entire hole surface because once the electrode passes through the hole, electrical discharge cease resulting in just electrochemical removal. For die-sinking high-pressure dielectric is essential, therefore research must be focused on methods for introducing electrolytic-dielectric to the machining surface. This has the potential to create large areas of recast free surfaces, which is highly desired in many industries. For W-EDM, high pressure flushing is used therefore application is easier.

References

1. Christman, D.H.H.L., *Method of making dies*. 1966, Motors Liquidation Co: US.
2. Marriage, P.V., *Cooled turbomachinery components*, E.P. Office, Editor. 1988, Rolls-ROyce plc.
3. IHI, *Slicing Tomatoes Extremely Thinly by Using an Aircraft Engine Technology*. 2011, IHI Coporation: Tokyo.
4. Kunieda, M., *Challenges to Miniturization in micro-EDM.* Proceeding of the Twenty-third Annual Meeting of the American Society for Precision Engineering and the twelfth ICPE Portland, 2008.
5. Makino *EDM Technology Brings High-Quality Surface Finish to Mold-Making Operation*.
6. Makenzi, M. and B.W. Ikua. *A review of flushing techniques used in electrical discharge machining*. 2012.
7. Zhang, S., et al., *Study on the Gap Flow Simulation in EDM Small Hole Machining with Ti Alloy.* Advances in Materials Science and Engineering, 2017. **2017**: p. 8408793.
8. Yahagi, Y., et al., *Micro Drilling EDM with High Rotation Speed of Tool Electrode Using the Electrostatic Induction Feeding Method.* Procedia CIRP, 2012. **1**: p. 162-165.
9. Meek J.M, C.J.D., *Electrical Breakdown of Gases*. The International Series of Monographs on Physics. 1953, London: Oxford at the Clarendon Press.
10. Jane Lehr, P.R., *Foundations of Pulsed Power Technology*. 2017: Wiley-IEEE Press.
11. Zhang, X., B. Lin, and Y. Li, *Experimental study on the effects of electrode materials on coal breaking by plasma.* Fuel, 2020. **270**: p. 117085.
12. Wang, J., et al., *Insight on Relation between Discharge Delay Time and Machining Parameters in Wire EDM.* Procedia CIRP, 2022. **113**: p. 289-293.
13. Kolb, J.F., et al., *Streamers in water and other dielectric liquids.* Journal of Physics D: Applied Physics, 2008. **41**(23): p. 234007.
14. Nijdam, S., J. Teunissen, and U. Ebert, *The physics of streamer discharge phenomena.* Plasma Sources Science and Technology, 2020. **29**(10): p. 103001.
15. Fujita, H., et al., *Initiation process and propagation mechanism of positive streamer discharge in water.* Journal of Applied Physics, 2014. **116**(21): p. 213301.
16. Sun, A., C. Huo, and J. Zhuang, *Formation mechanism of streamer discharges in liquids: a review.* High Voltage, 2016. **1**(2): p. 74-80.
17. Raizer, Y.P., *Gas Discharge Physics*, ed. J.E. Allen. 1991, Berlin Springer-Verlag Berlin Heidelberg. 449.
18. Wiessner, M., et al., *Fundamental Investigation of EDM Plasmas, Part I: A Comparison between Electric Discharges in Gaseous and Liquid Dielectric Media.* Procedia CIRP, 2018. **68**: p. 330-335.
19. Liu, Q., et al., *Study on the Time-Varying Characteristics of Discharge Plasma in Micro-Electrical Discharge Machining.* Coatings, 2019. **9**(11): p. 718.
20. Kitamura, T. and M. Kunieda, *Clarification of EDM gap phenomena using transparent electrodes.* CIRP Annals, 2014. **63**(1): p. 213-216.
21. Shervani-Tabar, M.T., M.H. Seyed-Sadjadi, and M.R. Shabgard, *Numerical study on the splitting of a vapor bubble in the ultrasonic assisted EDM process with the curved tool and workpiece.* Ultrasonics, 2013. **53**(1): p. 203-210.
22. Lauwers, B., et al., *Investigation of material removal mechanisms in EDM of composite ceramic materials.* Journal of Materials Processing Technology, 2004. **149**(1): p. 347-352.

23. Zhang, S., et al., *Study of the thermal erosion, ejection and solidification processes of electrode materials during EDM.* Engineering Applications of Computational Fluid Mechanics, 2019. **13**(1): p. 1153-1164.
24. Tang, J. and X. Yang, *A novel thermo-hydraulic coupling model to investigate the crater formation in electrical discharge machining.* Journal of Physics D: Applied Physics, 2017. **50**(36): p. 365301.
25. Yue, X. and X. Yang, *Study on the Distribution of Removal Material of EDM in Deionized Water and Gas with Molecular Dynamics Simulation.* Procedia CIRP, 2016. **42**: p. 691-696.
26. Yue, X. and X. Yang, *Molecular dynamics simulation of the material removal process and gap phenomenon of nano EDM in deionized water.* RSC Advances, 2015. **5**(82): p. 66502-66510.
27. Zhang, Y., et al., *Transient dynamics simulation of the electrical discharge-generated bubble in sinking EDM.* The International Journal of Advanced Manufacturing Technology, 2013. **68**(5): p. 1707-1715.
28. Singh, M., S. Sharma, and J. Ramkumar, *Numerical Simulation of Melt-Pool Hydrodynamics in μ-EDM Process.* Procedia CIRP, 2020. **95**: p. 226-231.
29. Yue, X. and X. Yang, *Molecular dynamics simulation of material removal process and mechanism of EDM using a two-temperature model.* Applied Surface Science, 2020. **528**: p. 147009.
30. 岳, 暁., 暁. 楊, and 正. 国枝, *Measurement of discharge reaction force caused by metal vapor jets in EDM.* 精密工学会学術講演会講演論文集, 2017. **2017A**: p. 93-94.
31. Yue, X. and X. Yang, *The role of discharge plasma on molten pool dynamics in EDM.* Journal of Materials Processing Technology, 2021. **293**: p. 117092.
32. Yang, X., X. Han, and M. Kunieda, *Molecular Dynamics Simulation of Pressure Generated inside Melting Area in EDM.* Key Engineering Materials, 2014. **625**: p. 525-529.
33. Yue, X. and X. Yang, *Molecular dynamics simulation of material removal process and crystal structure evolution in EDM with discharge on different crystal planes.* The International Journal of Advanced Manufacturing Technology, 2017. **92**(9): p. 3155-3165.
34. Yue, X., X. Yang, and M. Kunieda, *Influence of metal vapor jets from tool electrode on material removal of workpiece in EDM.* Precision Engineering, 2018. **53**: p. 278-288.
35. Yue, X., et al., *Novel methods for high-speed observation of material removal and molten pool movement in EDM.* Precision Engineering, 2020. **66**: p. 295-305.
36. Yue, X., et al., *Influence of discharge gap on material removal and melt pool movement in EDM discharge process.* The International Journal of Advanced Manufacturing Technology, 2022. **119**(11): p. 7827-7842.
37. Kunieda, M., M. Tohi, and Y. Ohsako, *Reaction forces observed in pulse discharges of EDM.* IJEM, 2003. **8**: p. 51-56.
38. Gu, W., M. Kunieda, and W. Zhao, *Behaviors of Bubbles generated in Wire Electrical Discharge Machining.* Proceedings of JSPE Semestrial Meeting, 2021. **2021A**: p. 494-495.
39. Shervani-Tabar, M.T. and N. Mobadersany, *Numerical study on the hydrodynamic behavior of the dielectric fluid around an electrical discharge generated bubble in EDM.* Theoretical and Computational Fluid Dynamics, 2013. **27**(5): p. 701-719.
40. Chakraborty, S., V. Dey, and S.K. Ghosh, *A review on the use of dielectric fluids and their effects in electrical discharge machining characteristics.* Precision Engineering, 2015. **40**: p. 1-6.
41. Fontanals, N., F. Borrull, and R.M. Marcé, *Overview of mixed-mode ion-exchange materials in the extraction of organic compounds.* Analytica Chimica Acta, 2020.

42. Zhang, Y., et al., *Investigation on the influence of the dielectrics on the material removal characteristics of EDM.* Journal of Materials Processing Technology, 2014. **214**(5): p. 1052-1061.
43. Zhang, Y., et al., *Study of the recast layer of a surface machined by sinking electrical discharge machining using water-in-oil emulsion as dielectric.* Applied Surface Science, 2011. **257**(14): p. 5989-5997.
44. Chen, S.L., B.H. Yan, and F.Y. Huang, *Influence of kerosene and distilled water as dielectrics on the electric discharge machining characteristics of Ti–6A1–4V.* Journal of Materials Processing Technology, 1999. **87**(1): p. 107-111.
45. Zhang, M., et al., *Effects of Some Process Parameters on the Impulse Force in Single Pulsed EDM.* Procedia CIRP, 2016. **42**: p. 627-631.
46. Liao, Y.S., J.T. Huang, and Y.H. Chen, *A study to achieve a fine surface finish in Wire-EDM.* Journal of Materials Processing Technology, 2004. **149**(1): p. 165-171.
47. Li, C., et al., *Effects of dielectric fluids on surface integrity for the recast layer in high speed EDM drilling of nickel alloy.* Journal of Alloys and Compounds, 2019. **783**: p. 95-102.
48. Storr, M., et al., *A new additive and application system for wire-EDM*. 2010.
49. Ekmekci, B., et al., *Suspended SiC particle deposition on plastic mold steel surfaces in powder-mixed electrical discharge machining.* Proceedings of the Institution of Mechanical Engineers, Part B: Journal of Engineering Manufacture, 2014. **229**(3): p. 475-486.
50. Kibria, G., et al., *Comparative study of different dielectrics for micro-EDM performance during microhole machining of Ti-6Al-4V alloy.* The International Journal of Advanced Manufacturing Technology, 2010. **48**(5): p. 557-570.
51. Kolli, M. and A. Kumar, *Effect of dielectric fluid with surfactant and graphite powder on Electrical Discharge Machining of titanium alloy using Taguchi method.* Engineering Science and Technology, an International Journal, 2015. **18**(4): p. 524-535.
52. Wu, K.L., et al., *Study on the characteristics of electrical discharge machining using dielectric with surfactant.* Journal of Materials Processing Technology, 2009. **209**(8): p. 3783-3789.
53. Du, Y., et al., *Effect of semiconductive nanoparticles on insulating performances of transformer oil.* IEEE Transactions on Dielectrics and Electrical Insulation, 2012. **19**(3): p. 770-776.
54. Li, Y.Z., et al., *Effects of additives on dielectric strength of naphthenic transformer oil.* Journal of Molecular Liquids, 2018. **271**: p. 1-7.
55. R, M. and S. Balaraman, *Investigation on effects of different types of nanoparticles on critical parameters of nano-liquid insulation systems.* Journal of Molecular Liquids, 2017. **230**: p. 437-444.
56. Leão, F.N. and I.R. Pashby, *A review on the use of environmentally-friendly dielectric fluids in electrical discharge machining.* Journal of Materials Processing Technology, 2004. **149**(1): p. 341-346.
57. Rozenek, M., *Sinking electrical discharge machining with glycol and glycerol application as dielectric fluid*. Vol. 2017. 2018. 020027.
58. Takamura, N., et al. *Effects of Types and Amounts of Additive Polymers on Resistivity and Dielectric Strength of Pure Water*. in *Annual Report - Conference on Electrical Insulation and Dielectric Phenomena, CEIDP*. 2019.
59. Rehbein, W., H.P. Schulze, and M. Storr, *Influence of liquid additives in electro-erosive micromachining (EDMM).* International Journal of Material Forming, 2009. **2**: p. 661-664.
60. Ushakov, V.Y., *Impulse Breakdown of Liquids*. Power Systems 2007: Springer.

61. Li, G., W. Natsu, and Z. Yu, *Study on quantitative estimation of bubble behavior in micro hole drilling with EDM.* International Journal of Machine Tools and Manufacture, 2019. **146**: p. 103437.
62. Li, G., W. Natsu, and Z. Yu, *Elucidation of the mechanism of the deteriorating interelectrode environment in micro EDM drilling.* International Journal of Machine Tools and Manufacture, 2021. **167**: p. 103747.
63. Kitamura, T., M. Kunieda, and K. Abe, *Observation of relationship between bubbles and discharge locations in EDM using transparent electrodes.* Precision Engineering, 2015. **40**: p. 26-32.
64. Murray, J., D. Zdebski, and A.T. Clare, *Workpiece debris deposition on tool electrodes and secondary discharge phenomena in micro-EDM.* Journal of Materials Processing Technology, 2012. **212**(7): p. 1537-1547.
65. Wang, Z., et al., *Dielectric flushing optimization of fast hole EDM drilling based on debris status analysis.* The International Journal of Advanced Manufacturing Technology, 2018. **97**(5): p. 2409-2417.
66. Liao, Z., et al., *Surface integrity in metal machining - Part I: Fundamentals of surface characteristics and formation mechanisms.* International Journal of Machine Tools and Manufacture, 2021. **162**: p. 103687.
67. la Monaca, A., et al., *Surface integrity in metal machining - Part II: Functional performance.* International Journal of Machine Tools and Manufacture, 2021. **164**: p. 103718.
68. Gostimirović, M., et al., *Influence of discharge energy on machining characteristics in EDM.* Journal of Mechanical Science and Technology, 2012. **26**.
69. Lee, H.-T., F.-C. Hsu, and T.-Y. Tai, *Study of surface integrity using the small area EDM process with a copper–tungsten electrode.* Materials Science and Engineering: A, 2004. **364**(1): p. 346-356.
70. Lee, H.T. and T.Y. Tai, *Relationship between EDM parameters and surface crack formation.* Journal of Materials Processing Technology, 2003. **142**(3): p. 676-683.
71. Rebelo, J.C., et al., *Influence of EDM pulse energy on the surface integrity of martensitic steels.* Journal of Materials Processing Technology, 1998. **84**(1): p. 90-96.
72. Das, A.K., et al., *Influence of process parameters on the surface integrity of micro-holes of SS304 obtained by micro-EDM.* Journal of the Brazilian Society of Mechanical Sciences and Engineering, 2016. **38**(7): p. 2029-2037.
73. Chen, Z., et al., *Surface Integrity and Fatigue Performance of Inconel 718 in Wire Electrical Discharge Machining.* Procedia CIRP, 2016. **45**: p. 307-310.
74. Ghanem, F., C. Braham, and H. Sidhom, *Influence of steel type on electrical discharge machined surface integrity.* Journal of Materials Processing Technology, 2003. **142**(1): p. 163-173.
75. Bhattacharyya, B., S. Gangopadhyay, and B.R. Sarkar, *Modelling and analysis of EDMED job surface integrity.* Journal of Materials Processing Technology, 2007. **189**(1): p. 169-177.
76. Kutz, M., *Handbook of Environmental Degradation of Materials (2nd Edition)*. Elsevier.
77. Zhang, J.-S., *25 - Environmental Damage at High Temperature*, in *High Temperature Deformation and Fracture of Materials*, J.-S. Zhang, Editor. 2010, Woodhead Publishing. p. 330-348.
78. Themelis, N.J., *Transport and Chemical Rate Phenomena*. 1995, Basel: Gordon and Breach.
79. R. Vasant Kumar, J.C., David Brook. *Ellingham Diagrams*. DoITPoMS 2022 [cited 2022.

80. Ihara, S., *Feasibility of hydrogen production by direct water splitting at high temperature.* International Journal of Hydrogen Energy, 1978. **3**(3): p. 287-296.
81. Pyle, W.R., M.H. Hayes, and A.L. Spivak. *Direct solar-thermal hydrogen production from water using nozzle/skimmer and glow discharge*. in *IECEC 96. Proceedings of the 31st Intersociety Energy Conversion Engineering Conference*. 1996.
82. Kojima, A., W. Natsu, and M. Kunieda, *Spectroscopic measurement of arc plasma diameter in EDM.* CIRP Annals, 2008. **57**(1): p. 203-207.
83. Descoeudres, A., *Characterization of electrical discharge machining plasmas*. 2006, Lausanne, EPFL. p. 137.
84. Yadav, V.K., P. Kumar, and A. Dvivedi, *Performance enhancement of rotary tool near-dry EDM of HSS by supplying oxygen gas in the dielectric medium.* Materials and Manufacturing Processes, 2019. **34**(16): p. 1832-1846.
85. Kanemaru, M., et al., *Single bubble generated by a pulsed discharge in liquids as a plasma microreactor.* Plasma Sources Science and Technology, 2011. **20**(3): p. 034007.
86. Munz, M., M. Risto, and R. Haas, *The Phenomenon of Polarity in EDM Drilling Process Using Water Based Dielectrics.* Procedia CIRP, 2016. **42**: p. 532-536.
87. Kunieda, M., M. Yoshida, and N. Taniguchi, *Electrical Discharge Machining in Gas.* CIRP Annals, 1997. **46**(1): p. 143-146.
88. Kliuev, M., *EDM Drilling and Milling of Aerospace Materials*. 2019, ETH Zurich: Zurich.
89. Morar, N.I., et al., *Investigation of recast and crack formation in laser trepanning drilling of CMSX-4 angled holes.* The International Journal of Advanced Manufacturing Technology, 2018. **95**(9): p. 4059-4070.
90. Sezer, H.K., et al., *Effect of beam angle on HAZ, recast and oxide layer characteristics in laser drilling of TBC nickel superalloys.* International Journal of Machine Tools and Manufacture, 2006. **46**(15): p. 1972-1982.
91. Leigh, S., et al., *Recast and oxide formation in laser-drilled acute holes in CMSX-4 nickel single-crystal superalloy.* Proceedings of the Institution of Mechanical Engineers, Part B: Journal of Engineering Manufacture, 2010. **224**(7): p. 1005-1016.
92. De Luca, A., et al., *Microstructure and defects in a Ni-Cr-Al-Ti γ/γ′ model superalloy processed by laser powder bed fusion.* Materials & Design, 2021. **201**: p. 109531.
93. Lee, L.C., L.C. Lim, and Y.S. Wong, *Towards crack minimisation of EDMed surfaces.* Journal of Materials Processing Technology, 1992. **32**(1): p. 45-54.
94. Li, L., et al., *Surface Integrity Characteristics in Wire-EDM of Inconel 718 at Different Discharge Energy.* Procedia CIRP, 2013. **6**: p. 220-225.
95. Gudipudi, S., et al., *Fabrication and experimental study to optimize the recast layer and the material removal in electric discharge machining (EDM) of AA6061-B4C composite.* Materials Today: Proceedings, 2019. **19**: p. 448-454.
96. Goyal, A., A. Garimella, and P. Saini, *Optimization of surface roughness by design of experiment techniques during wire EDM machining.* Materials Today: Proceedings, 2021. **47**: p. 3195-3197.
97. Holmberg, J., A. Wretland, and J. Berglund, *Grit Blasting for Removal of Recast Layer from EDM Process on Inconel 718 Shaft: An Evaluation of Surface Integrity.* Journal of Materials Engineering and Performance, 2016. **25**(12): p. 5540-5550.
98. Qu, J., et al., *Abrasive micro-blasting to improve surface integrity of electrical discharge machined WC–Co composite.* Journal of Materials Processing Technology, 2005. **166**(3): p. 440-448.

99. Khangura, S.S., et al., *Investigations Into the Removal of EDM Recast Layer With Magnetic Abrasive Machining*, in *ASME 2015 International Manufacturing Science and Engineering Conference*. 2015.
100. Yan, B.-H., et al., *Improving Electrical Discharge Machined Surfaces Using Magnetic Abrasive Finishing.* Machining Science and Technology, 2004. **8**(1): p. 103-118.
101. Holmberg, J., et al., *Surface integrity after post processing of EDM processed Inconel 718 shaft.* The International Journal of Advanced Manufacturing Technology, 2018. **95**(5-8): p. 2325-2337.
102. Joshi, S.S. and D. Marla, *11.15 - Electrochemical Micromachining*, in *Comprehensive Materials Processing*, S. Hashmi, et al., Editors. 2014, Elsevier: Oxford. p. 373-403.
103. Lohrengel, M.M., K.P. Rataj, and T. Münninghoff, *Electrochemical Machining—mechanisms of anodic dissolution.* Electrochimica Acta, 2016. **201**: p. 348-353.
104. Frankel, G.S., *Pitting Corrosion of Metals: A Review of the Critical Factors.* Journal of The Electrochemical Society, 1998. **145**(6): p. 2186-2198.
105. Landolt, D., *Fundamental aspects of electropolishing.* Electrochimica Acta, 1987. **32**(1): p. 1-11.
106. Datta, M. and D. Landolt, *Film Breakdown on Nickel under Transpassive Dissolution Conditions in Sodium Nitrate Solutions.* Journal of The Electrochemical Society, 1977. **124**(4): p. 483-489.
107. Chu, X., et al., *Electrolytic removal of recast layers on micro-EDM microstructure surfaces.* The International Journal of Advanced Manufacturing Technology, 2020. **108**(3): p. 867-879.
108. Wang, C.-C., et al., *Recast layer removal after electrical discharge machining via Taguchi analysis: A feasibility study.* Journal of Materials Processing Technology, 2009. **209**(8): p. 4134-4140.
109. Ramasawmy, H. and L. Blunt, *3D surface topography assessment of the effect of different electrolytes during electrochemical polishing of EDM surfaces.* International Journal of Machine Tools and Manufacture, 2002. **42**(5): p. 567-574.
110. Wu, X., et al., *Using WECM to remove the recast layer and reduce the surface roughness of WEDM surface.* Journal of Materials Processing Technology, 2019. **268**: p. 140-148.
111. Kishi, R. and J. Yan, *Electrical Discharge/Electrochemical Hybrid Machining Based on the Same Machine and Tool Electrode.* Journal of Micro and Nano-Manufacturing, 2020. **8**(1).
112. Liu, J.W., T.M. Yue, and Z.N. Guo, *An analysis of the discharge mechanism in electrochemical discharge machining of particulate reinforced metal matrix composites.* International Journal of Machine Tools and Manufacture, 2010. **50**(1): p. 86-96.
113. Goud, M., A.K. Sharma, and C. Jawalkar, *A review on material removal mechanism in electrochemical discharge machining (ECDM) and possibilities to enhance the material removal rate.* Precision Engineering, 2016. **45**: p. 1-17.
114. Wüthrich, R. and V. Fascio, *Machining of non-conducting materials using electrochemical discharge phenomenon—an overview.* International Journal of Machine Tools and Manufacture, 2005. **45**(9): p. 1095-1108.
115. Rajput, V., M. Goud, and N.M. Suri, *Review—Electrochemical Discharge Machining: Gas Film Electrochemical Aspects, Stability Parameters, and Research Work.* Journal of The Electrochemical Society, 2021. **168**(1): p. 013503.
116. Kumar, N., N. Mandal, and A.K. Das, *Micro-machining through electrochemical discharge processes: a review.* Materials and Manufacturing Processes, 2020. **35**(4): p. 363-404.

117. Krötz, H. and K. Wegener, *Sparc assisted electrochemical machining: a novel possibility for microdrilling into electrical conductive materials using the electrochemical discharge phenomenon.* The International Journal of Advanced Manufacturing Technology, 2015. **79**(9): p. 1633-1643.
118. Zhang, C., et al., *Effect of solution conductivity on tool electrode wear in electrochemical discharge drilling of nickel-based alloy.* The International Journal of Advanced Manufacturing Technology, 2019. **103**(1): p. 743-756.
119. Zhang, C., et al., *Surface integrity of holes machined by electrochemical discharge drilling method.* CIRP Journal of Manufacturing Science and Technology, 2020. **31**: p. 643-651.
120. Zhang, Y., et al., *Machining of a film-cooling hole in a single-crystal superalloy by high-speed electrochemical discharge drilling.* Chinese Journal of Aeronautics, 2016. **29**(2): p. 560-570.
121. Tanjilul, M., D.N. Wee Keong, and A. Senthil Kumar, *Super Dielectric Based EDM Process for Drilling of Inconel 718.* Materials and Manufacturing Processes, 2021. **36**(3): p. 341-350.
122. Rashedul, I.M., et al., *Influence of Different Tool Electrode Materials on Electrochemical Discharge Machining Performances.* Micromachines, 2021. **12**(9).
123. Zhang, J., Z. Xu, and C. Zhang, *Variable-parameter high-precision electrochemical discharge drilling method for 440C-Nb without recast layer.* The International Journal of Advanced Manufacturing Technology, 2020. **110**(9): p. 2815-2826.
124. Weiwen, X., W. Junqi, and Z. Wansheng, *Break-out Detection for High-speed Small Hole Drilling EDM Based on Machine Learning.* Procedia CIRP, 2018. **68**: p. 569-574.
125. Yilmaz, O. and M.A. Okka, *Effect of single and multi-channel electrodes application on EDM fast hole drilling performance.* The International Journal of Advanced Manufacturing Technology, 2010. **51**(1): p. 185-194.
126. Schacht, B., et al., *An Erosion Index for Wire Electrode Materials in EDM*. 2004. p. 157-164.
127. Harris, K. and J.B. Wahl, *Improved single crystal superalloys, CMSX-4®(SLS)[La+Y] and CMSX-486®*. 2004. 45-52.
128. Sugahara, T., et al., *Creep Behavior of the Inconel 718 Superalloy.* Defect and Diffusion Forum, 2012. **326-328**: p. 509-514.
129. Greene, G.A. and C.C. Finfrock, *Oxidation of Inconel 718 in Air at High Temperatures.* Oxidation of Metals, 2001. **55**(5): p. 505-521.
130. Allison, T.C., *NIST-JANAF Thermochemical Tables - SRD 13 (Version 1.0.2)*, N.I.o.S.a. Technology, Editor. 2013, National Institute of Standards and Technology: National Institute of Standards and Technology.
131. Thomas J. Wolery, C.F.J.-C., *Chemical Thermodynamic Data. 1. The Concept of Links to the Chemical Elements and the Historical Development of Key Thermodynamic Data*, S.N. Laboratories, Editor. 2016: Geochimica et Cosmochimica Acta.
132. Pei, H., et al., *Oxidation behavior of recast layer of air-film hole machined by EDM technology of Ni-based single crystal blade and its effect on creep strength.* Surface and Coatings Technology, 2021. **419**: p. 127285.
133. Cao, J., et al., *Microstructure and hot corrosion behavior of the Ni-based superalloy GH202 treated by laser shock processing.* Materials Characterization, 2017. **125**: p. 67-75.
134. Yang, X., et al., *Discharge crater formation simulation coupled by thermo-fluid analysis of arc plasma in EDM.* Procedia CIRP, 2020. **95**: p. 232-237.
135. Wei, D., et al., *Analyzing of Discharge Wave Oscillation Mechanism in Electrical Discharge Machining.* Procedia CIRP, 2016. **42**: p. 23-27.
136. Li, Q. and X. Yang, *Study on arc plasma movement and its effect on crater morphology during single-pulse discharge in EDM.* The International

Journal of Advanced Manufacturing Technology, 2020. **106**(11): p. 5033-5047.
137. Maradia, U., C. Hollenstein, and K. Wegener, *Temporal characteristics of the pulsed electric discharges in small gaps filled with hydrocarbon oil.* Journal of Physics D: Applied Physics, 2015. **48**(5): p. 055202.
138. Zhang, Y., et al., *A novel method of determining energy distribution and plasma diameter of EDM.* International Journal of Heat and Mass Transfer, 2014. **75**: p. 425-432.
139. Yahyavi Zanjani, M., et al., *Process Control in Jet Electrochemical Machining of Stainless Steel through Inline Metrology of Current Density.* Micromachines, 2019. **10**(4): p. 261.
140. Speidel, A., et al., *Post processing of additively manufactured parts using electrochemical jet machining.* Materials Letters, 2021. **292**: p. 129671.
141. Mitchell-Smith, J., et al., *Electrolyte Multiplexing in Electrochemical Jet Processing.* Procedia CIRP, 2018. **68**: p. 483-487.
142. Branzoi, F., et al., *The influence of different aggressive anions on the electrochemical behaviour of aluminium in sodium nitrate aqueous solutions.* Materials and Corrosion, 2000. **51**(9): p. 635-641.
143. Rizvi, M., et al., *Sodium nitrite as a corrosion inhibitor of copper in simulated cooling water.* Scientific Reports, 2021. **11**(1): p. 8353.
144. Rashid, K.H. and A.A. Khadom, *Sodium sulfite as an oxygen scavenger for the corrosion control of mild steel in petroleum refinery wastewater: optimization, mathematical modeling, surface morphology and reaction kinetics studies.* Reaction Kinetics, Mechanisms and Catalysis, 2020. **129**(2): p. 1027-1046.
145. Gavish, N. and K. Promislow, *Dependence of the dielectric constant of electrolyte solutions on ionic concentration: A microfield approach.* Physical Review E, 2016. **94**(1): p. 012611.
146. Hasted, J.B., D.M. Ritson, and C.H. Collie, *Dielectric Properties of Aqueous Ionic Solutions. Parts I and II.* The Journal of Chemical Physics, 1948. **16**(1): p. 1-21.
147. Han, W. and F. Fang, *Fundamental aspects and recent developments in electropolishing.* International Journal of Machine Tools and Manufacture, 2019. **139**: p. 1-23.
148. Wang, D., et al., *Investigation of the electrochemical dissolution behavior of Inconel 718 and 304 stainless steel at low current density in NaNO3 solution.* Electrochimica Acta, 2015. **156**: p. 301-307.
149. Chun, K.H., S.H. Kim, and E.S. Lee, *Analysis of the relationship between electrolyte characteristics and electrochemical machinability in PECM on invar (Fe-Ni)fine sheet.* The International Journal of Advanced Manufacturing Technology, 2016. **87**(9): p. 3009-3017.
150. Li, Z. and J. Bai, *Impulse discharge method to investigate the influence of gap width on discharge characteristics in micro-EDM.* The International Journal of Advanced Manufacturing Technology, 2017. **90**(5-8): p. 1769-1777.
151. Lee, S.H. and X.P. Li, *Study of the effect of machining parameters on the machining characteristics in electrical discharge machining of tungsten carbide.* Journal of Materials Processing Technology, 2001. **115**(3): p. 344-358.
152. Shiek, J., S.J. H, and M. Murugan, *Powder additives influence on dielectric strength of EDM fluid and material removal.* International Journal of Machining and Machinability of Materials, 2020. **22**: p. 47-61.
153. Takeuchi, H. and M. Kunieda, *Relation between Debris Concentration and Discharge Gap Width in EDM Process.* Journal of The Japan Society of Electrical Machining Engineers, 2007. **41**(98): p. 156-162.

154. Wang, X., et al., *Characteristics of plasma channel in powder-mixed EDM based on monopulse discharge.* The International Journal of Advanced Manufacturing Technology, 2016. **82**(5): p. 1063-1069.
155. Jiang, Y., et al., *Adaptive control for small-hole EDM process with wavelet transform detecting method.* Journal of Mechanical Science and Technology, 2012. **26**(6): p. 1885-1890.
156. Graps, A., *An Introduction to Wavelets.* IEEE Computational Science and Engineering, 1995. **2**(2).
157. Zhang, X., et al., *Intelligent pulse analysis of high-speed electrical discharge machining using different RNNs.* Journal of Intelligent Manufacturing, 2020. **31**(4): p. 937-951.
158. Shimasaki, T. and M. Kunieda, *Study on influences of bubbles on ECM gap phenomena using transparent electrode.* CIRP Annals, 2016. **65**(1): p. 225-228.
159. Kurita, T., et al., *The observation of growth and diffusion of electrolytic product in ECM.* Journal of Manufacturing Processes, 2020. **60**: p. 636-643.
160. Kunieda, M., L. Overmeyer, and A. Klink, *Visualization of electro-physical and chemical machining processes.* CIRP Annals, 2019. **68**(2): p. 751-774.
161. Mayank, G., C. Fuchen, and K. Masanori, *Analysis of Reactions Determining Current Efficiency in Electrochemical Machining.* Procedia CIRP, 2018. **68**: p. 511-516.